NORTHWESTERN UNIVERSITY

Precision Measurements of Antiproton-Proton Elastic Scattering at Small Momentum Transfers

A DISSERTATION

SUBMITTED TO THE GRADUATE SCHOOL
IN PARTIAL FULFILLMENT OF THE REQUIREMENTS

for the degree

DOCTOR OF PHILOSOPHY

Field of Physics

By

Steven Trokenheim

EVANSTON, ILLINOIS

June 1995

To my family

Acknowledgements

Many people contributed to the preparation of this dissertation in a variety of different ways.

I thank Professor Kamal K. Seth for directing this research.

The advice and assistance of Miguel Sarmiento, Todd Pedlar, Camille Ginsburg, Petros Rapidis and Stephen Pordes was also extremely helpful.

Finally, this dissertation would not be possible without the work of all those responsible for the design, construction and operation of Fermilab Experiment 760.

ABSTRACT

Precision Measurements of Antiproton-Proton Forward Elastic Scattering at Small Momentum Transfers

Steven Trokenheim

We have made precision measurements of the antiproton-proton elastic scattering differential cross sections in the momentum transfer range of $0.001 \leq |t|(\mathrm{GeV/c})^2 \leq 0.02$ at incident antiproton momenta from 3.45 to 6.23 GeV/c. The experiment was done in the Fermilab Antiproton Accumulator where an internal hydrogen gas-jet target intercepted the circulating antiproton beam. The measurements were made using an array of solid state detectors to detect recoil protons at scattering angles from 85° to 89°. The measured relative differential cross sections were fit to the standard parametrization, with parameters σ_T, b, and ρ. The values of σ_T and b were found to be consistent with previous measurements. The values of ρ were determined with much higher precision than in the previous measurements in this energy range, and were found to be in disagreement with the existing dispersion relation predictions.

Contents

1 Introduction **1**

2 The Recoil Technique **10**

2.1 Kinematics 10

2.2 Theoretical Formulation of Forward Angle Elastic Scattering 16

3 Experimental Apparatus **22**

3.1 The Antiproton Beam 23

3.2 The Gas Jet Target 28

3.3 The E760 Detector System 29

3.4 The Detector System for Proton Recoils 33

3.4.1 The Design Criteria 33

3.4.2 The Mechanical Assembly 35

3.4.3 The Solid State Detectors 39

3.4.4 Detector Performance 40

3.4.5 The Data Acquisition Electronics 45

4 Calibrations **47**

4.1 Energy Calibration 47

4.2 Detector Solid Angle Calibration 52

5 Monte Carlo Calculations **59**

5.1 Interaction Region Density Distribution 59

5.2 Corrections for Beam Displacements 63

6 Experimental Method and Data Analysis **71**

6.1 Data Acquisition 71

6.2 Background Subtraction 73

6.3 Determination of Recoil Energy Centroid 79

6.4 Determination of Relative $d\sigma/d\Omega$ from the Data 82

6.5 Determination of the Forward Scattering Parameters 84

6.6 Systematic Errors 90

7 Discussion of Results **95**

7.1 Results for the ρ Parameter 95

7.1.1 The Analytic Amplitude Analysis of Block et al. 96

7.1.2 The Dispersion Relations Analysis of Kroll and Schweiger . . . 97

7.2 Results for the b-Parameter 103

7.3 Summary and Conclusions 105

A Differential Cross Sections from the Present Experiment **106**

B World Data for σ_T, b, and ρ **120**

List of Figures

1.1 Results for the ρ parameter from the literature 5

2.1 Schematic of $\bar{p}p$ elastic scattering in the laboratory frame 11

2.2 Coordinate system in the laboratory frame. 13

2.3 Dependence of the recoil proton kinetic energy, momentum transfer and range in silicon on the recoil angle at $p_{\rm lab} = 6.23$ GeV/c. 15

2.4 $\bar{p}p$ forward angle differential cross sections at $\sqrt{s}$ of 4.1 and 541 GeV 18

2.5 Differential cross section predictions for typical values of σ_T, b, and ρ 20

3.1 Fermilab Accelerator Complex 24

3.2 Schematic of the E760 detector system. 30

3.3 Schematic view of the apparatus for detecting proton recoils. 35

3.4 Schematic view of the detector pan 37

3.5 The effect of radiation damage on the alpha spectrum of one of the detectors. 44

3.6 Block diagram for the luminosity monitor electronics 46

4.1 Energy spectrum of the ^{244}Cm alpha source 49

4.2 Deviation of ADC channel from linear fit as a function of pulser setting 51

4.3 Energy spectrum of the Am-241 alpha standard 54
4.4 Ratios of the areas of the carriage detectors to that of the fixed detector 58

5.1 Monte Carlo recoil energy spectrum, using a uniform circular gas jet distribution of radius 3.35 mm 61
5.2 Monte Carlo generated recoil spectra compared with real data at three different recoil angles 62
5.3 Fraction of events (calculated via Monte Carlo) not seen by the fixed detector at $\alpha = 3.547°$ and by a detector on the carriage as the result of horizontal beam displacements. 65
5.4 Ratio of counts in a movable detector at $\alpha = 3.547°$ to the counts in the fixed detector at the same angle as a function of the horizontal beam position. 66
5.5 Distributions of measured horizontal beam displacements by three different methods. 68
5.6 Net correction factors to be applied to the counts in the movable detectors normalized to the fixed detector. 70

6.1 Energy spectra for *pp* collisions under various beam/gas jet conditions for a detector at $\alpha = 0.5°$. 74
6.2 Typical energy spectra for two detectors on the carriage 76
6.3 Recoil spectra for detector # 2 at five angles between 1° and 2° . . . 78
6.4 Background-subtracted spectra for each movable detector 80
6.5 Frequency distribution of the measured recoil angle of the fixed detector 81
6.6 Schematic representation of the geometry of the measurements. . . . 83

6.7 Correlations between the three scattering parameters for data sets at two different energies 88
6.8 World data on $\bar{p}p$ total cross sections in the 2 – 8 GeV/c momentum range 89
6.9 Measured differential cross sections at six antiproton momenta 91
6.10 Results for the ρ- and b-parameters from the present experiment . . . 93

7.1 Fits to the pp and $\bar{p}p$ total cross sections using the analytic amplitudes of Block et al. 98
7.2 Fits to the pp and $\bar{p}p$ ρ-parameters using the analytic amplitudes of Block et al. 99
7.3 Total cross section fits used by Kroll and Schweiger in their dispersion relation analysis. 101
7.4 Dispersion theory prediction of Kroll and Schweiger 102
7.5 World data for the b parameter and fits using the parametrization of Block et al. 104

B.1 World data on $\bar{p}p$ total cross sections in the $2 - 50$ GeV/c momentum range with an empirical fit 126

List of Tables

2.1 Relationships between recoil angle, momentum transfer, kinetic energy and proton range in silicon. 14

3.1 History of the performance of the solid state detectors. 41

3.2 Detector characteristics and performance. 45

4.1 Solid angle measurements and area calculations 56

6.1 Uncertainties due to background subtraction 79

6.2 Results for $\bar{p}p$ elastic scattering parameters from the "σ_T free" fit . . 86

6.3 Results for $\bar{p}p$ elastic scattering parameters from the "σ_T fixed" fit . . 90

6.4 Systematic errors contribution to σ_T, b and ρ 94

A.1 Differential cross section results for $p_{\text{lab}} = 3.702$ GeV/c. 107

A.2 Differential cross section results for $p_{\text{lab}} = 4.066$ GeV/c. 109

A.3 Differential cross section results for $p_{\text{lab}} = 5.603$ GeV/c. 110

A.4 Differential cross section results for $p_{\text{lab}} = 5.724$ GeV/c. 114

A.5 Differential cross section results for $p_{\text{lab}} = 5.941$ GeV/c. 116

A.6 Differential cross section results for $p_{\text{lab}} = 6.234$ GeV/c. 119

B.1 World data for the total cross section for $\bar{p}p$ scattering 120

B.2 Best fit parameters for the world data for the $\bar{p}p$ total cross sections . 125

B.3 World data for the total cross section for pp scattering 128

B.4 Nuclear slope parameter b for pp elastic scattering 131

B.5 Nuclear slope parameter b for $\bar{p}p$ elastic scattering 132

B.6 World data for the ρ-parameter for pp elastic scattering 134

B.7 World data for the ρ-parameter for $\bar{p}p$ elastic scattering 135

Chapter 1

Introduction

The simplest type of reaction between two colliding particles is elastic scattering. However, in the case of pp and $\bar{p}p$ elastic scattering, although many measurements have been made over an extended range of energies and angles, the reaction is still not well understood. Many theoretical models describing elastic scattering have been proposed. These include potential models, and models based on pomeron exchange. However, none of the models successfully describes all observables at all energies. In order to provide discriminating tests of the different models, precision data for as many observables of elastic scattering as possible are needed at all accessible energies.

In this dissertation we present the results of precision measurements of $\bar{p}p$ elastic scattering cross sections in the very small momentum transfer region $0.0004 \leq |t| \leq 0.022$ $(\mathrm{GeV/c})^2$ for incident antiproton momenta in the range 3.5 to 6.2 GeV/c. We use the Coulomb-nuclear interference technique to determine the scattering parameters σ_T (total cross section), b (nuclear slope parameter) and ρ (ratio of the real to imaginary part of the forward scattering amplitude) from the measured shape of the differential cross sections as a function of the square of the four-momentum transfer.

Although there are no theories of hadronic elastic scattering, there is general

agreement that elastic scattering amplitudes must posses the properties of analyticity, unitarity and crossing symmetry. Unitarity leads directly to the optical theorem. It relates the total cross section σ_T to the imaginary part of the forward elastic scattering amplitude. However, the scattering amplitudes may defined with any of several normalizations. If the amplitude in the center of mass frame f_{cm} is defined so that

$$\frac{d\sigma}{d\Omega_{cm}} = |f_{cm}|^2 \,, \tag{1.1}$$

the optical theorem takes the form

$$\sigma_T = \frac{4\pi}{k} \mathrm{Im} f_{cm}(\theta_{cm} = 0) \,, \tag{1.2}$$

where k is the momentum of an incident particle in the center of mass frame. If the amplitude in the laboratory frame is defined so that

$$\frac{d\sigma}{d\Omega_{lab}} = |f_{lab}|^2 \,, \tag{1.3}$$

the optical theorem takes the form

$$\sigma_T = \frac{4\pi}{p_{lab}} \mathrm{Im} f_{lab}(\theta_{lab} = 0) \,, \tag{1.4}$$

where p_{lab} is the momentum of the incident particle in the laboratory frame. An invariant amplitude may also be defined with the normalization

$$\frac{d\sigma}{dt} = |F|^2 \,. \tag{1.5}$$

The optical theorem then takes the form

$$\sigma_T = 4\sqrt{\pi} \mathrm{Im} F(t = 0) \,, \tag{1.6}$$

where t is the square of the four momentum transfer. The different amplitudes are related by

$$f_{lab} = \frac{p_{lab}}{k} f_{cm} = \frac{p_{lab}}{\sqrt{\pi}} F \ . \tag{1.7}$$

Analyticity imposes the requirement that the real and imaginary parts of the scattering amplitude are related in the mathematical way common to all analytic functions. Crossing symmetry states that the scattering amplitudes for pp scattering are related to those of $\bar{p}p$ scattering.

The imaginary part of the forward scattering amplitude is directly determined from the measurement of the total cross section. However, to fully understand the scattering process, it is important to determine the real part of the scattering amplitude as well. There is no analog of the optical theorem which allows a simple means of determining the real part of the forward scattering amplitude. However, the real part can be determined by analyzing the shape of the elastic scattering differential cross sections for very small momentum transfers, i.e., in the (forward) region of small scattering angles. At these momentum transfers the Coulomb and hadronic amplitudes are of comparable magnitude, and their interference results in a characteristic shape of the differential cross sections as a function of momentum transfer.

The Coulomb-nuclear interference technique has been used extensively to determine the real part of the hadronic forward elastic scattering amplitude, or equivalently, the ratio of the real to the imaginary part of the forward amplitude,

$$\rho \equiv \mathrm{Re}F(0)/\mathrm{Im}F(0) \ . \tag{1.8}$$

A determination of the ratio ρ is effectively equivalent to a determination of the real part of the amplitude because the imaginary part can be calculated from the

measured total cross section via the optical theorem. The method was first used for pp scattering in 1964 by Dowel et al. [48], Lohrman et al. [52], and Kirillova et al. [51]. By now the measurements of the pp ρ parameter extend over the momentum range of p_{lab} from 1 GeV/c to 2081 GeV/c ($\sqrt{s} = 62.5$ GeV) These data are displayed in Fig. 1.1a. It was not until 1967 that the interference technique was applied to $\bar{p}p$ elastic scattering by Foley et al. [56] at the AGS at Brookhaven National Laboratory. Since then it has been used to measure the real part of the forward amplitude at incident kinetic energies of 20 MeV ($p_{\rm lab} = 195$ MeV/c) up to collider energies ($\sqrt{s} = 1.8$ TeV, equivalent $p_{lab} = 1.7 \times 10^6$ GeV/c). These results are shown in Fig. 1.1b.

The figure shows that there are large regions of momentum where the ρ parameter is not well measured, or not measured at all. There are very few measurements of the pp ρ parameter below $p_{lab} = 10$ GeV/c. The ones that exist have large errors. In this region, the determinations of the $\bar{p}p$ ρ parameter also have large errors, and values from different measurements which are inconsistent with each other. In the region of p_{lab} covered by the present $\bar{p}p$ measurements. (3.5 – 6.2 GeV/c), the only data are from two series of measurements from 1975 and 1977 CERN experiments by Jenni et al. [57, 58]. Although they have large errors, they suggest a rather large change in ρ in this region. In the present experiment we have measured the ρ parameter in this momentum range with sufficient precision to test the likelihood of such a rapid variation of ρ.

In Fig. 1.1 we also show some of the theoretical predictions for the ρ-parameter. The solid and dashed curves are from dispersion theory calculations [1, 2], and the dotted curves are from an asymptotic amplitude analysis [3]. These are the two techniques which are commonly used to describe the ρ parameter data as a function

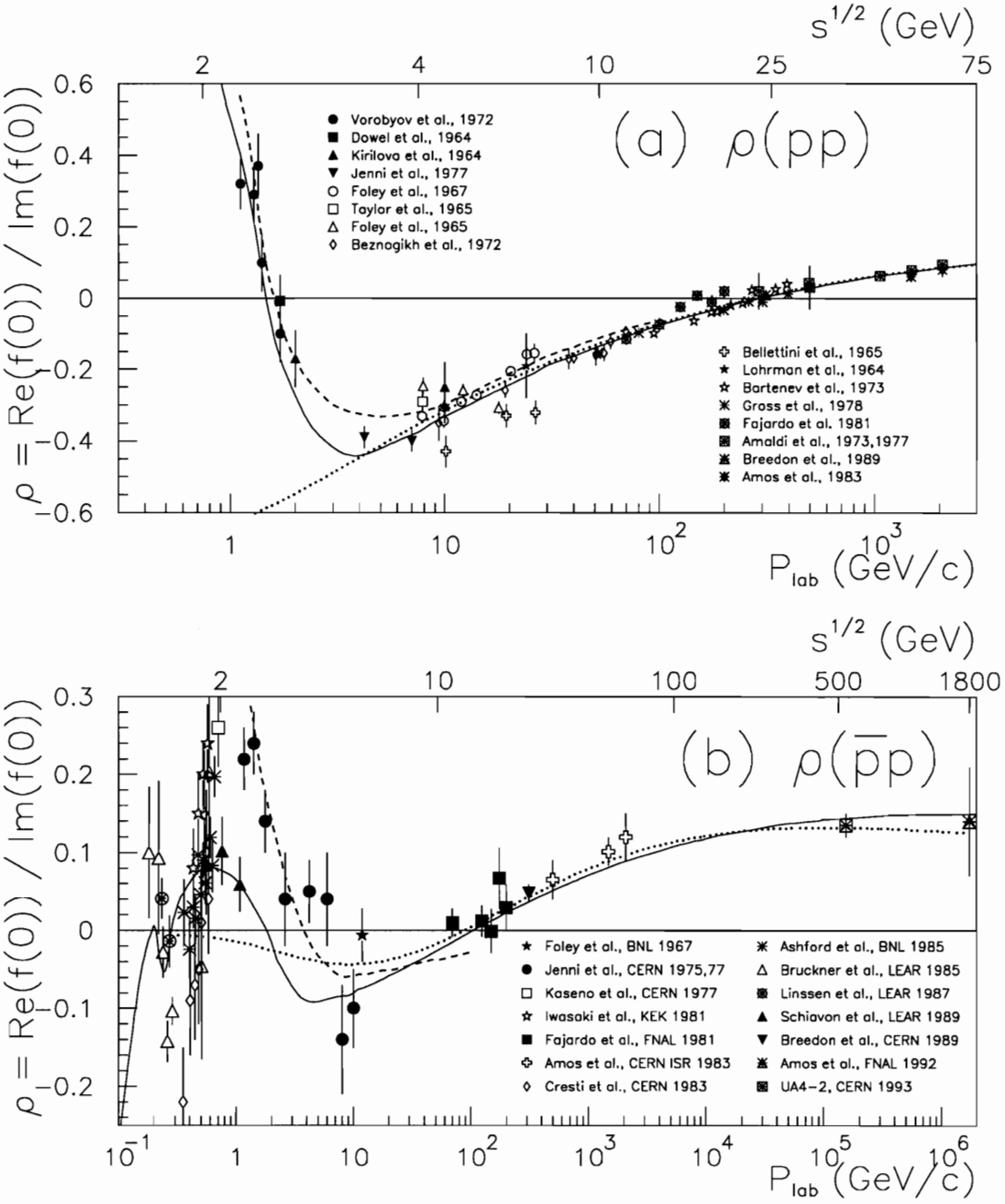

Figure 1.1: Results for the ρ parameter from the literature. (a) pp scattering (b) $\bar{p}p$ scattering. The dashed curves are due to Soding [1], the solid curves are due to Kroll and Schweiger [2], and the dotted curves are due to Block et al. [3]. The data and the references to their sources are given in Tables B.6 and B.7.

of energy. Both of these methods use the properties that the scattering amplitude is an analytic function, that the scattering matrix is unitary, and that the pp and $\bar{p}p$ amplitudes are related by crossing symmetry.

Dispersion theory, which has its origin in optics, provides a means to relate the real part of a complex analytic amplitude to an integral over the imaginary part. The prescription for applying dispersion theory to the complex scattering amplitudes of nucleon-nucleon scattering was given by Goldberger et al. [4] in 1957. Its first application to predict the behavior of the real part of the amplitude for pp and $\bar{p}p$ scattering was made in 1964 in a pioneering paper by Soding [1]. At that time Soding had only fragmentary data on pp and $\bar{p}p$ total cross sections available in the 1 to 10 GeV/c range. Nevertheless, by making plausible assumptions about pole contributions in the unphysical region ($2m_\pi < \sqrt{s} < 2m$) and the asymptotic behavior of σ_T, he was able to obtain the predictions for the ρ parameters shown by the dashed curves in Fig. 1.1(a,b). The near agreement of these predictions with the data, nearly all of which came later, is a remarkable testimony to the validity of the general principles of analyticity, unitarity and crossing symmetry as well as to Soding's intuition. The most recent dispersion theory calculation is that due to Kroll and Schweiger [2]. Its results are shown by the solid curves in Fig. 1.1(a,b).

In 1973 Bourrely and Fischer [5] introduced the idea of constructing analytic amplitudes directly, obtaining their parameters by fitting measured pp and $\bar{p}p$ total cross sections in the non-resonant region, and thereby obtaining an analytic prediction for ρ. This is mathematically equivalent to calculating dispersion relations, since the analytic properties implied in the integral dispersion relations are a priori built in to the scattering amplitudes. The method of constructing analytic amplitudes has the

advantage of being much simpler than evaluating the complex integrals which occur in the dispersion calculations. The method has been greatly refined and developed by Block and his collaborators in a series of articles and reviews [6, 3]. We illustrate their latest prediction by the dotted curves in Fig. 1.1.

Existing data for the ρ parameter have come from two broad classes of experiments. The first consists of forward scattering measurements in which the antiproton beam is incident on a liquid hydrogen target. The second consists of experiments using colliding beams.

The experiments of Jenni et al. [57, 58] are typical examples of the first class. Jenni et al. measured both the pp and $\bar{p}p$ ρ parameter at lab momenta of 1.1 to 10 GeV/c. For the pp scattering measurement they used protons from the CERN PS incident on a 25 cm long liquid hydrogen target. The $\bar{p}p$ measurements were complicated by the fact that antiprotons in the secondary antiproton beam were outnumbered by pions in a ratio of 150:1. The pions and kaons in the beam were discriminated by means of 3 gas-filled Cherenkov counters. The inefficiency of the tagging procedure was estimated to be ~ 1 in 10^5 for pions and ~ 1 in 10^3 for kaons. In order to detect elastic scattering events, the forward region was equipped with a series of proportional chambers and lead-scintillator sandwich counters. Measurements of the differential cross section were obtained at values of $|t|$ down to 0.001 $(\mathrm{GeV/c})^2$. The statistical errors in these measurements ranged from 5% to 15%. Jenni et al. had to also make corrections of up to 16% due to the absorption of particles in the liquid hydrogen target and the production of delta rays from the target. The problems described above led to the large errors shown in the results of Jenni et al. in Fig. 1.1.

With the advent of colliding beams, the ρ parameter was measured at much higher

energies than previously possible. The technique employed was very different from that used with fixed targets. A typical example is provided by the experiment of Amos et al. [61]. In this experiment pp and $\bar{p}p$ differential cross sections were measured in the CERN ISR at total center of mass energies of 30.7 GeV and 62.5 GeV (equivalent $p_{lab} = 501$ and 2081 GeV/c, respectively). In order to detect forward elastic scattering, "Roman pots" were placed downstream from the interaction region in both ISR beam pipes. The Roman pots were devices used to insert small scintillator hodoscopes into the ISR beam pipes close enough to the colliding beams to measure scattering at angles as small as 0.06°. Elastic scattering events were identified by a coincidence between Roman pots symmetrically located with respect to the interaction point. Elastic differential cross section data were collected at values of $|t|$ as low as 0.0007 $(\mathrm{GeV/c})^2$. The ISR delivered luminosity sufficient to obtain good counting statistics.

The present experiment is different from either experiment described above, but contains elements of both. It is a fixed target experiment (like that of Jenni et al.), but it utilizes a 100% pure circulating antiproton beam (like the experiment of Amos et al.). The large flux of antiprotons in the Fermilab Antiproton Accumulator ring together with an internal H_2 gas jet target enables the experiment to obtain an instantaneous luminosity of up to 10^{31} $\mathrm{cm^{-2}sec^{-1}}$. This leads to excellent statistical precision.

In the present experiment, the problems associated with measurements of the elastically scattered antiprotons in the extreme forward direction were avoided by detecting the recoil protons at scattering angles close to 90°. The method of measuring elastic scattering by detecting recoil particles was first used to measure the pp ρ parameter by Lohrmann et al. [52] at CERN in 1964. Also in 1964, Akimov et

al. [7] at the 10 GeV proton synchrotron in Dubna demonstrated the feasibility of using solid state detectors to detect recoil protons from elastic scattering events. These two techniques were combined at the 70 GeV Serpukhov accelerator in 1972 when Beznogikh et al. [47] used an array of solid state detectors to measure elastic scattering recoils. This experiment also pioneered the use of an internal gas jet target in forward elastic scattering measurements. The same technique was used a year later at the 400 GeV proton synchrotron at Fermilab by Bartenev et al. [46]. The experiments of Beznogikh et al. and Bartenev et al. were very similar to the present experiment. Both experiments used a movable array of solid state detectors near 90° to the beam direction to detect proton recoils from an internal hydrogen gas jet target. An excellent review of these experiments is presented by Melissinos and Olsen [8]. The most recent application of this method was in 1988 by Breedon et al. [60] at the CERN SPS at $\sqrt{s} = 24.3$ GeV (equivalent $p_{lab} = 314$ GeV/c).

The present experiment is the latest example of measurements using the recoil technique. By measuring relative differential cross sections in the range where the Coulomb and nuclear amplitudes interfere and fitting the data to a theoretical expression for the differential cross section as a function of the forward scattering parameters, σ_T, b, and ρ, these parameters were determined with high precision. The technique and method of analysis are described in detail in the following chapters.

Chapter 2

The Recoil Technique

In this chapter we present the kinematics of $\bar{p}p$ elastic scattering, the conventional formalism for describing elastic scattering cross sections at forward angles, and the considerations which bear on the design of our experiment to detect proton recoils near 90°.

2.1 Kinematics

The kinematics of $\bar{p}p$ elastic scattering in the lab frame are shown in Fig. 2.1. An antiproton of 4-momentum P_1 collides with a proton at rest resulting in a final state in which the proton and antiproton have 4-momenta P_3 and P_4, respectively. The invariant quantities s, t, and u are defined as

$$s = (P_1 + P_2)^2 = 2m^2 + 2mE_1 \tag{2.1}$$

$$t = (P_3 - P_2)^2 = 2m^2 - 2mE_3 \tag{2.2}$$

$$u = (P_4 - P_2)^2 = 2m^2 - 2mE_4 \tag{2.3}$$

where m is the mass of the proton (as well as the antiproton), and the E_i are the total energies in the lab frame.

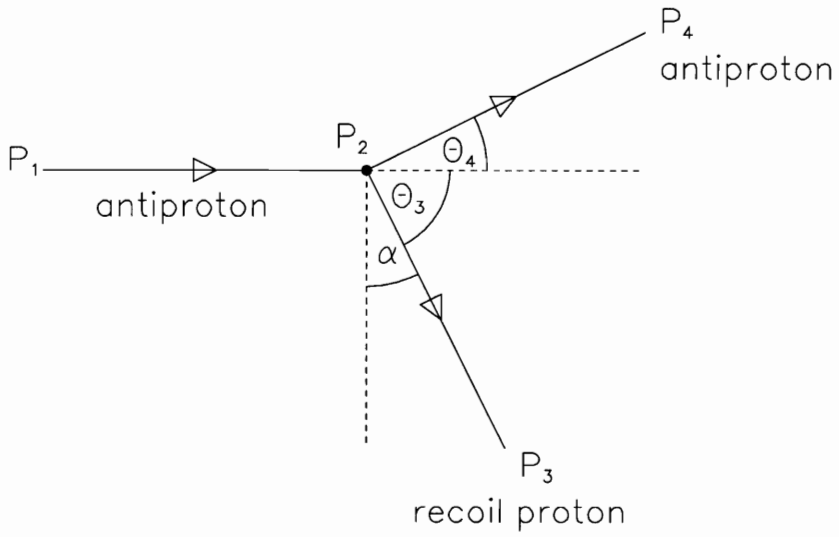

Figure 2.1: Schematic of elastic scattering of an antiproton with 4-momentum P_1 $(E_1, \vec{p}_1)$ by a proton at rest P_2 $(m, 0)$ in the laboratory frame.

The scattering angles of the proton and antiproton, θ_3 and θ_4, respectively, are related to the square of the momentum transfer t by

$$\cos^2\theta_3 = \frac{-t}{4m^2 - t} \times \frac{E_1 + m}{E_1 - m} \tag{2.4}$$

$$\cos^2\theta_4 = \frac{t + 2m(E_1 - m)}{t + 2m(E_1 + m)} \times \frac{E_1 + m}{E_1 - m}\,, \tag{2.5}$$

where E_1 is the total energy of the incident antiproton in the lab frame. In the limit $t \to 0$, we have $\theta_4 \to 0$ and $\theta_3 \to 90°$; i.e., the antiproton goes forward ($E_4 \to E_1$) and the proton recoils at 90° ($E_3 \to m$). In order to describe the angle of the recoil proton relative to its $t = 0$ limit of 90° we define the recoil angle $\alpha \equiv 90° - \theta_3$.

For very small $|t|$ it is difficult to detect the forward scattered antiproton, because it is scattered very close to the beam. It is much easier to detect the recoil proton near 90° to the beam direction. For example, at $t = -0.001$ (GeV/c)^2 and $E_1 = 8.8$ GeV, one would need to detect an 8.8 GeV antiproton at $\theta_4 = 0.21°$. Measurement at such a small forward angle would be extremely difficult. However, for the same value of t, the recoil angle $\alpha = 1.11°$, and the recoil kinetic energy $T = 533$ keV are much more manageable. In addition, in contrast to the antiprotons which scatter in a small cone at forward angles, the corresponding recoil protons are spread over a much larger area in azimuth. A fraction of these recoils can be measured in a small detector, avoiding the large count rate problems which are present in forward angle measurements.

In the present experiment we have chosen to measure elastic scattering by detecting the recoil proton near $\alpha = 0°$. In terms of α, Eq. 2.4 becomes

$$\sin^2\alpha = \frac{\kappa|t|}{4m^2 + |t|}\,, \tag{2.6}$$

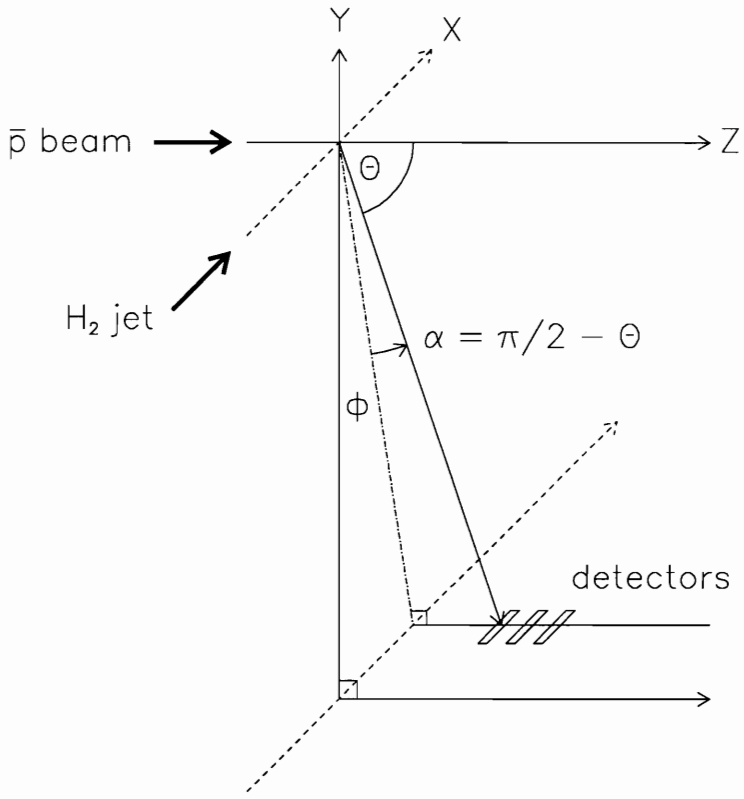

Figure 2.2: Coordinate system in the laboratory frame.

Table 2.1: Relationships between recoil angle, momentum transfer, kinetic energy and proton range in silicon.

	$p_{\rm lab} = 3.5$ GeV/c			$p_{\rm lab} = 8.8$ GeV/c		
α°	$\lvert t\rvert$ (GeV/c)^2	T (MeV)	Range (μm)	$\lvert t\rvert$ (GeV/c)^2	T (MeV)	Range (μm)
1	0.0006	0.337	6	0.0009	0.462	7
2	0.0025	1.346	26	0.0035	1.849	43
3	0.0057	3.031	95	0.0078	4.164	161
4	0.0101	5.390	249	0.0139	7.410	429
5	0.0158	8.429	535	0.0218	11.593	926
6	0.0228	12.147	1000	0.0314	16.720	1740
7	0.0311	16.551	1710	0.0428	22.801	2980
8	0.0406	21.642	2720	0.0560	29.846	4740

where $\kappa = (E_1 + m)/(E_1 - m) = 1/\beta_{cm}^2$ is a weak function of the incident beam energy. Equation 2.2 relates the recoil kinetic energy to the momentum transfer

$$|t| = 2mT \ , \tag{2.7}$$

where T is the recoil kinetic energy. This can be used along with Eq. 2.6 above to obtain a relation between the recoil kinetic energy and the recoil angle

$$T = \frac{2m\sin^2\alpha}{\kappa - \sin^2\alpha} \approx \frac{2m\alpha^2}{\kappa} \ . \tag{2.8}$$

The above relationships between recoil angle, recoil energy and momentum transfer are illustrated in Fig. 2.3 and in Table 2.1. The figures show that the momentum transfer range $|t| < 0.03$ (GeV/c)^2 corresponds to recoil angles $\alpha \leq 6^\circ$, and that the recoil protons have kinetic energies $T < 17$ MeV, and they can be completely stopped in silicon detectors of thickness 2 mm.

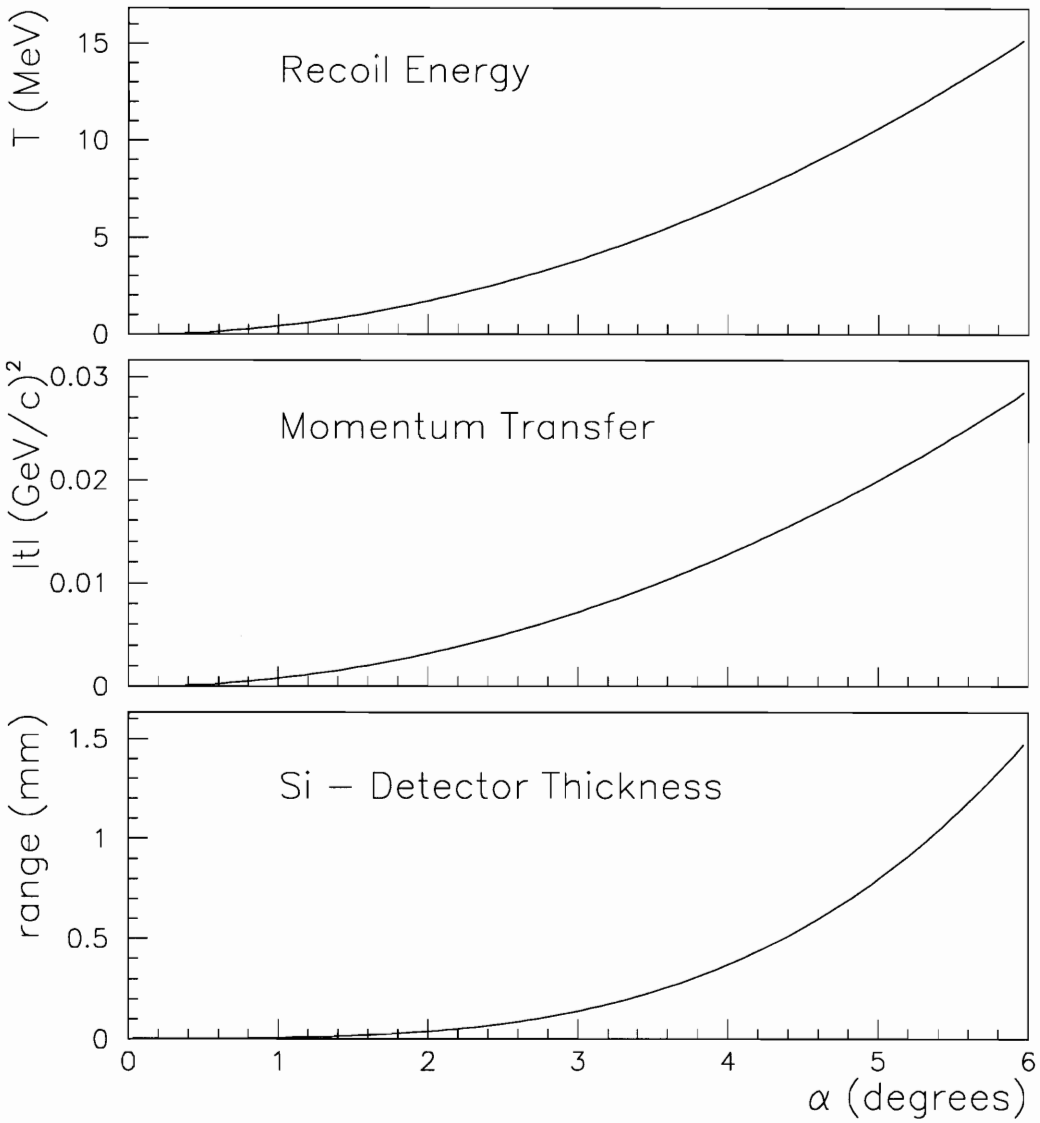

Figure 2.3: Dependence of the recoil proton kinetic energy, momentum transfer and range in silicon on the recoil angle at $p_{\text{lab}} = 6.23$ GeV/c.

2.2 Theoretical Formulation of Forward Angle Elastic Scattering

The $\bar{p}p$ elastic scattering amplitude is expressed as the sum of the amplitudes due to the nuclear (hadronic) and Coulomb interactions, and the phase difference δ between them,

$$F(t) = F_n(t) + F_c(t)e^{i\delta} \ . \tag{2.9}$$

The differential cross section is written,

$$\frac{d\sigma}{dt} = |F(t)|^2 \ . \tag{2.10}$$

The Coulomb amplitude is well known and can be written

$$F_c(t) = \frac{2\sqrt{\pi}\alpha}{\beta|t|}\hbar c G^2(t) \ , \tag{2.11}$$

where β is the laboratory velocity of the antiproton and $G(t)$ is the dipole electromagnetic form factor of the proton

$$G(t) = \frac{1}{(1+|t|/\Lambda^2)^2} \ . \tag{2.12}$$

The parameter Λ is determined by fits to the form factor data and has the value $\Lambda^2 = 0.71$ (GeV/c)^2 [9].

The nuclear amplitude is not well known. There are several models for it. In one very simple model, a purely imaginary potential is assumed with a Gaussian spatial dependence

$$U(r) \propto ie^{-r^2/(2R^2)} \ . \tag{2.13}$$

The scattering amplitude can then be calculated using the first Born approximation

$$f_{n,cm}(\theta) = -\frac{1}{4k\sqrt{\pi}} \int d^3\vec{r}\,' U(r\,') e^{i\vec{q}\cdot\vec{r}\,'}, \tag{2.14}$$

where k is the momentum of either particle in the center of mass frame, and $\vec{q}$ is the three-momentum transfer. The resulting amplitude has an exponential dependence

$$f_{n,cm}(\theta) = f_{n,cm}(0)e^{-(R^2/2)|t|} , \tag{2.15}$$

where the square of the 4-momentum transfer t has been substituted for the square of the 3-momentum transfer $\vec{q}^2$. This approximation is valid for $|t| \ll 4m^2$. Setting $b = R^2$ and converting to the invariant amplitude using Eq. 1.7

$$F_n(t) = F_n(0)e^{-b|t|/2} . \tag{2.16}$$

This simple model reproduces the exponential behavior which is experimentally observed in elastic scattering differential cross sections at forward angles over a wide range of energies (see Fig. 2.4), and is conventionally used to analyze the data for pp and $\bar{p}p$ forward elastic scattering.

The amplitude $F_n(0)$ can be written as

$$F_n(0) \equiv \text{ Re } F_n(0) + i \text{ Im } F_n(0) = \text{ Im } F_n(0)(\rho + i) , \tag{2.17}$$

where we have defined

$$\rho \equiv \text{Re}F_n(0)/\text{Im}F_n(0) . \tag{2.18}$$

Using the optical theorem for the invariant amplitude (Eq. 1.6), we obtain the nuclear amplitude

$$F_n(t) = \frac{\sigma_T(\rho + i)e^{-b|t|/2}}{4\sqrt{\pi}\hbar c} . \tag{2.19}$$

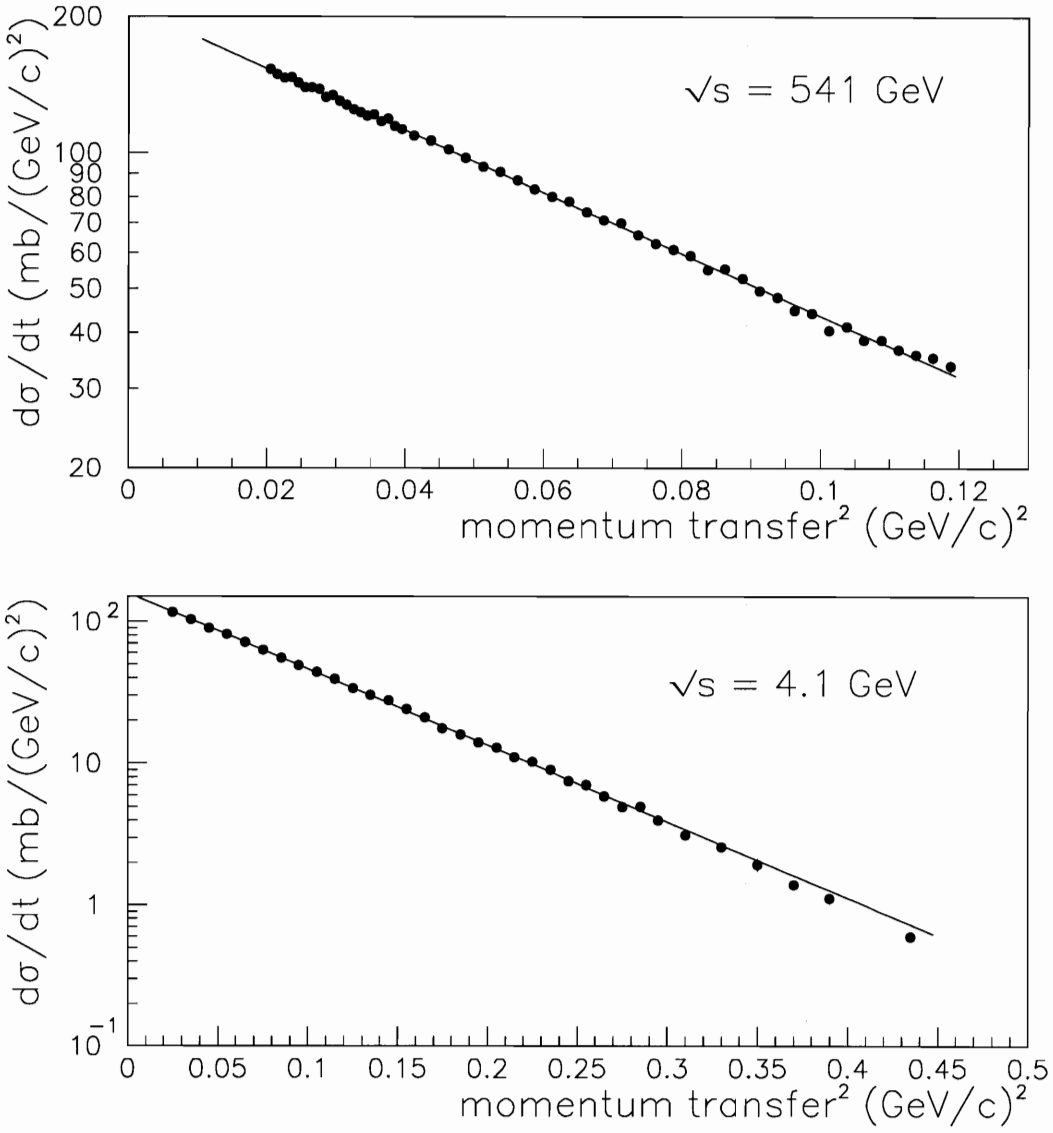

Figure 2.4: Forward angle differential cross sections for $\bar{p}p$ elastic scattering. Data for 4.1 GeV are from Ref. [10]. Data for 541 GeV are from Ref. [70]. Notice the exponential dependence of cross section on the square of the momentum transfer.

The elastic differential cross section is then written as the square of the sum of the two amplitudes

$$\frac{d\sigma}{dt} = |F_C(t)e^{i\delta} + F_n(t)|^2 \,. \tag{2.20}$$

The relative phase δ between the Coulomb and nuclear amplitudes has been calculated in a variety of different ways. We use the parameterization of R. N. Cahn [11]

$$\delta = \alpha\left(\gamma + \log\left(\frac{b|t|}{2}\right) + \log\left(1 + \frac{8}{\Lambda^2 b}\right) + \frac{4|t|}{\Lambda^2}\log\left(\frac{4|t|}{\Lambda^2}\right) + \frac{2|t|}{\Lambda^2}\right). \tag{2.21}$$

where $\gamma \approx 0.577$ is the Euler constant. Expanding Eq. 2.20 results in an expression containing three terms

$$\frac{d\sigma}{dt} = \frac{d\sigma_C}{dt} + \frac{d\sigma_n}{dt} + \frac{d\sigma_i}{dt} \tag{2.22}$$

representing the Coulomb, nuclear and interference contributions, respectively. The individual terms have the following form:

$$\frac{d\sigma_C}{dt} = \frac{4\pi\alpha^2}{\beta^2 t^2}(\hbar c)^2 G^4(t) \tag{2.23}$$

$$\frac{d\sigma_n}{dt} = \frac{\sigma_T^2(1+\rho^2)e^{-b|t|}}{16\pi(\hbar c)^2} \tag{2.24}$$

$$\frac{d\sigma_i}{dt} = \frac{\alpha\sigma_T}{\beta|t|}G^2(t)e^{-b|t|/2}(\rho\cos\delta + \sin\delta) \,. \tag{2.25}$$

Figure 2.5 shows how the three terms in Eq. 2.22 contribute to the differential cross sections assuming typical values of σ_T and b and two different values of ρ. The contribution of the Coulomb cross section (Eq. 2.23) is completely determined by the momentum transfer t, being essentially proportional to $1/t^2$. The nuclear cross section (Eq. 2.24) depends on three parameters σ_T, b, and ρ, which are *a priori* unknown and which must be determined from the experiment. The third contribution (Eq. 2.25) arises from the interference between the Coulomb and hadronic amplitudes.

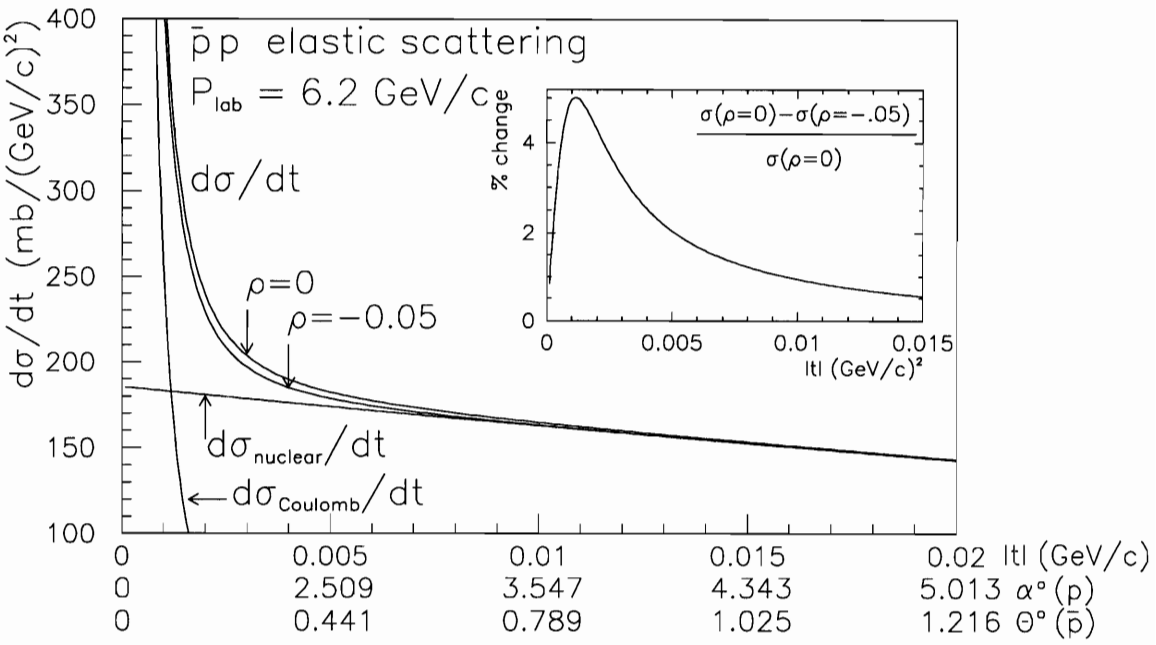

Figure 2.5: Differential cross section predictions for typical values of σ_T, b, and ρ. The nuclear and Coulomb components are shown separately. The horizontal axis is labeled in terms of the momentum transfer t, the recoil angle α and the antiproton scattering angle θ. The inset shows the percent difference between the cross sections for $\rho = 0$ and $\rho = -0.05$.

Figure 2.5 illustrates which ranges of momentum transfer are most useful for determining the different parameters. For $|t| > 0.01$ (GeV/c)^2 the cross section is almost entirely nuclear. This range is ideal for measuring the slope parameter, b. At extremely small $|t|$ ($|t| < 0.0002$ (GeV/c)^2) the Coulomb interaction accounts for 98% of the differential cross section. This region can be used for absolute normalization since the Coulomb cross section is independent of the scattering parameters.

It can be shown that the interference term is of maximum significance at $|t| \approx 0.071$ mb (GeV/c)$^2/\sigma_T$, which is $|t| \approx 0.001$ (GeV/c)^2 in our region of interest. This is illustrated in the inset of Fig. 2.5. We note that the difference between the differential cross sections for $\rho = 0$ and $\rho = -0.05$ is a maximum of $\sim 5\%$ at $|t| = 0.0011$ (GeV/c)^2. It falls rapidly with increasing $|t|$, being only 2% at $|t| = 0.005$ (GeV/c)^2 and $\leq 0.5\%$ at $|t| = 0.020$ (GeV/c)^2.

In the present experiment we have measured $\bar{p}p$ elastic scattering differential cross sections, $d\sigma(\alpha)/d\Omega$ at six different momenta of the incident antiprotons in the range 3.5 to 6.2 GeV/c. The measurements covered the recoil angle range $0.65° \leq \alpha \leq 5.35°$, which correspond to momentum transfer range $0.0004 \leq |t| \leq 0.0022$ (GeV/c)^2. We note that since

$$\frac{dt}{d\Omega} = \frac{p_r^2}{\pi \sin\alpha} = \frac{\sqrt{t(t+4m^2)^3/k}}{4\pi m^2}, \tag{2.26}$$

$$\frac{d\sigma}{d\Omega} = \frac{d\sigma}{dt}\frac{dt}{d\Omega} = \left|\frac{2\sqrt{\pi}}{\beta|t|}\hbar c G^2(t) + \frac{\sigma_T(\rho+i)e^{-b|t|/2}}{4\sqrt{\pi}\hbar c}\right|^2 \frac{\sqrt{t(t+4m^2)^3/k}}{4\pi m^2} \tag{2.27}$$

By comparing the measured $d\sigma(\alpha)/d\Omega$ with the theoretical expression in Eq. 2.27, suitably averaged over the finite geometry of the measurements, we derive the best fit values of the forward scattering parameters, σ_T, b and ρ.

Chapter 3

Experimental Apparatus

The $\bar{p}p$ elastic scattering measurements which form the subject of this dissertation were made in conjunction with Fermilab experiment E760. This experiment was devoted to the precision spectroscopy of the bound states of charmonium, the system containing a charm and an anticharm quark ($\bar{c}c$). The charmonium states were directly formed in $\bar{p}p$ annihilations.

$$\bar{p}p \rightarrow (\bar{c}c)_R \tag{3.1}$$

The experiment was located at the Fermilab Antiproton Accumulator whose circulating antiproton beam was intercepted by a hydrogen gas jet target. In order to measure the luminosity of $\bar{p}p$ interactions a luminosity monitor, based on the detection of recoil protons, was designed. The design of the luminosity monitor was augmented in such a manner that precision measurements of $\bar{p}p$ forward scattering at small momentum transfers could be carried out asynchronously, but simultaneously with the charmonium measurements. We describe the different components of the experimental setup briefly.

3.1 The Antiproton Beam

The Fermilab accelerator complex consists of six major components which were designed to accelerate protons and antiprotons up to energies of 1 TeV. The first stage is the Cockroft-Walton accelerator. In the Cockroft-Walton accelerator H^- ions are accelerated to a kinetic energy of 750 keV. The H^- ions then enter the linac, a 150 m long linear accelerator which increases the kinetic energy of the H^- ions to 200 MeV. Before the particles enter the next stage of acceleration in the Booster, they pass through a carbon foil which strips the electrons from the H^- ions, leaving bare protons. The Booster is a synchrotron, 500 m in circumference, which accelerates the protons to a kinetic energy of 8 GeV. The 8 GeV protons are extracted from the Booster into the Main Ring. The Main Ring is a synchrotron, 6.3 km in circumference, which can raise the energy of the protons up to 150 GeV. When the collider detectors, CDF and D0, are operating, the 150 GeV protons are fed into the Tevatron to be accelerated to 1 TeV. When E760 and the other fixed target experiments are operating (fixed target and collider modes are mutually exclusive), the protons are accelerated to 120 GeV in the Main Ring, and a portion of them are extracted and used to produce antiprotons.

The antiproton source [12] is shown in Fig. 3.1. Antiprotons are produced when the 120 GeV proton beam from the Main Ring is extracted and made to strike a 5 cm tungsten production target. Downstream from the production target, a lithium lens [13] focuses the beam. The lithium lens is simply a cylinder of solid lithium 15 cm long with a radius of 1 cm. An electric current of 0.5×10^6 amps along the axis of the cylinder produces a magnetic field of 1000 T/m in the azimuthal direction. The

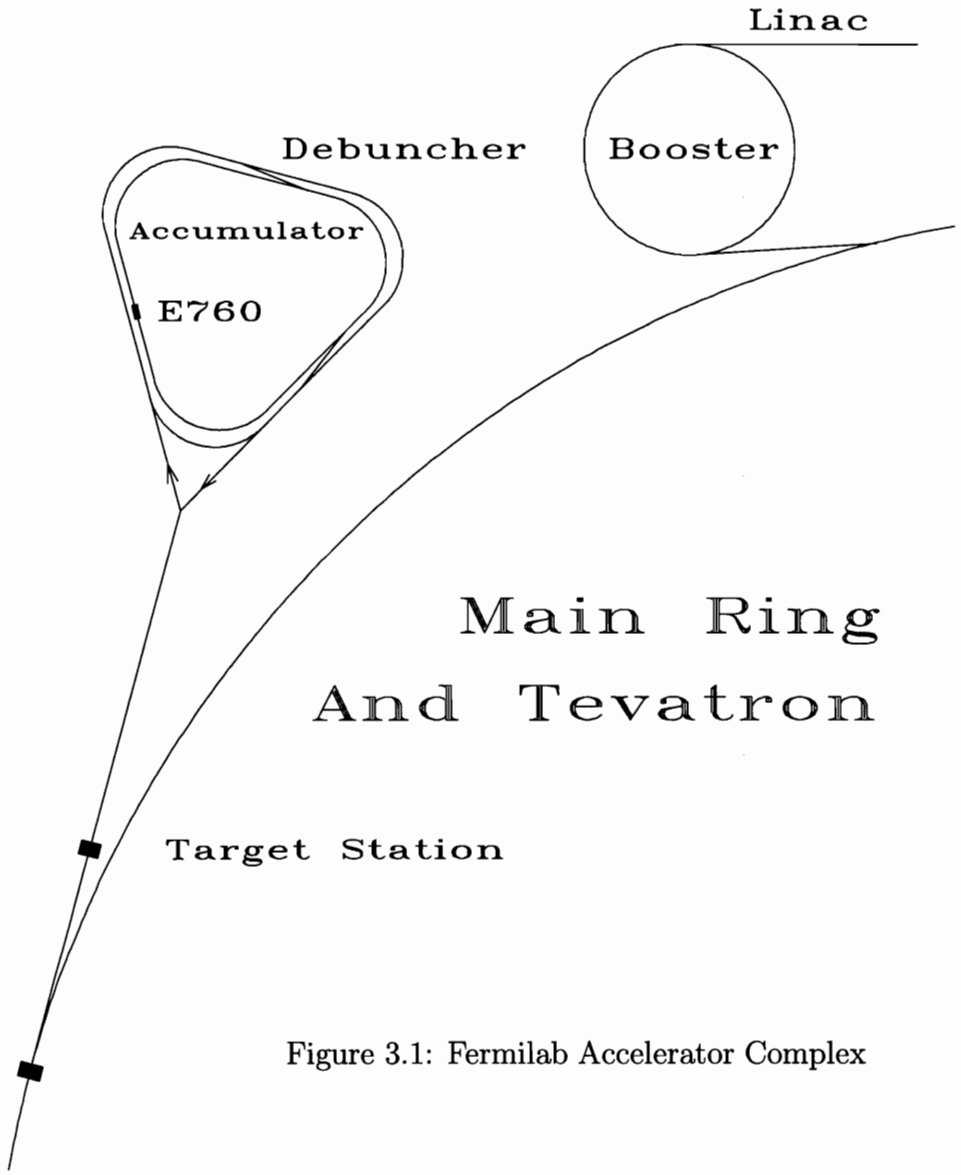

Figure 3.1: Fermilab Accelerator Complex

magnetic field exerts a radial force on the charged particles passing through the lens, producing a focusing effect. This method was found to be superior to conventional magnetic focusing methods for this application [12]. Note that the focusing effect occurs for any conducting material. Lithium was chosen because it is the least dense conductor, and multiple scattering effects and energy loss within the lens are therefore minimized.

After the beam passes through the lithium lens, antiprotons with 8.9 GeV/c momentum are selected magnetically and directed into the 500 m perimeter debuncher ring (the outer ring in Fig. 3.1). At this point, the beam is structured in 84 bunches 1 ns wide separated by 18.9 ns and has a momentum spread of $\sim 3.5\%$. The debuncher reduces the momentum spread by rf debunching of the beam. That is, the spread of the beam in time is increased and the spread in energy is decreased. After 12 ms of rf manipulation in the debuncher, the beam is transferred to the accumulator with a momentum spread of 0.22%.

The accumulator ring is concentric with the debuncher with a slightly smaller perimeter of 474 m (inner ring in Fig. 3.1). The momentum spread of the beam in the accumulator is reduced by a stochastic cooling system [14]. The stochastic cooling system uses a set of "pick-up" electrodes to detect the deviations of particles from the desired orbit (betatron oscillations) and applies a corrective "kick" at the right place and the right time to make the appropriate correction. The "kicker" must be placed an odd number of quarter betatron wavelengths from the pickup in order for the kick to have a net corrective effect. Since there is such a large number of particles in the beam, a particle is also affected by kicks meant for other nearby particles, producing a heating component. However, since the oscillations of the particles are

incoherent, the kicks due to other particles tend to cancel out. Furthermore, the heating component is proportional to the square of the "gain" of the system (the fraction of the deviation corrected per revolution); whereas the cooling is linearly related to the gain [14]. There is therefore an optimum gain which maximizes the net cooling effect.

The stochastic cooling system is used to keep the physical size of the beam small in the directions perpendicular to the direction of propagation (transverse cooling) and also to keep the momentum spread of the beam small (longitudinal cooling). Longitudinal cooling is achieved by applying the principle of transverse cooling in a high dispersion region of the accumulator where the spatial spread of the beam is highly correlated with the momentum spread.

Transverse cooling is important because the smaller the size of the interaction region, the greater the luminosity. It is also very important for the elastic scattering measurements that the size of the interaction region be small. It enables the recoil angle to be defined more precisely. Longitudinal cooling is necessary to obtain the energy resolution needed for charmonium spectroscopy.

The entire process of injecting a batch of antiprotons from the main ring and cooling them in the accumulator takes about two seconds. The antiprotons are then moved to a smaller orbit within the accumulator beam pipe, and the outer area of the pipe is used by the next batch of incoming antiprotons. The process of injection and cooling is repeated every two seconds for about 36 hours until the circulating antiproton beam in the accumulator reaches a current of about 40 mA or 4×10^{11} circulating antiprotons. The beam is then decelerated from the injection momentum of 8.9 GeV/c to the desired momentum for data taking. When the beam is finally

ready to be used for data-taking, it is a continuous (debunched) beam with a revolution frequency of about 0.63 MHz, a momentum spread of $\Delta p/p = 0.05\%$, and a Gaussian spatial distribution with 95% of the beam contained in a diameter of 4.6 mm [15].

The beam energy is measured in terms of the revolution frequency f and the orbit length L,

$$E = m(1 - (Lf/c)^2)^{-1/2} \,. \tag{3.2}$$

The revolution frequency is determined from the Schottky noise spectrum of the circulating beam. The Schottky spectrum is detected by a resonant pickup and is written to tape every 3 to 5 minutes during data-taking. By fitting the Schottky spectrum with a Gaussian function, the revolution frequency can be determined with a precision of 10^{-7}.

The orbit length is determined by scanning the beam energy in discrete steps over the ψ' charmonium resonance [16], the mass of which is known to within 100 keV. At each step, the E760 detector system (see Sec. 3.3 below) is used to count the number of ψ's via their e^+e^- decay. The ψ' production cross section as a function of the total energy in the center of mass frame traces out the Breit-Wigner line shape of the resonance. The precisely known mass of the ψ' (3686.00(9) MeV [17]) provides an absolute energy calibration for the beam. This known energy is then used in Eq. 3.2 along with the revolution frequency (measured as described above) to determine the orbit length (474.046 ± 0.001 m). Once the length of the ψ' reference orbit has been determined, the beam energy at any other resonance is determined by measuring the deviation of the new orbit relative to the reference orbit by means of

48 beam position monitors (BPMs) [18] located throughout the Accumulator ring. The 1 mm uncertainty in the orbit length leads to an uncertainty in the beam energy of $\Delta E/E \approx 8 \times 10^{-5}$. The uncertainty in the beam revolution frequency is negligible.

The stack of antiprotons has a lifetime of about 50 to 90 hours depending on the energy. The finite lifetime is due to the loss of antiprotons as they traverse the H_2 target as well as beam-beam interactions and beam-gas interactions with residual gas present in the beam pipe. The interaction of the beam with the target also causes energy loss, and increases the energy and spatial spread of the beam. This is compensated for by the stochastic cooling system. A stack was typically used for about 1 to 2 lifetimes after which it was dumped and acquisition of a new stack was begun.

3.2 The Gas Jet Target

Proton-antiproton collisions were generated when the circulating antiproton beam crossed a hydrogen jet [19], which was coupled directly to the accumulator beam pipe.

In the gas jet target, hydrogen is injected at a pressure of about 10 bar through a trumpet-shaped nozzle cooled to liquid nitrogen temperature. The diameter of the throat of the nozzle is 37 μm. When the gas passes through the small aperture of the nozzle, it begins a rapid expansion. However, due to the trumpet-shaped geometry of the nozzle, the expansion is slowed, and the hydrogen molecules form clusters. Each cluster contains 10^5 to 10^6 molecules of hydrogen. The formation of clusters is an important advantage. It greatly increases the gas density, increasing the luminosity. In addition, the clusters can travel through the vacuum in straight lines for relatively

long distances without dispersion and without interference from residual gas. This keeps the size of the interaction region small. The trumpet shaped nozzle was chosen specifically for these reasons.

The clusters emerge from the nozzle at high velocity forming a tightly confined jet. However, the distance from the nozzle to the center of the beam pipe is 27.4 cm, and in the traversal of this distance the molecular stream tends to spread. Three skimmers were installed to prevent residual hydrogen present in the outer edges of the stream from reaching the interaction region. Turbomolecular vacuum pumps acting on the region between the nozzle and the beam remove the excess hydrogen from the system. When the stream of molecular clusters crosses the antiproton beam it has a diameter of about 6.7 mm (correpsonding to 95% containment in a diameter of 6.4 mm) and a density of about 3.5×10^{13} atoms/cm^2. After the H_2 stream passes through the antiproton beam another set of turbo pumps remove the excess hydrogen. Pumping speeds of the order of 10^4 liters/second were required to maintain the vacuum in the accumulator beam pipe at a pressure of 10^{-7} Torr. This pressure was much larger than the 10^{-10} Torr standard pressure in the accumulator beam pipe far from the gas jet. The extensive pumping system was required to keep the high pressure localized to the region of the jet target.

3.3 The E760 Detector System

As stated above, the elastic scattering measurements were made in conjunction with Fermilab experiment E760, the purpose of which was to make precision measurements of charmonium states. Charmonium states were resonantly produced in $\bar{p}p$ annihilations and detected via their electromagnetic decay. The measurements were made by

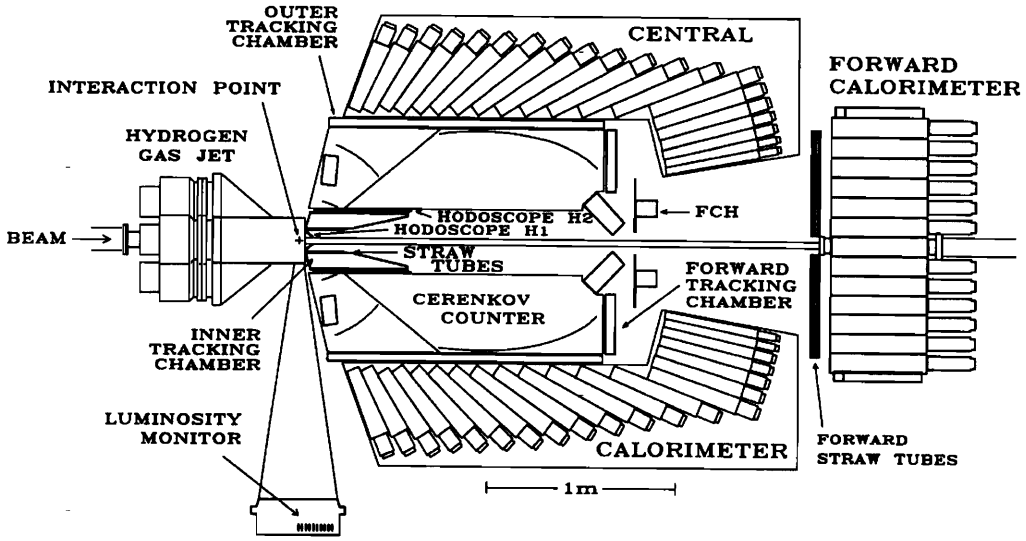

Figure 3.2: Schematic of the E760 detector system.

scanning the energy of the antiproton beam in discrete steps through the mass of the state under study. At each step the event rate in the electromagnetic decay channels was recorded. In this way, the event rate as a function of beam energy traces out the Breit-Wigner line shape of the charmonium state. The high precision of the method results from the excellent energy resolution of the antiproton beam ($\Delta p/p \approx .02\%$), and the extremely small effective thickness of the target.

The detector system used in the charmonium experiment is shown in Fig. 3.2. It has azimuthal symmetry about the beam direction and covers the full 2π azimuth. Its polar angle coverage is from 2° to 70° (where the beam direction is the z-axis and defines the 0° line). Its main components are the scintillator hodoscopes (H1, H2), the Cherenkov counter, the central calorimeter (CCAL) and the charged tracking system; these are briefly described below.

The scintillator hodoscope H1 was the closest detector component to the interaction point. It consisted of 8 plastic scintillator paddles arranged cylindrically around the beam pipe. Similarly, the H2 hodoscope consisted of 32 paddles arranged in a cylinder at a radial distance of 16.5 cm. Both hodoscopes were used in the hardware triggers and to help define charged particle tracks.

In order to distinguish electrons from pions, a gas-filled threshold Cherenkov counter was used [20]. The Cherenkov detector was divided into forward and backward regions covering the angular regions $15° - 38°$ and $38° - 70°$ respectively. Since electrons from charmonium decay have energies which are correlated with their production angle, different thresholds were required in the forward and backward regions in order to efficiently tag the electrons. The forward region was therefore filled with CO_2, while the backward region used freon 13. Both forward and backward regions were divided into octants, symmetrically arranged about the beam pipe.

The most important element in the E760 detector system was the CCAL [21]. The CCAL was an electromagnetic calorimeter consisting of 1280 blocks of lead-glass with a pointing geometry arranged symmetrically about the beam pipe. The glass blocks were placed in 64 identical wedges. Each wedge covered 1/64 of the azimuth and contained 20 glass blocks, each specially constructed to point back to the interaction region. The blocks were each equipped with a photomultiplier to detect light from electromagnetic showers.

The charged tracking system consisted of several elements. The element closest to the beam pipe was a two layer system of straw tubes [22]. Each layer had forty 22 cm long tubes arranged symmetrically about the beam pipe; the axis of the tubes being parallel to the beam. They were filled with an Ar-CO_2-methane mixture, and they

gave both θ and ϕ information. The θ information was provided via charge division along the axis of the tube.

Just beyond the straw tubes was the radial projection chamber (RPC) [23]. The RPC consisted of 80 wires arranged symmetrically about the beam pipe; each wire being parallel to the beam. The chamber was filled with an Ar-ethane mixture. Just beyond the RPC was a multiwire proportional chamber (MWPC). This was filled with an argon-isobutane mixture. The MWPC contained 320 wires in the usual cylindrical arrangement. Both the MWPC and the RPC provided θ and ϕ information. Note that in Fig. 3.2, the RPC and MWPC are referred to collectively as the inner tracking chamber.

Beyond the H2 and Cherenkov counters was the outer tracking chamber, which consisted of two layers of limited streamer tubes (LST) [24] arranged in the usual cylindrical geometry. Each tube was filled with an Ar-CO_2-isobutane mixture and contained conductive strips oriented in such a way as to provide information on θ and ϕ.

The detector system described above was used for identifying electrons and photons resulting from the decay of charmonium states. The CCAL provided the energy measurement with a resolution of $6\%/\sqrt{E}$. The position resolution of the CCAL alone was $\Delta\theta = 7$ mrad and $\Delta\phi = 11$ mrad. For electrons the combined position resolution of the CCAL and the charged tracking was $\Delta\theta = 4$ mrad and $\Delta\phi = 7$ mrad.

The detector system was not directly used in the elastic scattering analysis, however it was used for several supporting measurements. In addition to the detector system described above, the installation included a luminosity monitor based on the

principle of detecting protons recoiling at a scattering angle of $\theta_3 = 86.453(6)°$ ($\alpha = 3.547°$), corresponding to antiprotons which are elastically scattered at $\theta_4 = 1.106(2)°$. The apparatus for measuring the forward elastic scattering parameters was designed as a part of this luminosity monitor and is described in the next section.

3.4 The Detector System for Proton Recoils

The luminosity monitor [25] was designed to measure forward elastic scattering relative differential cross sections in the recoil angle range $\alpha = 0° - 8°$, with a precision of 1 to 2%. If reliable measurements could be made to α as small as 0.5° ($[d\sigma_C/dt]/[d\sigma/dt]$=0.98) absolute cross section normalization would follow trivially, and all three parameters, σ_T, b, and ρ could be directly determined. If measurements at such small angles were found to be not possible, it was hoped that it would still be possible to determine the absolute normalization of the differential cross sections by using the value of σ_T from a fit to the world data, and determining b and ρ by analyzing the shape of the relative differential cross sections.

3.4.1 The Design Criteria

The above objectives dictated the following design criteria for the elastic scattering detector system.

a. It should be able to measure $\bar{p}p$ *relative* cross sections with errors of the order of a percent in the entire range from $\alpha \approx 0.5°$ to 8°.

b. It should consist of detectors at fixed values of α, and detectors which can be moved to any value of α in the range $\alpha = 0°$ to 8°.

c. All detectors should be able to see the full interaction volume. It was expected that the interaction volume would consist of the intersection of a cylindrical gas jet of ~8 mm diameter with a perpendicular antiproton beam of similar dimensions. Henceforth, we refer to the centroid of the interaction volume as the interaction 'point'.

d. Because of the rapid variation of $d\sigma/dt$ in the small t region, each detector should subtend only a small range of recoil angles, $\Delta\alpha < 1°$ at the interaction 'point'.

e. It should be possible to make frequent energy and solid angle calibrations of the solid state detectors *in situ* with an alpha source.

With these criteria in mind, the detector assembly was designed to have up to two fixed detectors (see Sec. 3.4.3), and up to eight detectors linearly arranged on a movable carriage at ~150 cm vertical distance from the interaction 'point'. The vertical distance from the detectors to the interaction point was adjusted so that the one inch distance between detectors on the carriage corresponded to $\Delta\alpha \approx 1°$, and the detectors were nominally at angles of 1°, 2°,$\cdots$, 7°, 8°. The carriage had a total range of movement of 8 inches, so that each detector could be placed anywhere within the range α(nominal) to α(nominal)-8 degrees. For example, the detector in slot number one could be moved from $\alpha = 1°$ down to $\alpha = -7$ degrees.

The assembly was to be coupled directly to the beam pipe, and all detectors were to be able to have line-of-site to the full interaction region through an aperture in the beam pipe. The solid state detectors were to have nominal active areas of ~ 1 cm $\times$ 5 cm each. Because of their better tolerance to the ambient hydrogen atmosphere and

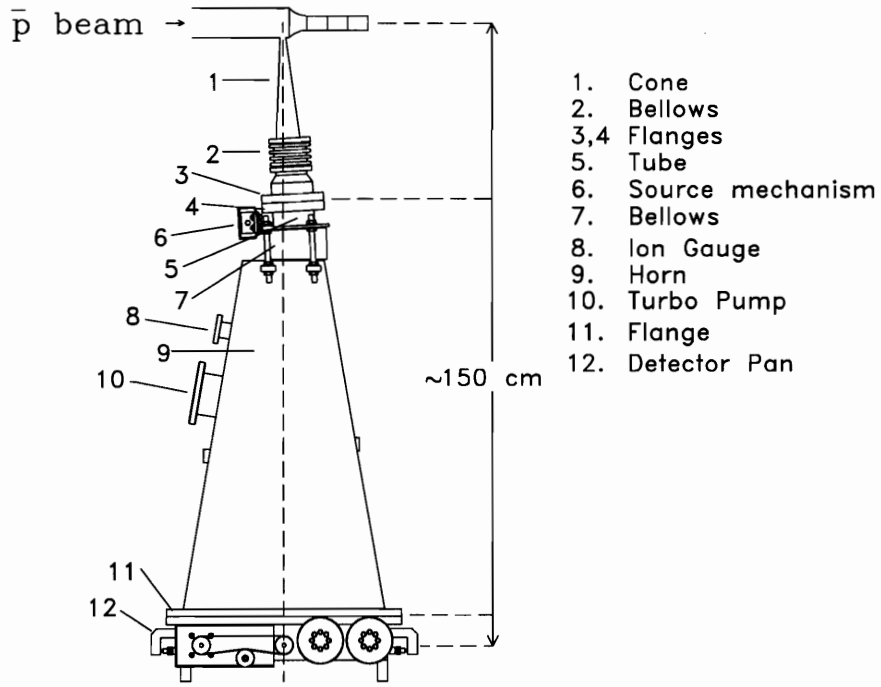

Figure 3.3: Schematic view of the apparatus for detecting proton recoils.

their greater radiation resistance, ion-implanted silicon detectors of 500 μm depletion depth were chosen for use at angles $\alpha \leq 4°$. For larger angles lithium-drifted silicon detectors of 3000 μm were chosen [26] (see Table 2.1). Both types of detectors had the same external dimensions, 72 mm $\times$ 17.5 mm $\times$ 14 mm, with rear-mounted microdot connectors. The apparatus is described in more detail below.

3.4.2 The Mechanical Assembly

A schematic view of the apparatus is shown in Fig. 3.3. It consists of three main parts.

a. The first part is permanently attached to a 12 mm aperture in the beam pipe below the interaction region. It consists of a 25 cm long conical piece (#1) which is welded to the accumulator beam pipe, a 3" outer diameter (OD) bellows section (#2), and a 4" OD flange (#3). The aperture in the beam pipe was kept small because of geometrical considerations, and also in order to keep the vacuum in the beam-target region relatively isolated from the vacuum in the horn (# 9).

b. The second part of the apparatus consists of the horn assembly. It is essentially a tall vacuum vessel made of 3/8" thick plates of 304 stainless steel (#9). It is coupled to flange #3 via an identical flange (#4), a 4" OD tube (#5) which has a penetration for an alpha source insertion device (#6), and an adjustable length 6" diameter bellows (#7). A vacuum pump port (#10) for a 120 liter/second turbo pump and an ion gauge port (#8) are also provided in the horn. The bottom flange of the horn (#11) is rectangular and mates with the corresponding flange at the top of the detector pan.

c. The third part consists of the detector pan (#12), which is shown in detail in Fig. 3.4. The detector pan is an open rectangular box made of stainless steel plates of 1/4" thickness (sides) and 3/8" thickness (bottom). Its inside dimensions are 49.5 cm $\times$ 16.5 cm $\times$ 9.5 cm. It is topped by a 3/4" thick flange which has a rectangular groove to accommodate either a standard Viton O-ring or an OFHC (oxygen-free high conductivity) copper seal for high vacuum coupling to the horn assembly. The pan contains the detector carriage and the fixed detector platform.

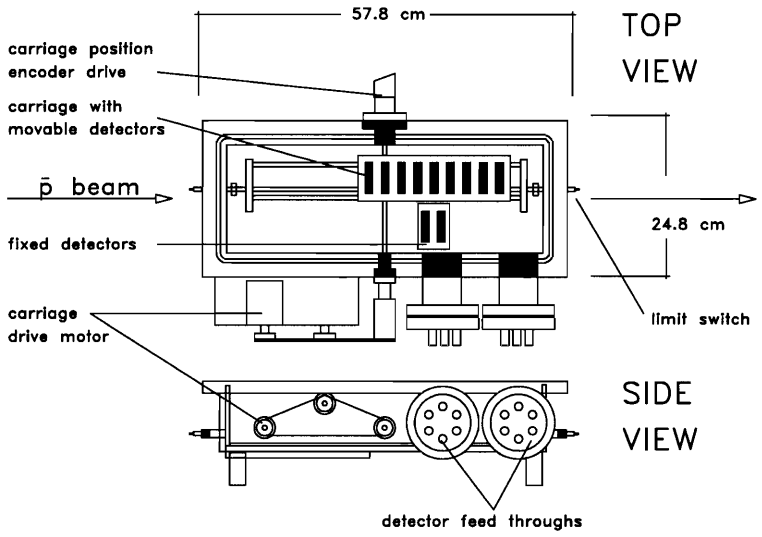

Figure 3.4: Schematic view of the detector pan

The fixed detector holder consists of two 1/8" thick plates between which up to two solid state detectors can be sandwiched. The lower plate is made of aluminum and has grooves to accurately anchor the detectors (each with outer dimensions 72 mm $\times$ 17.5 mm $\times$ 14 mm) and holes to allow passage of the signal cables. The upper plate is made of 304 stainless steel and has a large cut-out to allow the detectors free line-of-sight to the interaction region. The fixed detectors are positioned at $\alpha \approx 2.5°$ and $\alpha \approx 3.5°$.

The movable detectors are mounted on a carriage which can be moved from outside the pan. The carriage consists of an aluminum slide plate with appropriate grooves at the bottom, and a stainless steel clamping plate with a large cut-out at the top. Between the two plates up to eight detectors can be sandwiched in accurately machined positions. The detector positions are designed to be $\sim 1°$ apart.

The carriage inside the detector pan can be moved parallel to the beam direction by means of a rack and pinion arrangement (see Fig. 3.4) which is driven from the outside of the pan by a stepping motor (Superior Electric M063-FC06). The drive motor operates via feedthroughs and bearings for proper operation under vacuum. On the other side of the pan a 10-bit absolute position encoder (BEI series T25 [27]) is driven by a similar mechanism and measures the distance traveled by the carriage. The physical end of the linear motion of the carriage is signaled by limit switches at each end of the pan. When a limit switch is activated, power to the stepping motor is cut off.

Detector bias voltages and the return signals from the detectors are fed through two DEL-SEAL 4" OD flanges, each with 6 HSV feedthrough connectors [28].

The alpha source can be moved inside the horn via bellows which couple the horn vacuum to the outside. The vacuum side of the bellows is sealed and is movable. It is coupled to a rod, the far end of which has the provision to attach a standard radiation source holder. Normally, a spring loaded mechanism keeps the bellows at natural extension and the source retracted in its housing. When needed, an actuator, consisting of a standard air cylinder piston driven by a 12 V DC solenoid, extends the bellows and brings the source to the center of the top flange of the horn. Limit switches indicate the position of the source.

The position of the detectors was determined by a surveying team. The vertical distance between the interaction point and the surface of the detectors was found to be 146.90(3) cm. Note that detectors on the movable carriage are at the same height as the fixed detectors. The transverse horizontal position with respect to the vertical (x-coordinate in Fig. 2.2) of the fixed detector is -5.555 cm and that of the movable

carriage is 2.451 cm. The position of any detector on the carriage along the beam direction depends on the position of the carriage.

3.4.3 The Solid State Detectors

As illustrated in Fig. 2.3, recoil protons in the recoil angular range $\alpha \leq 6°$ have kinetic energies up to about 15 MeV. Total energy loss solid state detectors are ideal for detecting charged particles in this energy range. They can be made small enough to obtain the position resolution necessary to measure the shape of the differential cross sections at small $|t|$, they provide excellent energy resolution and signal to noise characteristics, and they are 100% efficient for charged particle detection.

A silicon semiconductor detector is a diode of the p-n type operated in a reverse bias mode. In such a device the barrier created at the p-n junction reduces the leakage current to a low value. Thus, a sufficient electric field can be applied across it so as to collect charge carriers liberated by ionizing radiation.

A solid state detector provides a signal proportional to the energy lost by a charged particle during its passage through the detector. If the depletion depth of the detector is large enough to completely stop the particle, the signal is proportional to the total (kinetic) energy of the particle minus the (very small) energy loss in the "dead layer" on the face of the detector. The full depletion depth of the detector is realized by applying a sufficiently high reverse bias to collect all the charge carriers created by the ionizing radiation.

The solid state detectors [26] used were of two types: lithium-drifted and ion-implanted. The ion-implanted detectors are generally more rugged. They have smaller dead layers at entrance, smaller leakage current, less sensitivity to surface

conditions, and less susceptibility to radiation damage. However, they are limited to depletion depths of less than 1 mm. When larger depletion depths (i.e., more stopping power) are needed, lithium drifted detectors must be used.

Table 2.1 shows the thickness of silicon needed to stop protons scattered at α up to 8°. For recoil angles $\alpha < 4°$ the proton recoils can be completely stopped in silicon detectors of thickness $\leq 500\mu$m. The first four slots on the carriage (used at angles $\alpha < 4°$) as well as the fixed mounting at $\alpha = 3.5°$ were therefore provided with ion-implanted detectors with a 500 μm depletion depth. Slots 5 and 6 on the carriage (covering larger angles) were provided with lithium-drifted detectors with a 3000 μm depletion depth.

In order to obtain reasonable count rates it was decided to have detectors with areas as large as possible. Since we wished to keep $\Delta\alpha$ small ($\approx 0.4°$), we wanted $\Delta\phi$ to be as large as possible. This led to the choice of detectors of a rectangular surface. As specified by the manufacturer, the ion-implanted detectors have nominal active areas of 1.2 cm $\times$ 4.8 cm. The lithium-drift detectors have nominal active areas of 1.0 cm $\times$ 5.0 cm. Each ion-implanted detector has an entrance window of 0.05 μm of aluminum and a 0.15 μm thick layer of inactive silicon. The lithium-drifted detectors have entrance windows of 0.05 μm of gold and 0.3 μm thick layers of inactive silicon. At the bottom of each detector there is a microdot connector through which bias voltage may be applied and the output signal collected.

3.4.4 Detector Performance

In preparation for this experiment a total of eight ion-implanted detectors and three lithium-drifted detectors were purchased, although only five ion-implanted and

Table 3.1: History of the performance of the solid state detectors.

Ion-implanted detectors				**Ion-implanted detectors**			
Thickness		500 μm		Thickness		500 μm	
Active dimensions		12 mm × 48 mm		Active dimensions		12 mm × 48 mm	
Entrance window		500 Angstroms Al		Entrance window		500 Angstroms Al	
Dead layer		1500 Angstroms Si		Dead layer		1500 Angstroms Si	
Purchased		7/27/1987		Purchased		10/18/1990	
Serial	Resistivity Ωcm	Bias Volts	Leakage nA	Serial	Resistivity Ωcm	Bias Volts	Leakage nA
6492	9760	100	275	8582	16300	110	210
	Used in 1988 run. Excessive leakage, 10/1989. RETURNED to Enertec. Replacement 6492′ received.				Used in 1990,1991 runs. Still good.		
6492′	16300	100	330	8583	16300	110	270
	Used in 1990 run. Drift, 10/1990. RETURNED to Enertec. Replacement due.				Poor resolution, 10/1990. RETURNED to Enertec. Replacement due.		
6493	8800	110	300	**Lithium-drifted Detectors**			
	Used in 1989, 1990, 1991 runs. Still good.			Thickness		3000 μm	
6494	9760	100	250	Active dimensions		10 mm × 50 mm	
	Used in 1989, 1990, 1991 runs. Still good.			Entrance window		500 Angstroms Au	
				Dead layer		3000 Angstroms Si	
				Purchased		3/2/1988	
6495	10080	100	—	9124	—	300	4500
	Excessive leakage, 3/1989. RETURNED to Enertec. Replacement 6495′ received.				Excessive leakage, 11/1989. Replacement 9124′ received.		
6495′	—	100	130	9124′	—	300	8000
	Used in 1990,1991 runs. Double peak 8/1991. Apparently recovered, 1/1994.				Big bump, 10/1990. RETURNED to Enertec. Replacement due.		
6506	10080	100	250	9125	—	700	3800
	Used in 1989,1990,1991 runs. Still good.				Used in 1989,1990,1991 runs. Vacuum failure, 6/1991.		
6507	10080	100	200	9126	—	300	5100
	Used in 1988 run. Excessive leakage, 11/1989. RETURNED to Enertec. Replacement 6507′ received.				Used in 1989,1990,1991 runs. Still good.		
6507′	16300	70	330				
	Drift, 10/1990. RETURNED to Enertec. Replacement due.						

two lithium-drifted detectors were used in the data runs. Table 3.1 gives the history of the performance of all of the detectors used in the data runs and the preliminary testing of the apparatus. The detectors were used at room temperature at a typical pressure of $\sim 10^{-7}$ Torr. Table 3.1 shows that nearly half of the detectors had serious problems develop at one time or another.

A detector may experience problems for several reasons. The main reasons include the following:

a. a "short" for any reason between its front and back surfaces. This shows up as a sharp rise in the leakage current and an inability to support bias.

b. an alteration of the "surface states". This is the catch-all phrase. It means everything from scratches and smudges on the surface of the detector to alteration of the chemical nature (e.g., reduction) of the rectifying contact at the detector surface. This shows up as a gradual deterioration of the energy resolution as well as an increase in the leakage current.

   There is no deep understanding of the above phenomenon. It is known that the detectors deteriorate when subjected to high vacuum over long periods. Neither "high vacuum" nor "long periods" are well defined. However it is also known that a detector so damaged tends to recover when allowed to rest for some time in normal atmosphere. It is worth noting that one detector manufacturer (ORTEC) expressly cautions "do not expose the detector to reducing atmosphere, such as hydrogen gas"!

c. The high degree of perfection of a semiconductor crystal makes semiconductor detectors subject to radiation damage. Radiation causes changes in the crys-

tal lattice and the introduction of carrier trapping and recombination centers. These produce changes in noise, carrier lifetime, sensitive depth, reverse leakage current, and energy resolution. One characteristic effect of radiation damage is to produce secondary peaks on the low energy side of a spectral peak. For silicon detectors the half-mortality rate with proton radiation is estimated to be $\sim 10^{10}$ proton/cm^2 [29].

d. Finally, it should be noted that the band gap in silicon is weakly sensitive to temperature changes. The pulse height from ^{241}Am alphas (5486 keV) increases by about 1 keV/°C near room temperature.

The most common problem which was observed during our use of the detectors was a gradual increase in leakage current and noise, and the eventual inability to support the required bias voltage. This may have been due, in part, to the harsh environment in which they were used (see item b above).

One of our detectors (6495′, see Table 3.1) exhibited the typical radiation damage symptom, i.e., secondary peak development. Although integrated charged particle exposure was calculated to be only $\sim 10^9$ (protons and alphas), the estimated total radiation exposure near the detectors was $10 - 50$ rads. In Fig. 3.5 the gradual worsening of the performance of this detector and its eventual recovery are illustrated.

The bias voltages and typical leakage currents for the detectors which were used in the final data run are shown in Table 3.2. Note that the first column of the table is an index number for each detector and refers to the detector's position on the carriage (see Sec. 3.4). The table also shows typical values of each detector's energy resolution. These were measured by taking the full width at half maximum of the

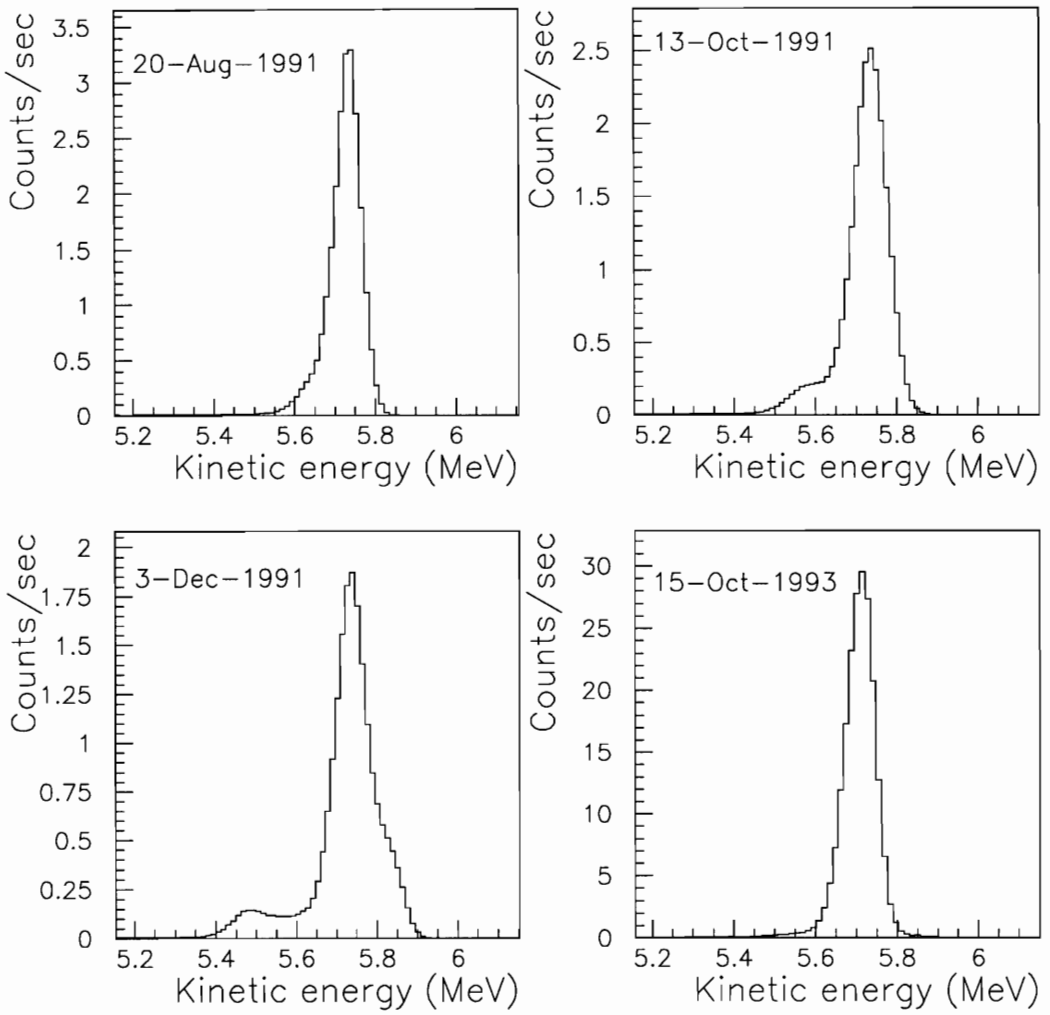

Figure 3.5: The effect of radiation damage on the alpha spectrum of one of the detectors.

Table 3.2: Detector characteristics and performance.

Detector	α°_{max}	Thickness (μm)	Bias (Volts)	Current (nA)	Resolution (keV)
1	1.0	500	100	710	115
2	2.0	500	110	230	73
3	3.0	500	100	210	92
4	4.0	500	100	330	97
5	5.0	3000	300	10100	130
6	6.0	3000	700	6900	120
fixed	3.5	500	100	160	100

alpha particle spectrum acquired with the ^{244}Cm source (see Sec. 4.1).

3.4.5 The Data Acquisition Electronics

The block diagram of the rather conventional electronics used with the detectors is shown in Fig. 3.6. Note that only one detector line is shown explicitly.

Bias voltage was supplied to the detectors by two ORTEC 210 Detector Control Units [30]. Each of these can supply up to 1000 V to four detectors, as well as measure detector leakage currents.

Bias was supplied to the detectors through two Tennelec TC 178 [31] quad preamplifiers. In order to keep the cable length between the detectors and the preamplifiers as short as possible, the preamplifiers were placed less than 1 m from the solid state detectors. The outputs from the preamplifiers were brought up to the counting room to two Enertec 7175 [26] four-channel amplifiers.

Two Tennelec TC 178P [31] quad pulsers were used for testing and calibration. In addition, a precision 60 Hz mercury relay pulser was also used for calibration.

The signals from the eight amplifiers were fed into a Nuclear Data ND588 analog

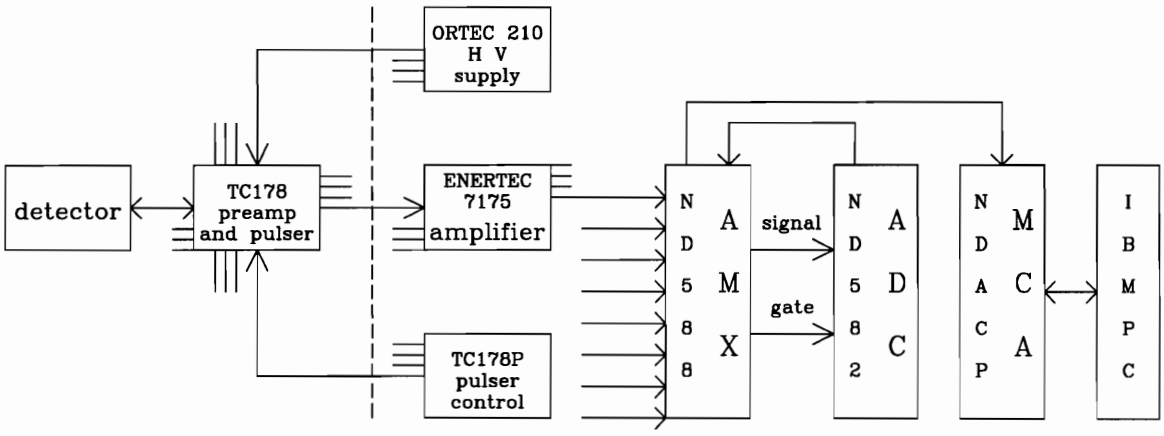

Figure 3.6: Block diagram for the luminosity monitor electronics

multiplexer (AMX) [32] which in turn fed a single ND582 [32] ADC. The AMX checks each of its 8 inputs at a rate of 2.5 MHz until it finds an incoming signal. It then passes this signal to the ADC. The ADC digitizes the signal's peak amplitude and then sends the digital information back to the AMX. The AMX then sends the pulse height information, as well as the bits identifying the input from which the signal came, to the Nuclear Data NDACP Micro- Multichannel Analyzer (MCA). The MCA stores all 8 spectra, each binned into 512 channels. The spectra can be read out at will and displayed on an IBM PC.

The ADC contains a dead time circuit which determines the fraction of time during which it is busy, and this information was stored with the data. However, since the count rate typically did not exceed 100 Hz, the dead-time correction was negligible.

Chapter 4

Calibrations

As described in Sec. 3.4, precision in the measurement of the forward elastic scattering parameters depends on the precision with which the energy of the recoil protons is measured and the precision with which the relative solid angles subtended by the different detectors at the interaction point are measured. In this chapter we describe how the calibrations required for these measurements were made.

4.1 Energy Calibration

The absolute energy calibration of the detectors is based on the energy of the alpha particles from a 12 μCi ^{244}Cm alpha source, the pedestal of the ADC, and the pulse height linearity of the detector electronics.

The alpha source consists of a 4 mm diameter spot of curium oxide, electrodeposited and diffusion bonded onto a 0.005" thick platinum foil. The curium is covered with a layer of sputtered gold of thickness 100 μg/cm^2.

The alpha radiation from ^{244}Cm is emitted essentially with two energies, 5805 keV (76%) and 5763 keV (24%). The detector system is not capable of resolving the two lines at 5805 keV and 5763 keV (see Fig. 4.1), and in all calculations the weighted

average 5795 keV is used. In the spectrum the additional small peak at 5168 keV is due to the alpha decay of ^{240}Pu, which is the daughter nucleus of ^{244}Cm decay.

The gold covering on the alpha source causes $\sim$ 24 keV of energy loss. The entrance windows and dead layers of the detectors cause additional energy losses of $\sim$ 29 keV for the ion-implanted detectors and $\sim$ 65 keV for the lithium-drifted detectors. The effective alpha particle energy is therefore 5742 keV for the ion-implanted detectors and 5706 keV for the lithium-drifted detectors. The uncertainty in the thickness of the dead layers contributes to the overall systematic error of the measurements. From discussions with the manufacturer of the detectors, we estimate that there is a 25% uncertainty in the thickness of the detector dead layers. By varying the dead layer thickness by $\pm$25% and recalculating the energy calibration (see below), it was found that the corresponding uncertainty in the measured recoil proton energy is $\leq 0.2\%$.

The detector system was calibrated when the experiment was not taking $\bar{p}p$ data by moving the ^{244}Cm alpha source into position over the detectors. The count rate seen by the detectors was about 25 cts/sec. A typical calibration run lasted for about 24 hours, giving a statistical accuracy of $< 0.1\%$ in the calibration spectrum. In the calibration spectrum shown in Fig. 4.1, the main alpha peak at $(5795 - 24 - 29 =)$ 5742 keV and the ^{240}Pu peak at $(5168 - 24 - 29 =)$ 5115 keV are clearly visible above a background which is more than three orders of magnitude smaller.

The channel corresponding to the ^{244}Cm alpha peak was determined by calculating the weighted mean in the 5-channel region centered on the channel containing the maximum number of events. This method determined the position of the ^{244}Cm peak to within < 0.1 channels.

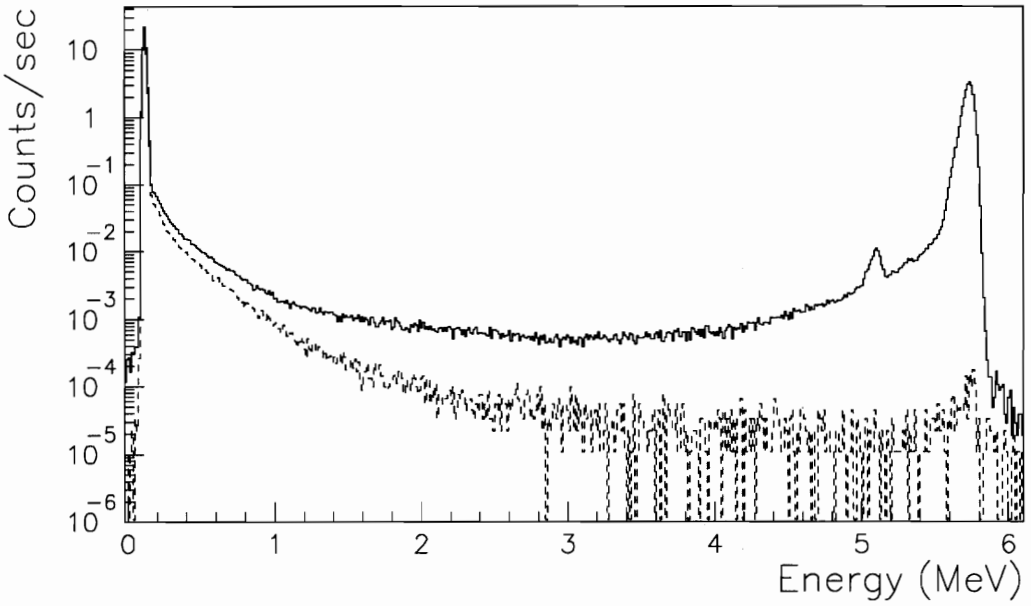

Figure 4.1: The solid line shows a typical energy spectrum from the ^{244}Cm alpha source. The dashed line shows a background spectrum taken with the source withdrawn.

In order to obtain an energy calibration over an extended range, it was necessary to obtain at least one calibration point in addition to that of ^{244}Cm, and to calibrate the linearity of the system. In our case the only other calibration point possible was that corresponding to zero energy, i.e., the ADC pedestal channel.

The ADC pedestal channel was determined using two different methods. In the first method the signal cables were disconnected from the ADC, and the internal strobe of the ADC was used to calibrate the zero offset. In this mode the ADC digitizes whatever DC bias level is present at the signal input at an internally controlled rate. The resulting energy spectrum showed that data accumulated entirely in a single channel. The ADC zero offset was then adjusted until the pedestal occurred in ADC channel number three.

In the second method a 60 Hz precision mercury relay pulser was connected to the preamplifier input. To simulate the effect of a typical detector capacitance a 180 cm length of RG58 cable (0.98 pf/cm) was also attached to the preamplifier input. The input pulse height was varied to obtain pulser peaks spanning the full range (512 channels) of the ADC. The peak channel numbers were then fit to a straight line as a function of pulser setting to determine the pedestal channel. The average pedestal for the eight detector lines was found to be 3 ± 1 channels, in agreement with that obtained by the method described above.

The two points determined by the alpha peak and by the ADC pedestal were used to calculate the calibration line, assuming the system was linear over its entire range. The system linearity was tested over the full range of the ADC by using the 60 Hz precision pulser, as mentioned above. The relation between pulser setting and ADC channel was very well fit by a straight line. The deviation of the data from the fit is

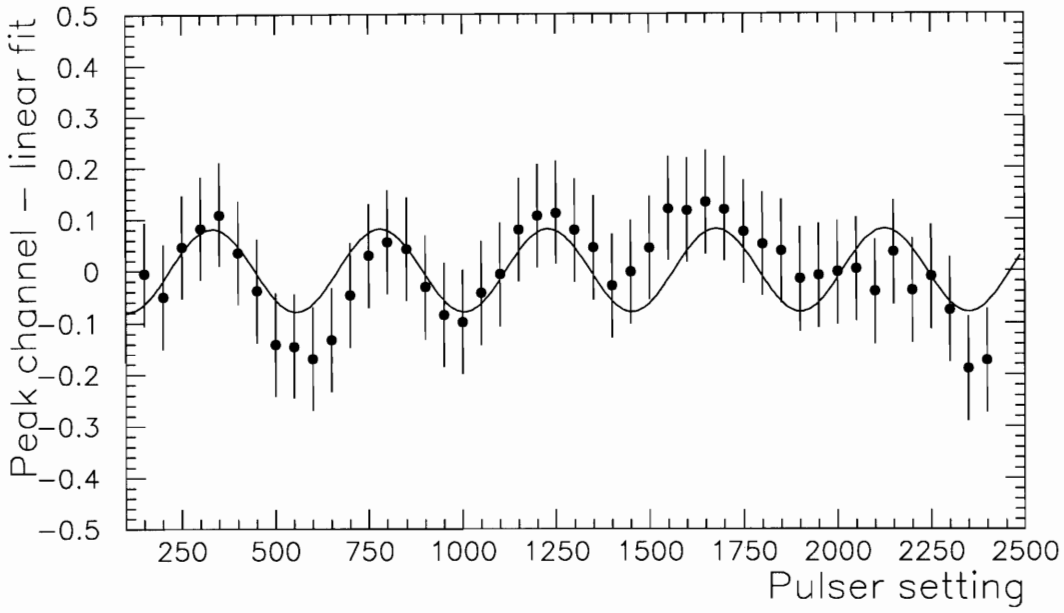

Figure 4.2: Deviation of ADC channel from linear fit as a function of pulser setting. The sinusoidal variation of the deviations indicates a calibration error in one of the ranges of the Decapot of the pulser.

shown in Fig. 4.2. The rms departure of the calibration from linearity was just 0.08 channels (or about 1 keV). (The sinusoidal structure seen in Fig. 4.2 is caused by a small calibration error in one of the ranges of the Decapot of the pulser.)

Calibration runs were performed approximately once per week. The calibration constants were stable to within 0.2% over a period of five months. Deviations of the alpha peak even by one channel were rare. When deviations did occur, the new calibration was used.

The excellent linearity and stability of the energy calibration allowed us to use

Eqs. 2.8 and 2.7

$$T = \frac{2m \sin^2 \alpha}{\kappa - \sin^2 \alpha} = \frac{t}{2m}$$

to determine the proton recoil angle α and the momentum transfer t from a measurement of the recoil energy. As it turns out, recoil angle determinations based on energy measurements were found to be more accurate and stable than the determinations based on survey measurements and the carriage position encoder, particularly because evidence was found for small backlash in the chain drive of the encoder.

4.2 Detector Solid Angle Calibration

In order to use different detectors to measure relative differential cross sections, we must know the relative effective areas of the different detectors. The nominal areas of the detectors were provided by the manufacturer. However, these values were not sufficiently accurate for our use. We therefore decided to make our own area measurements using radioactive alpha sources. We measured the absolute area of the fixed detector, and measured the areas of the movable detectors relative to that of the fixed detector.

The area of the fixed detector was measured using a ^{241}Am alpha particle standard purchased from the National Bureau of Standards (# 4904S-G). The source consists of ^{241}Am electroplated on a 0.016 cm thick platinum foil of 0.6 cm diameter. The platinum foil is glued to the center of a stainless steel disk 2.54 cm in diameter and 0.16 cm thick. The activity of the source was measured on May 16, 1986 at the National Bureau of Standards and found to be 2429(10) disintegrations per second. Correcting for the half-life of ^{241}Am (432.2 years), the activity when we made our area

measurements was 2400(10) dps (64.86(27) nCi). This source was mounted vertically above the fixed detector on an accurately machined post. This was done after the apparatus had been removed from the antiproton source. The alpha spectrum was accumulated so as to obtain $\sim 10^6$ counts in the peak (see Fig. 4.3).

The effective solid angle which the detector subtends at the alpha source was measured as

$$\Delta\Omega_\alpha = 4\pi n/N \ , \tag{4.1}$$

where n is the measured count rate, and N is the 4π count rate (absolute activity) of the source. The measured count rate was obtained by integrating the observed spectrum from 3 MeV to 6.2 MeV. The background is negligible in this region, and this region contains 99.8% of the counts in the total background subtracted spectrum (see Fig. 4.3).

The effective solid angle $\Delta\Omega_\alpha$ relative to the alpha source can also be calculated as

$$\Delta\Omega_\alpha = \frac{1}{A_{\text{source}}} \iiint \frac{z\, dx_0 dy_0 dx dy}{((x-x_0)^2 + (y-y_0)^2 + z^2)^{3/2}} \ , \tag{4.2}$$

where x and y range over the area of the detector, x_0 and y_0 range over the (much smaller) area of the source, z is the fixed height of the source above the detector centroid, and A_{source} is the area of the alpha source.

Equation 4.2 shows that the exact relation between the area of the detector and the solid angle $\Delta\Omega$ is rather complicated. In order to calculate the area from the measured solid angle, we used the fact that for the typical dimensions involved in our measurements the ratio $A/\Delta\Omega$ of the area to the solid angle is almost independent of the area. This was confirmed by a Monte Carlo calculation in which a known

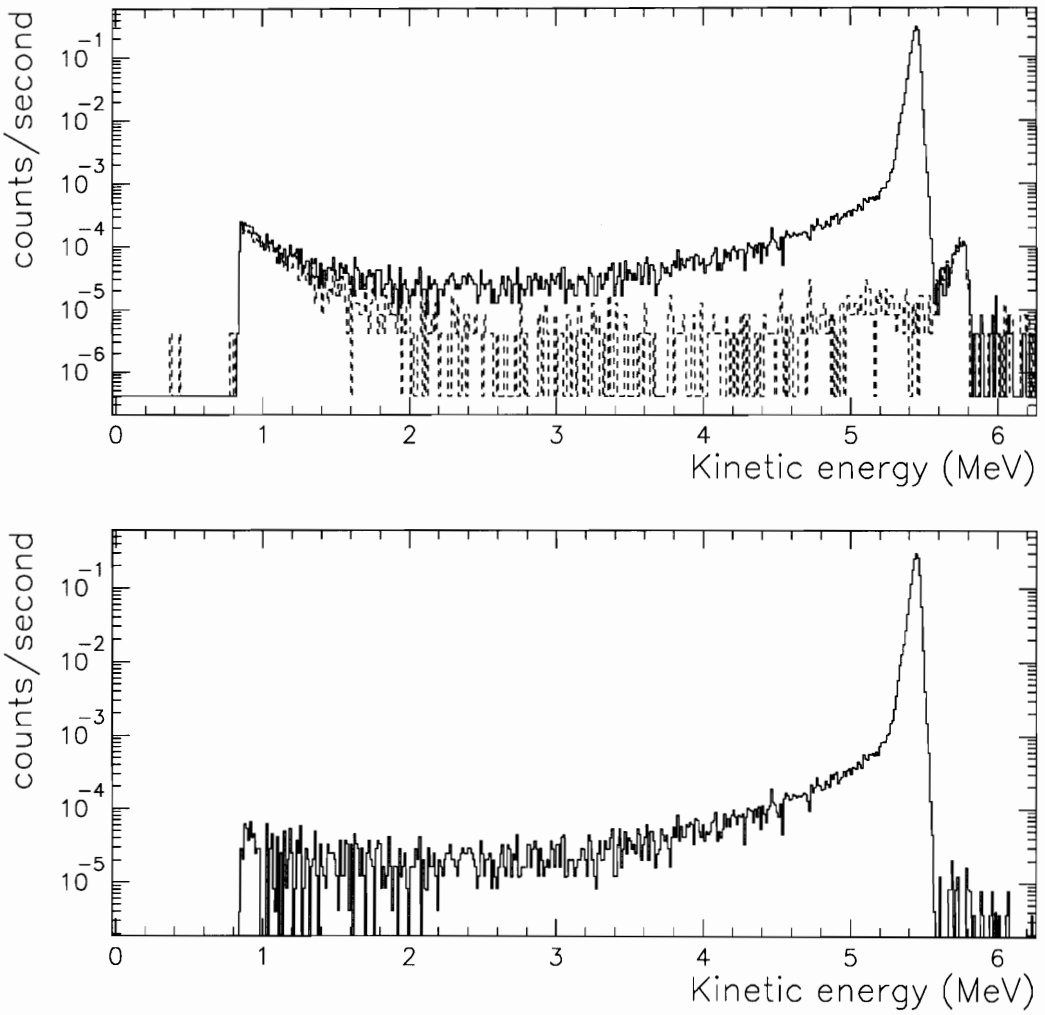

Figure 4.3: The upper panel shows the alpha particle spectrum from the ^{241}Am standard (solid) together with the background spectrum acquired with the source removed (dashed). The small peak at ~5.75 MeV is due to a small amount of ^{244}Cm contamination in the vacuum vessel. The lower panel shows the "no source" background subtracted spectrum. The residual background is more than four orders of magnitude smaller than the peak.

number of particles was generated uniformly over the area of the source and emission angles were assigned isotropically. The number of hits in the detector were then counted and the solid angle was calculated using Eq. 4.1. More than one million events were generated for each of several detector sizes close to the size given by the manufacturer. Calculations made for the source heights of 17.72 cm and 35.52 cm showed that $A_{MC}/\Delta\Omega_{MC}$ varied by $\leq 0.1\%$ for the different detector sizes at each height.

With $A_{MC}/\Delta\Omega_{MC}$ determined as described above, the effective area A of the detector was calculated from the measured solid angle (Eq. 4.1) as

$$A = \Delta\Omega_{\alpha}(A_{MC}/\Delta\Omega_{MC}) \; . \tag{4.3}$$

Several measurements were made with the source mounted at each of two different heights, z=17.72(2) cm and 35.52(2) cm. The results of these measurements are shown in Table 4.1. The table shows that the effective area of the fixed detector was found to agree for the two measurements within 0.2%, with the mean value being $A_0 = 545.0 \pm 0.6 \pm 2.3$ mm^2, where the first error is statistical and the second is systematic. The systematic error is due to uncertainties in the source activity and the distance of the source to the detector. Our measured value of the area is thus 6.0% less than the nominal area quoted by the detector manufacturer.

The ratios of the areas of the detectors on the carriage to that of the fixed detector were measured frequently *in situ* using the ^{244}Cm source between antiproton stacks when no data was being taken. The source was located $\sim$ 101 cm above the detectors, and the area ratio was approximated by

$$\frac{A_i}{A_0} = \frac{n_i r_i^2 \cos\alpha_0}{n_0 r_0^2 \cos\alpha_i} \; , \tag{4.4}$$

Table 4.1: Solid angle measurements and area calculations. When two uncertainties are given, the first is statistical and the second is systematic.

Run #	Counts/sec	$\Delta\Omega_\alpha = 4\pi n/2400$	Area(mm^2)
		Height = 17.72(2) cm	
1552	3.270(34)	.01711(18)	542.2(57)
1553	3.291(35)	.01722(18)	545.7(57)
1554	3.281(11)	.01717(6)	544.1(19)
1555	3.262(16)	.01707(8)	540.9(25)
1556	3.285(3)	.01719(2)	544.7(6)
		Average =	$544.4 \pm 0.5 \pm 2.6$
		Height = 35.52(2) cm	
1564	0.8272(32)	.004329(17)	546.9(21)
1565	0.8253(22)	.004319(12)	545.7(15)
1566	0.8235(32)	.004310(17)	544.5(21)
1578	0.8235(32)	.004304(17)	543.8(21)
		Average =	$545.3 \pm 0.9 \pm 2.3$
		Overall average =	$544.7 \pm 0.5 \pm 2.6$

where n, r, and $\cos\alpha$ refer to the count rate, distance from the source, and angle from the vertical, respectively, for detector i on the carriage (subscript 0 denotes the fixed detector). The above relation is accurate to better than 0.07% for our geometry.

The area ratios calculated repeatedly during the running period are shown in Fig. 4.4. The figure shows that the measured areas were extremely stable over the course of the run. The figure shows that the rms/$\sqrt{N}$ is about 0.1% for all but detector # 3, which suffered from radiation damage for the second half of the run. The dashed histogram shows the area measurements for detector # 3 taken in the first half of the run. During this time, the rms/$\sqrt{N}$ was also about 0.1%; the detector was not used thereafter.

It was known that the lithium drift detectors have smaller areas than the ion-implanted detectors. It was observed that the alpha spectra in these detectors also had longer tails, so that the integrated number of counts depended on the lower integration limit. A lower limit of 3 MeV (the same as for the ion-implanted detectors) was used, and a ratio of $A_5/A_0 = 0.9356(11)$ was obtained. This ratio was also determined independently by allowing it to vary as a free parameter in the fit to the differential cross section data (see Sec. 6.5). The best fit value for the area ratio was found to be 0.9357(5), which is in perfect agreement with the value given above.

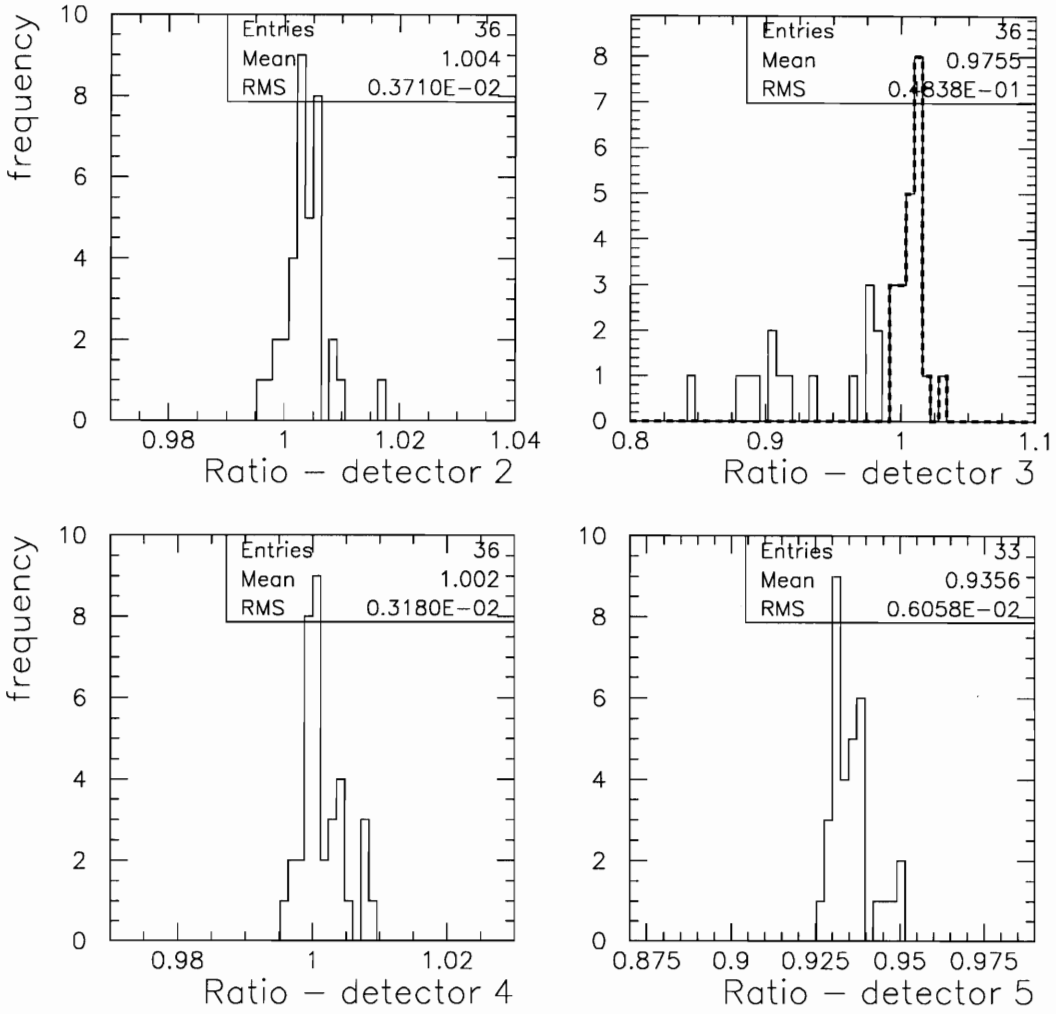

Figure 4.4: Ratios of the areas of the carriage detectors to that of the fixed detector. The dashed histogram for detector # 3 indicates values of the ratio during the first three months of the running period, during which data from this detector were used, and the detector was operating satisfactorily. The mean value of the area ratio for this period was 1.008. Detector # 5 is the Li-drift detector of smaller area.

Chapter 5

Monte Carlo Calculations

In order to better understand the performance of the detectors and the effects of beam displacement, a Monte Carlo program was written to simulate the observed recoil energy spectrum. The simulation enabled us to determine the density distribution of the hydrogen target, and was also used to calculate the variation of the geometric acceptance of the detectors as a function of the horizontal displacement of the antiproton beam relative to the center of the beam pipe.

5.1 Interaction Region Density Distribution

In order to understand the performance of the detectors in a detailed and quantitative manner, it is necessary to know the density distribution of the interaction region. Recall that the beam travels in the z direction, the gas jet travels in the x direction, and y is the vertical. The density distribution of the interaction region is determined by the antiproton beam density profile (in the $x-y$ plane) and the gas jet density profile (in the $y-z$ plane). The gas jet has cylindrical symmetry by construction. The beam profile was determined by the measured beam emittances and the known beta function of the accumulator. The emittances were 1.5 ± 0.5 π mm-mrad, and beta

was 7.4 ± 1.9 m in the horizontal direction and 5.9 ± 1.5 m in the vertical direction [15]. This gave 95% beam containment in an elliptical profile with the x dimension (major axis) being 5.4 ± 2.2 mm and the y dimension (minor axis) being 4.8 ± 2.0 mm. Thus, the profile density of the beam can be well approximated by a Gaussian with $\sigma = 1.3 \pm 0.5$ mm in both the x and y directions. Note that the entire beam is contained within the diameter of the gas jet (see below).

Given the beam density profile, the recoil spectrum for the fixed detector was generated by assuming a density profile for the gas jet. For a trial profile of the gas jet, the x, y and z coordinates of collisions between the beam and gas jet were generated by a Monte Carlo program. Recoil events were created at the collision points according to the known $\bar{p}p$ elastic cross sections. The energy spectrum of those recoil events which were incident on the active area of the fixed detector was accumulated. The spectrum was corrected for energy loss in the dead layer of the detector ($\leq$ 20 keV), and for the energy resolution of the detector and the electronics chain (see Table 3.2), as determined from the ^{244}Cm alpha particle spectra. The Monte Carlo spectrum thus produced was then compared to the experimental background subtracted spectrum.

A uniform gas jet density distribution with circular cross section was assumed at the intersection region and the value of its diameter was iterated. Figure 5.1 shows the distribution obtained for a uniform density gas jet of diameter 6.70 mm. The sensitivity of this method is sufficient to determine the best fit gas jet diameter to be 6.70 ± 0.05 mm. The fit to the data, shown more sensitively on the plot of the ratio of the Monte Carlo predictions to the data, is excellent. No improvements in the fit were obtained by introducing smoother fall-offs of the density at the edges. The best fit result was also found to be stable within the stated errors even when the

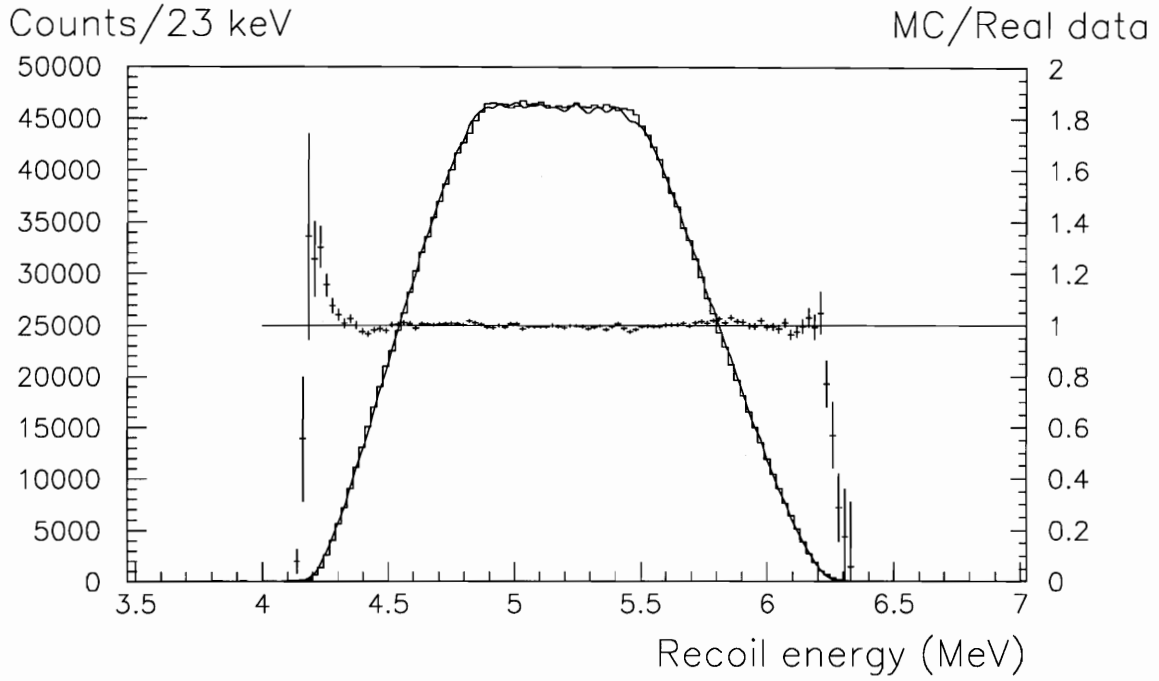

Figure 5.1: Monte Carlo recoil energy spectrum, using a uniform circular gas jet distribution of radius 3.35 mm. The histogram in the center shows real data with the Monte Carlo predictions overlaid as a smooth curve. The set of points with error bars shows the ratio of the Monte Carlo predictions to the real data and corresponds to the scale on the right side of the plot.

beam diameter was changed by ±50%. As a test of how universally valid the density profile determination is, the same density was used to generate Monte Carlo spectra for detectors at other recoil angles. As shown in Fig. 5.2, in all cases the Monte Carlo results were found to be in excellent agreement with the data. We therefore feel confident that the gas jet density profile is uniform with a diameter of 6.70 ± 0.05 mm, which is equivalent to a 95% confinement width of 6.4 mm.

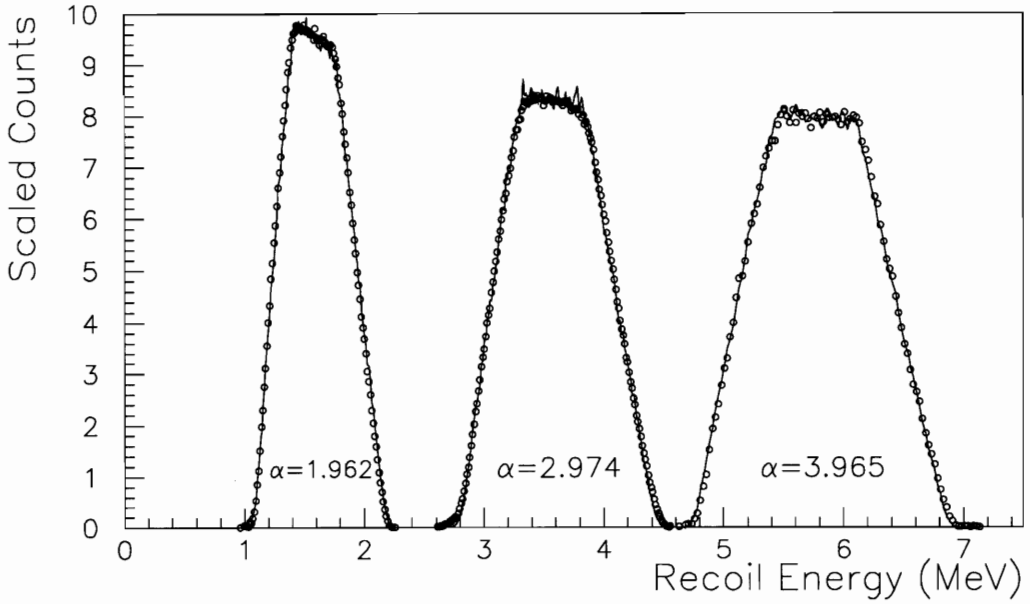

Figure 5.2: Monte Carlo generated spectra compared with real data at three different recoil angles. The open circles represent the real data and the smooth curves are the Monte Carlo predictions. The shape of these spectra illustrates the t acceptance of the detector system.

5.2 Corrections for Beam Displacements

As described in Sec. 3.4, the detectors 'see' the interaction region through a 12 mm diameter coupling aperture. It is important to find out the extent to which this finite aperture prevents the detectors from 'seeing' the entire beam-jet interaction region when the beam is in its central orbit, i.e., in the center of the beam pipe, and how this loss varies as a function of the horizontal (x) displacement of the beam and the position of the detectors.

Analysis of the data from the beam position monitors (BPMs) located throughout the Antiproton Accumulator ring showed that the horizontal position of the beam varied by as much as 4 mm from stack to stack. This is significant relative to the 12 mm aperture coupling the detectors to the interaction region. The absolute calibration of the BPMs was poorly known, however, and it was not possible to precisely determine the effect on the detector acceptance based solely on the BPM measurement of the beam position. We therefore developed a procedure in which the horizontal beam position could be determined from the observed count rates in the solid state detectors. The count rates were then corrected if the beam was found to be displaced. This procedure is described below.

The first step was to use the Monte Carlo program described in the previous section to model the effect of beam displacements on the observed count rates. The Monte Carlo program was used to calculate the ratio of the number of protons which would reach a detector through the aperture to the number of those which would reach the detector in the absence of the aperture. This fraction, of course, depends on both the x-positions of the beam and the detector, and to a lessor extent the recoil

angle of the detector. It was found that because of the large vertical distance from the detectors to the interaction point (150 cm), the vertical displacements of the beam (a few mm) have no effect on the observed count rates.

The fraction of events not seen by the movable detectors due to the presence of the 12 mm coupling aperture is shown in the lower panel of Fig. 5.3 as a function of α and the horizontal beam position. The figure shows that the effect is worse for smaller recoil angles. For beam displacements of 2 mm or less, which accounted for the vast majority of the data, the effect is $\leq 1.5\%$ even at the smallest recoil angles.

The fixed detector is located at a different x-position than the movable carriage and therefore is affected differently by a beam displacement. The fraction of events not seen by the fixed detector is shown in the upper panel of Fig. 5.3 as a function of beam displacement. Similar to the movable detectors, the fixed detector experiences losses of just a few percent when the beam is displaced by 2 mm or less.

The fact that the fixed detector and movable carriage are on opposite sides of the beam provides a diagnostic tool for determining the x-position of the beam. If the beam is in the center of the beam pipe, then a detector on the movable carriage at $\alpha = 3.547°$, i.e., at the same recoil angle as the fixed detector, sees the same count rate as the fixed detector[1] (after accounting for the different detector areas). When the beam is displaced in x, the two detectors are affected differently. The ratio of counts in the two detectors therefore indicates the horizontal displacement of the beam. This is illustrated in Fig. 5.4 from Monte Carlo calculations. We notice that for a beam displacement of $-2(+2)$ mm the ratio differs from unity by $\sim +3\%(-1\%)$.

[1]The movable detectors were actually placed only at integer multiples of 0.125°. The count rate at 3.547° was obtained by interpolation.

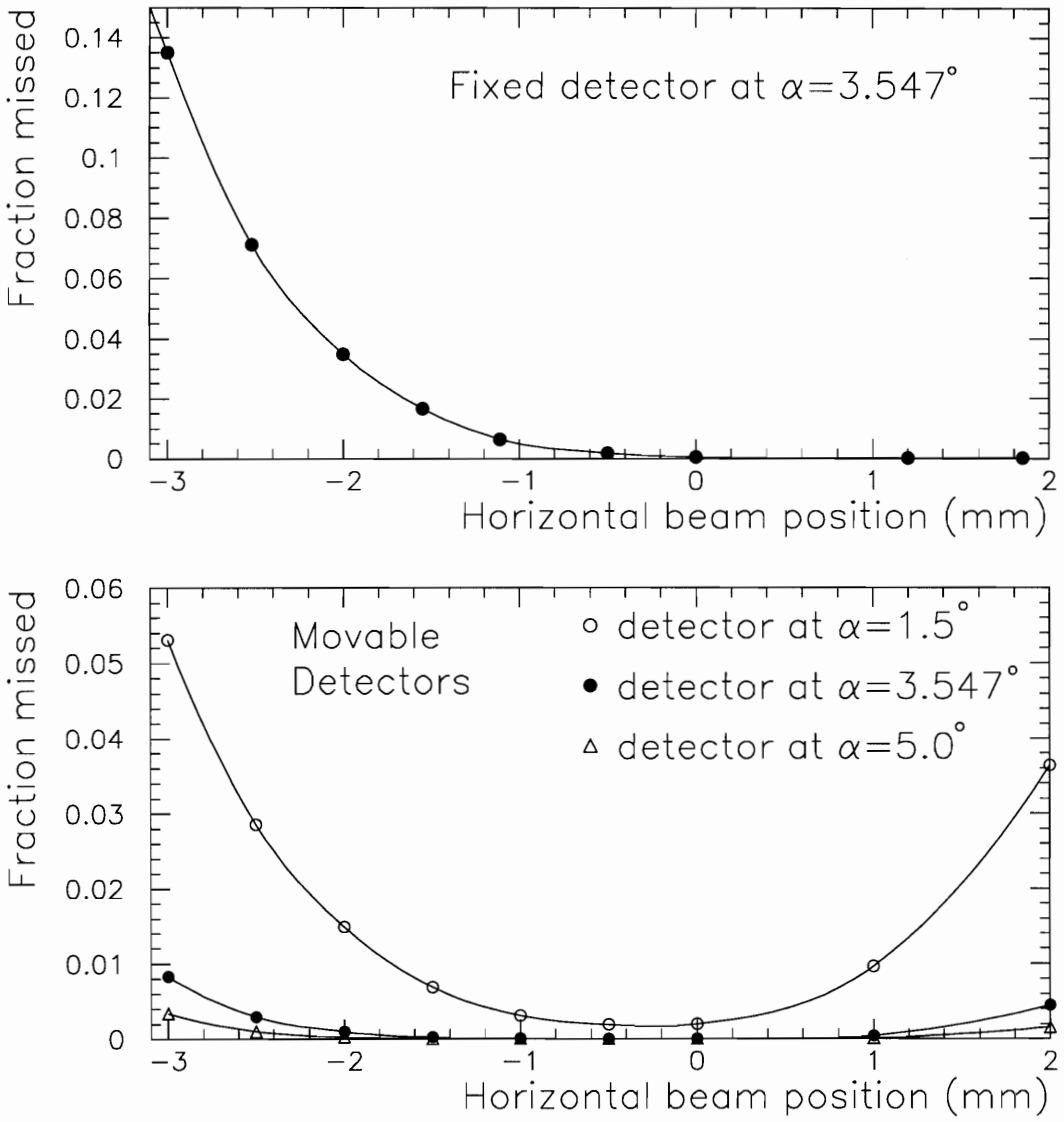

Figure 5.3: Fraction of events (calculated via Monte Carlo) not seen by the fixed detector at $\alpha = 3.547°$ and by a detector on the carriage as the result of horizontal beam displacements.

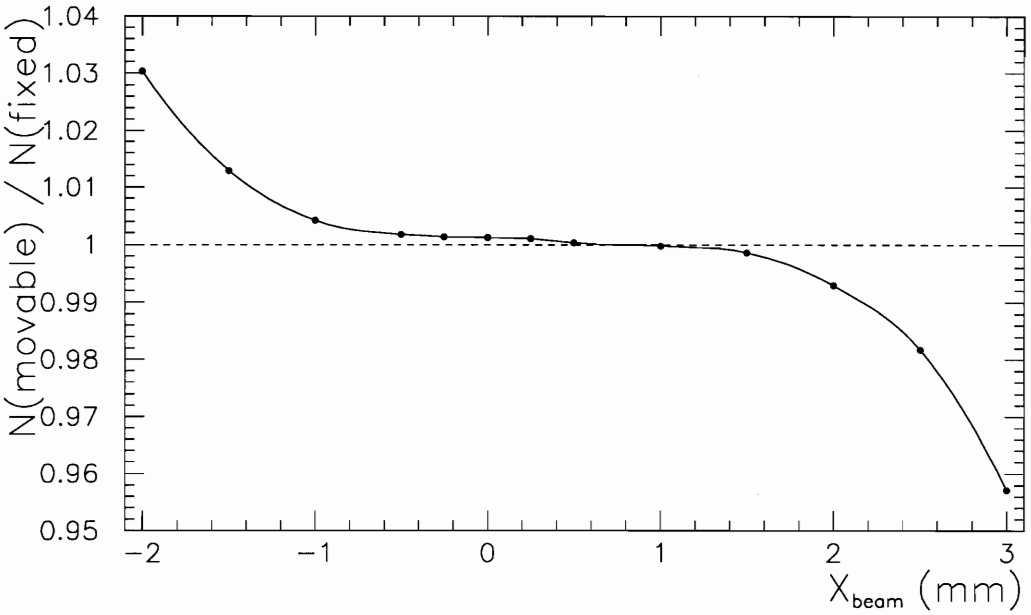

Figure 5.4: Ratio of counts in a movable detector at $\alpha = 3.547°$ to the counts in the fixed detector at the same angle as a function of the horizontal beam position.

The procedure for correcting for beam offset was to measure the ratio of counts in the fixed and movable detectors and then use the relation shown in Fig. 5.4 to calculate the beam displacement. The beam displacements determined in this way for each stack are shown in the top panel of Fig. 5.5. There were two other methods at our disposal for determining horizontal beam displacements. One was the data from the BPMs. Unfortunately, as mentioned earlier, the absolute calibration of the BPMs was unreliable, and it was only possible to use them to measure relative displacements. These data are shown for each run in the center panel of Fig. 5.5.

Another method is provided by the use of the E760 detector system (see Sec. 3.3) to reconstruct the $\bar{p}p$ interaction point via the analysis of $\bar{p}p \rightarrow \pi^0\pi^0$ events. The interaction vertex for each run is determined by an iterative procedure. An arbitrary interaction point is first chosen. From the measured centroids of the four clusters in the calorimeter (two photons for each π^0), the momentum vectors are constructed for the two π^0's. If the interaction region were truly a point, then for the correct choice of the vertex, these vectors should be back to back, and if their end points at the detector were joined, the straight line should pass through the vertex, i.e., the perpendicular distance between this line and the vertex should be zero. Since the trial interaction point may not be correct, and since the interactions occur over a finite region, the distances for different events are non-zero. One finds a second trial position of the vertex by minimizing the sum of these perpendicular distances. This second trial position is then used to recalculate the π° momentum vectors, and the whole process is repeated. This iterative procedure is continued until the input and output vertices agree within 0.1 mm. The results of this analysis are shown in the lower panel of Fig. 5.5.

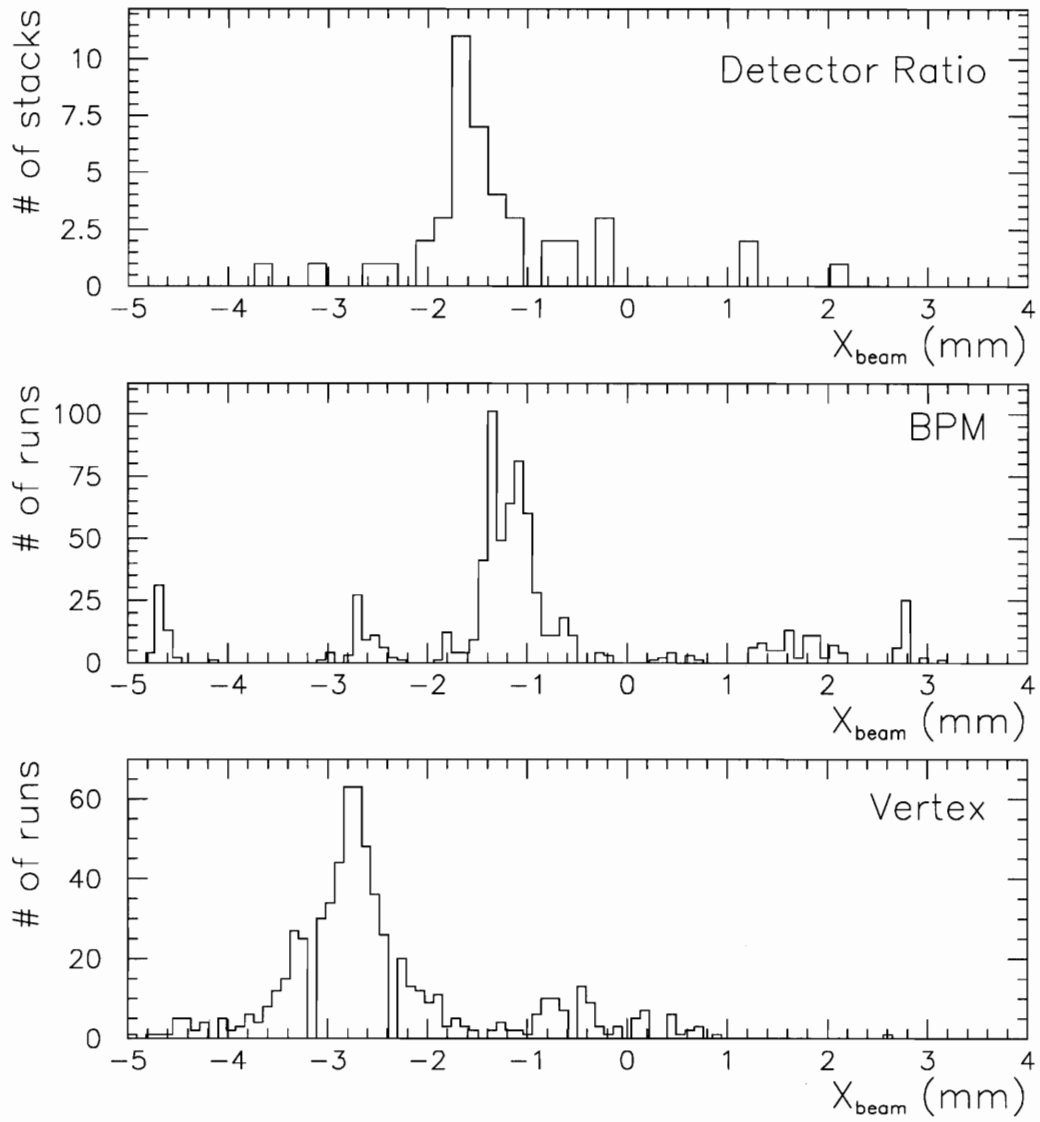

Figure 5.5: Distributions of measured horizontal beam displacements by three different methods.

The three panels in Fig. 5.5 all show some variation in the position of the beam. Note that each entry on the top panel represents data from an entire stack, while in the other two panels there is an entry corresponding to each run in a stack. The top panel shows that for most of the stacks the beam was displaced by about -1.6 mm. There were two stacks that were displaced by more than -3 mm and three that were displaced by more than $+1$ mm. Although the values of the displacements are different in the center panel (due to the lack of absolute calibration of the BPMs) the relative shifts agree with the determination shown in the top panel. There are still two stacks with large negative displacements, three with large positive displacements, and the majority of data clustered around -1 mm. The results of the $2\pi^0$ vertex analysis (shown in the bottom panel) are smeared out by the effects of the calorimeter resolution and the finite size of the beam and the gas jet. They are also offset by ~ -1.5 mm with respect to those of the detector ratio method. This is most likely due to errors in the surveyed position of the calorimeter with respect to the interaction point. Nevertheless, it is seen that most of the data from the vertex analysis are also closely clustered and that a small number of runs are displaced by large amounts.

Note that it was the detector ratio method which was actually used to calculate the beam displacement. This method is the most precise and is the only one capable of providing absolute measurements of the beam displacement. Stacks for which the beam displacements (as measured using the detector ratio method) were larger than ± 2.5 mm were not used in the elastic scattering analysis. Once the beam displacements are known, all the observed count rates can be corrected for them. As shown in Fig. 5.3, the corrections for the fixed and movable detectors partially cancel each other since the counts observed in the movable detectors are always normalized

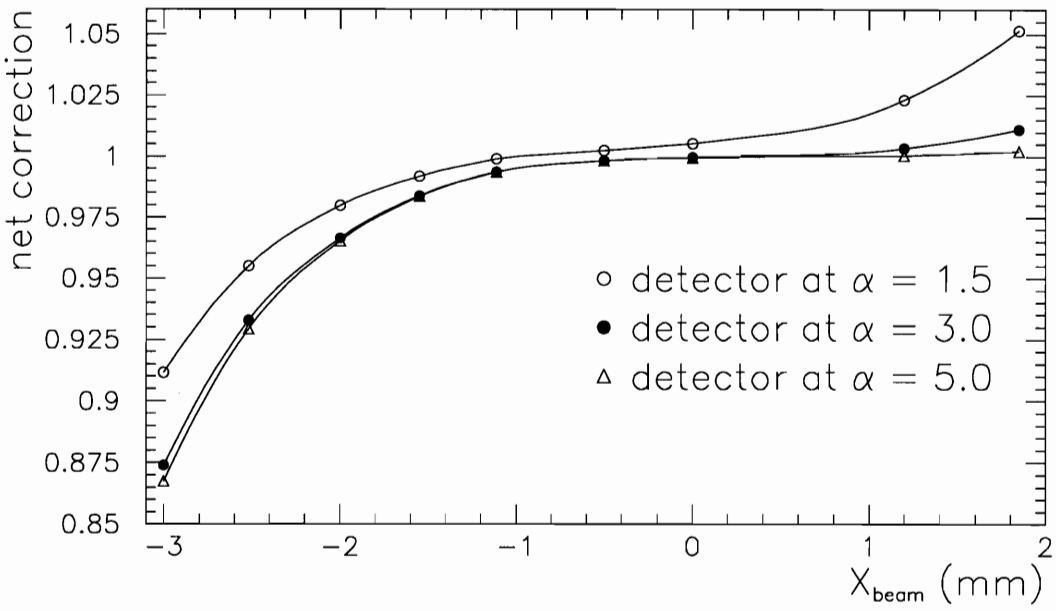

Figure 5.6: Net correction factors to be applied to the counts in the movable detectors normalized to the fixed detector.

to those in the fixed detector. The net correction factors are shown in Fig. 5.6 as a function of beam displacement and recoil angle. For the vast majority of the data, which had beam displacements between -1 mm and -2 mm, the corrections were less than 3.5%.

Chapter 6

Experimental Method and Data Analysis

The procedure for the accumulation and cooling of an antiproton stack in the Antiproton Accumulator has been described in Sec. 3.1. A typical stack contained 4×10^{11} antiprotons and required about 30 hours to accumulate. When the stack reached the desired intensity, the antiprotons were decelerated from the injection energy of 8.9 GeV to the energy of interest for data-taking. During these periods of antiproton accumulation and deceleration, the H_2 gas jet was shut off, and detector calibration data were collected using the ^{244}Cm alpha source (see Secs. 4.1 and 4.2).

6.1 Data Acquisition

Once the antiproton stack was decelerated to the proper energy, the gas jet was switched on and data-taking was begun. The data for the measurement of the differential cross section were taken according to the following procedure. The detector carriage was initially positioned at the largest possible recoil angle. In this position detector 2 was at $\alpha \approx 2°$, detector 3 at $\alpha \approx 3°$, etc. Data were taken in this position until roughly 100,000 counts were accumulated in the spectrum of each detector. At this point, data acquisition was stopped, and the energy spectrum of each de-

tector was written to disk. The carriage was then moved by approximately 3.2 mm ($\Delta\alpha \approx \frac{1}{8}^\circ$), and another set of spectra was acquired. This cycle of data taking at $\frac{1}{8}^\circ$ steps was continued until the carriage had moved a full degree in recoil angle from its original position. In this ninth and final step, detector 2 was at $\alpha \approx 1^\circ$, detector 3 at $\alpha \approx 2^\circ$, etc. That is, data were taken at the same recoil angles as in the first step, but with different detectors. This 'overlap point' provided a check on the relative detector area calculations described in Sec. 4.2. After data were taken at the overlap point, if a sufficient number of antiprotons remained in the beam to continue charmonium data taking, the carriage was returned to its original position, and another set of measurements was made in order to increase the statistical precision at each angle.

The lifetime of the antiproton stack was 50 to 90 hours, depending on the beam energy. A stack was typically used for one lifetime, after which the beam was dumped and the acquisition of a new stack was begun. There was usually time for two to three complete sets, each of nine detector carriage positions, before the antiproton stack was dumped.

The fact that data at up to three complete sets of detector carriage positions were possible per stack meant that there were up to three energy spectra for each detector at each of the nine detector positions. Data taken with the same detector at the same position were summed resulting in a set of 45 spectra - one for each of the five detectors (four detectors on the carriage plus the fixed detector) at each of the nine carriage positions.

During the running period from June of 1991 through January of 1992 differential cross section data were taken in 20 stacks at six different beam energies. Data sets taken at the same energy were fitted simultaneously to yield a single set of scattering

parameters.

6.2 Background Subtraction

The proton energy spectrum recorded by each detector consists of a prominent elastic peak sitting on a background which is generally a factor 20 to 40 smaller. The first step in the analysis is to extract the elastic signal from the observed spectrum. The differential cross section can then be determined from the number of background-subtracted counts.

Prior to the main data runs with antiprotons, a few measurements were made using a test beam of protons to try to anticipate the nature of the background to be expected in $\bar{p}p$ collisions. Four of the recoil spectra from these pp runs are illustrated in Fig. 6.1 for a detector at 0.5°. At this angle the elastic recoil protons have energies below the smallest energy shown in the figure. As histogram #1 of Fig. 6.1 illustrates, the background with both the gas jet and proton beam on has two distinct components. In the low energy region ($T < 1$ MeV) the background rises rapidly with decreasing energy. In the energy region $T > 1.5$ MeV the background varies more slowly. A comparison of histograms 1 and 2 shows that the slowly varying part of the background ($T > 1.5$ MeV) disappears when the gas jet is turned off. This component is therefore due to particles produced in pp collisions. We also note that this component of the background falls to zero at a recoil energy of about 8 MeV (see the lower panel in Fig. 6.2). This indicates that it can not be due to electrons or any other minimum ionizing particle, because in that case the maximum energy loss in 500 μm of silicon is only ~0.5 MeV. The maximum energy loss for a proton in 500 μm of silicon is, however, 8.1 MeV. We therefore conclude that the main part of the

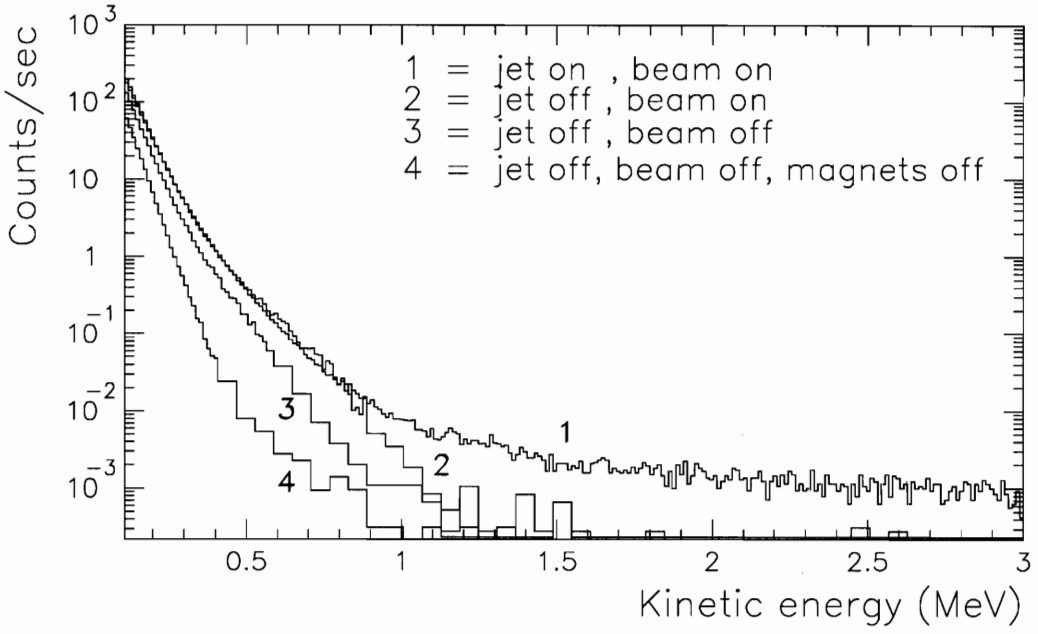

Figure 6.1: Energy spectra for pp collisions under various beam/gas jet conditions for a detector at $\alpha = 0.5°$.

high energy background is due to protons. Such protons can arise in several ways. The most likely process is $pp \rightarrow pp + N\pi$.

In contrast to the high energy background component, the rapidly varying low energy component of the background (histograms 2, 3, and 4 of Fig. 6.1) persists even after the gas jet is turned off. Further, when the antiproton beam is turned off, the background level decreases by approximately a factor of two. A similar decrease is again observed when the magnets in the Antiproton Accumulator ring are also turned off. These observed variations do not lead to any simple conclusions, except that the background shown in histograms 3 and 4 most likely have their origin in detector and electronic noise and rf pickup.

Figure 6.2 shows the energy spectra of two detectors on the movable carriage for a typical $\bar{p}p$ run. In both cases the elastic peak is clearly visible above the background. We note that the nature of the background in $\bar{p}p$ collisions is very similar to that for the pp case discussed above. Once again the background has two distinct components and we surmise that their origin is also as described above. We note that the high energy ($T > 1.5$ MeV) component is now due to $\bar{p}p \rightarrow \bar{p}p + N\pi$ reactions which are known to have quite substantial total cross sections, e.g., 19 mb at 3.6 GeV/c [155]. Since it was not possible to eliminate the background, it was decided to carefully study the variation of the background with incident antiproton momenta and recoil angles, and to subtract the background from the recoil energy spectra in an empirically determined consistent manner.

The background in each spectrum was determined by a completely empirical fit to that portion of the spectrum which does not include the elastic peak. It was possible to do so reliably because, as shown in Fig. 6.2, the background level was typically

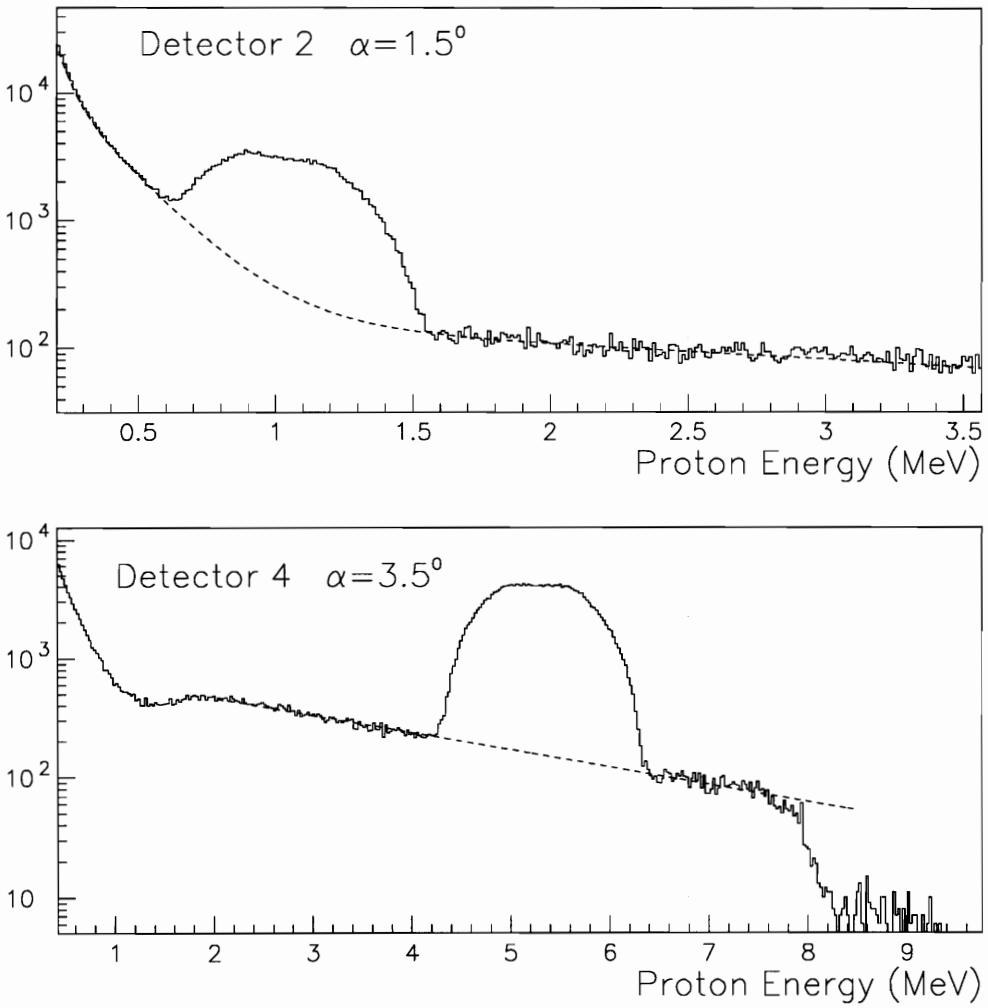

Figure 6.2: Typical energy spectra for two detectors on the carriage. The dashed lines represent the background fits which are described in the text.

only 5 to 10% of the elastic peak. In choosing the functional form of the background fit, the number of parameters was kept at the minimum required to obtain good agreement with the data ($\chi^2/df \approx 1.0$).

For $|t| > 0.003$ (GeV/c)^2 ($\alpha > 2°$), proton recoil energy is larger than $\sim$ 1.5 MeV. In these cases the recoil peak sits on top of a smooth and stable background which varies exponentially and which is nearly a factor 40 smaller than the peak. An example of such a spectrum is shown in the lower panel of Fig. 6.2. As shown, this background can be subtracted very reliably by means of a simple exponential parametrization.

For $|t| < 0.003$ (GeV/c)^2 ($\alpha < 2°$) the recoil proton energy is less than 1.5 MeV, and the recoil peak sits on the part of the background which increases rapidly as the energy decreases. An example is shown in the upper panel of Fig. 6.2. Although the origin of this background is not well understood, it is very stable. This fact, illustrated in Fig. 6.3, allows the background to be determined accurately by comparing the recoil spectrum at one detector angle with that at an adjoining angle. As the recoil peak moves away with the change of angle, it reveals the almost exact form of the background under its former position.

The uncertainty in the background-subtracted counts arises from the uncertainty in the determination of the level of the fitted background curve. This uncertainty was estimated by comparing the background subtracted counts in several spectra taken under identical conditions, i.e., with the same detector, at the same recoil angle, and at the same beam energy. The rms variation in the background subtracted counts normalized to the corresponding counts in the fixed detector are given in Table 6.1. It was found that these errors were characteristic of each detector. Note that for detector

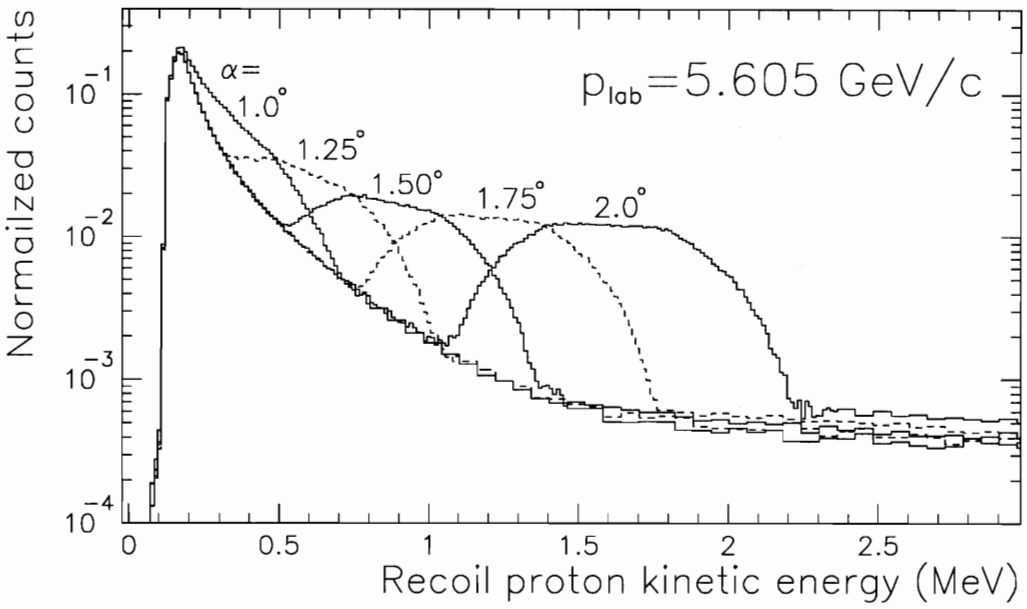

Figure 6.3: Recoil spectra for detector # 2 at five angles between 1° and 2°. The spectra are normalized to the counts in the fixed detector.

Table 6.1: Uncertainties due to background subtraction

Detector:	2 ($\alpha < 1.3°$)	2 ($\alpha > 1.3°$)	3	4	5
error (%):	1.47	0.52	0.97	0.43	0.67

#2, the values are given for two angular ranges. The larger error at very small recoil angles indicates the greater uncertainty in performing background subtraction in the region of rapidly rising background.

6.3 Determination of Recoil Energy Centroid

The background-subtracted spectrum is also used to determine the mean recoil angle of the detector. Two body kinematics (see Sec. 2.1) relates the recoil proton energy to the recoil angle and momentum transfer

$$T = \frac{2m \sin^2 \alpha}{\kappa - \sin^2 \alpha} = |t|/(2m) \ , \tag{6.1}$$

where $\kappa = (E_{\text{beam}} + m)/(E_{\text{beam}} - m)$. An algorithm was therefore developed to determine the central energy of the recoil protons, or equivalently the central value of t. The central energy was determined by fitting the plateau region of the background subtracted spectrum to a straight line, and simultaneously fitting each sloping side to a Gaussian. By comparing with Monte Carlo simulations, the channel corresponding to the central value of t was empirically defined to be 1.0 ± 0.5 channels above the midpoint of the central plateau region as determined by the fit. Figure 6.4 shows typical fits for each detector on the carriage. As the figure illustrates, this method enables the determination of the centroid ADC channel to within half a channel. The channel number is converted to energy using the energy calibration described in Sec. 4.1. The use of Eq. 6.1 then leads to the determination of the central value $\bar{t}$ of the

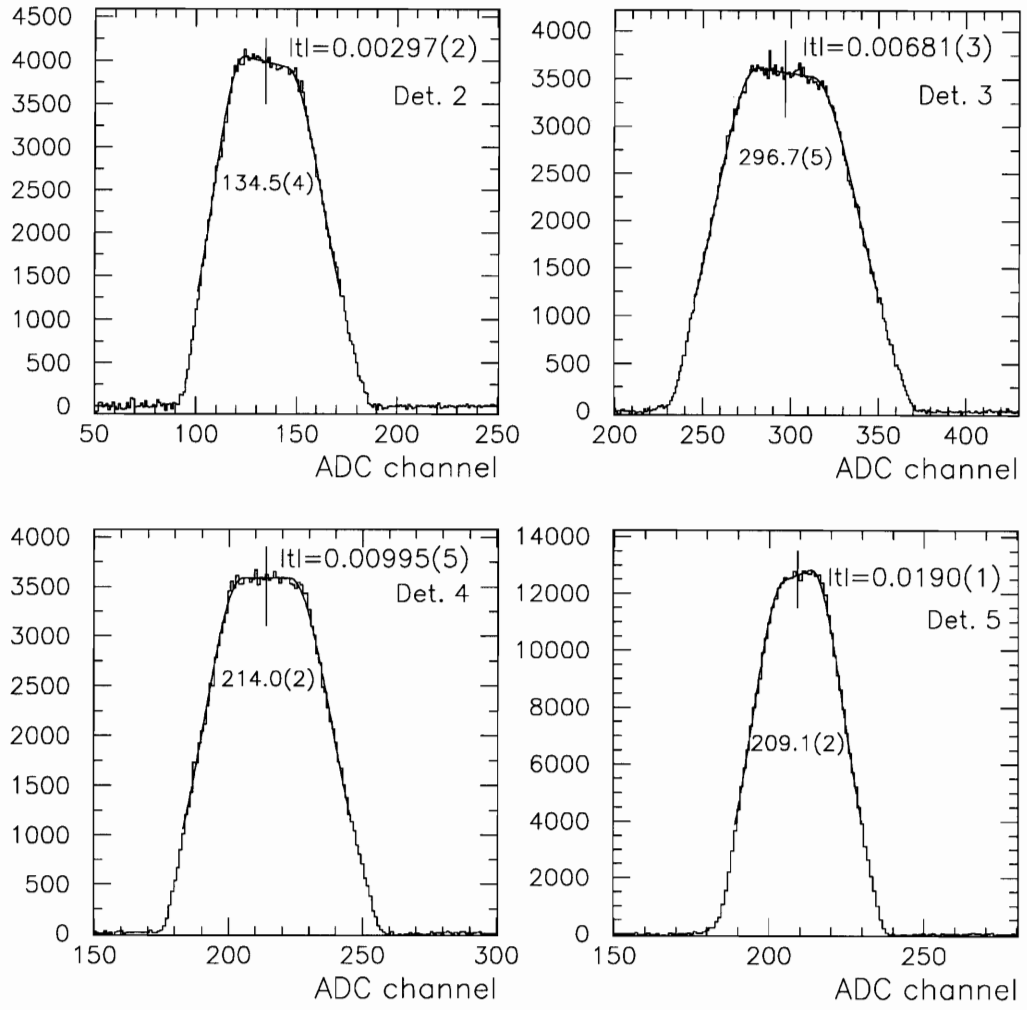

Figure 6.4: Background-subtracted spectra for each movable detector. The central channel and the t value corresponding to it as determined by the fit are shown.

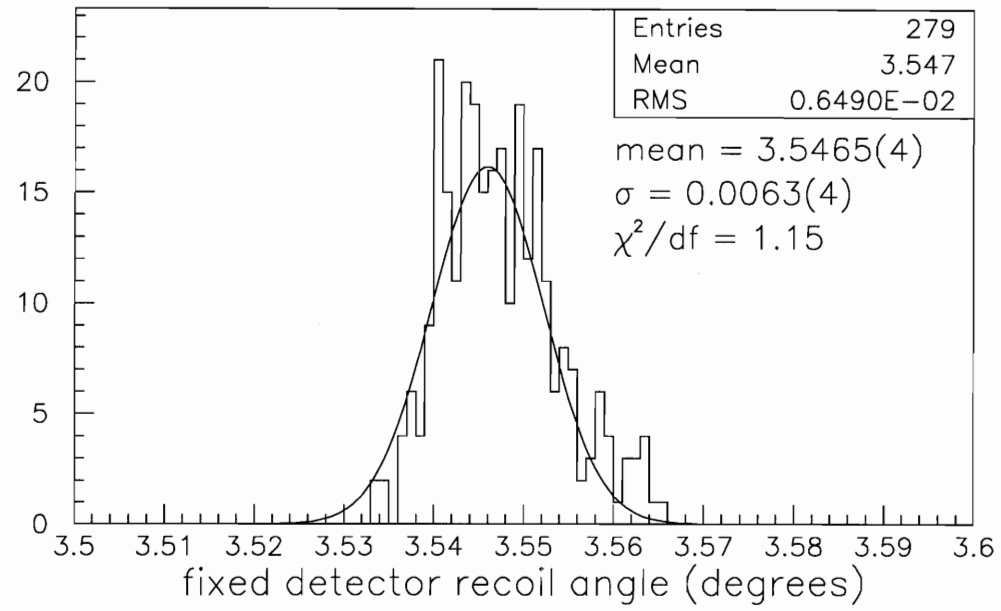

Figure 6.5: Frequency distribution of the measured recoil angle of the fixed detector. The curve is a fit to a Gaussian, and the fitted parameters are shown on the plot.

momentum transfer and the recoil angle $\alpha(\bar{t})$ corresponding to it.

Since the fixed detector is always at the same angle $\alpha = 3.5465(4)°$, the uncertainty in this method of determining the central value of t can be determined from the distribution of recoil angles $\alpha(\bar{t})$ calculated from a large number of fixed detector spectra. The distribution is shown in Fig. 6.5. The measurements lead to an estimate of the uncertainty inherent in the method of $\sigma = 0.006°$. This method was used for $\alpha \geq 1.8°$.

When detector 1 was at $\alpha < 1.8°$, the above algorithm did not lead to a good determination of recoil angles. Therefore a different procedure had to be adopted.

By determining $\bar{t}$ by the first algorithm for detectors 1 and 2 when they were at $1.8° - 2.0°$ and $2.8° - 3.0°$ respectively, it was determined that the separation between the geometrical centroids of the two detectors was $1.020(1)°$.

When detector 1 was moved to $\alpha < 1.8°$, $\bar{t}$ corresponding to it was calculated as that corresponding to the detectors geometrical centroid being at the recoil angle for detector 2 minus $1.020°$. This procedure yielded α in the $1°$ to $1.8°$ region also with estimated errors of about $\pm 0.006°$.

6.4 Determination of Relative $d\sigma/d\Omega$ from the Data

In the preceding two sections the methods for obtaining the number of background-subtracted counts and the central value of the momentum transfer in the recoil energy spectra have been described. These data, along with the effective area of each detector, are used to determine the differential cross sections.

The measured differential cross section is related to the number N of observed elastic events for integrated luminsoty L as

$$\frac{d\sigma}{d\Omega} = \frac{N}{L\Delta\Omega} \,. \tag{6.2}$$

$\Delta\Omega$, the solid angle subtended by the detector, is given by

$$\Delta\Omega = \frac{A\cos\alpha}{r^2} \,, \tag{6.3}$$

where r is the distance from the interaction point to the center of the detector. This relation is accurate to within 0.07% for our geometry. As shown in Fig. 6.6,

$$r = R/\cos\alpha \,, \tag{6.4}$$

where $R = \sqrt{x^2 + y^2}$. Expressing $\Delta\Omega$ in terms of R,

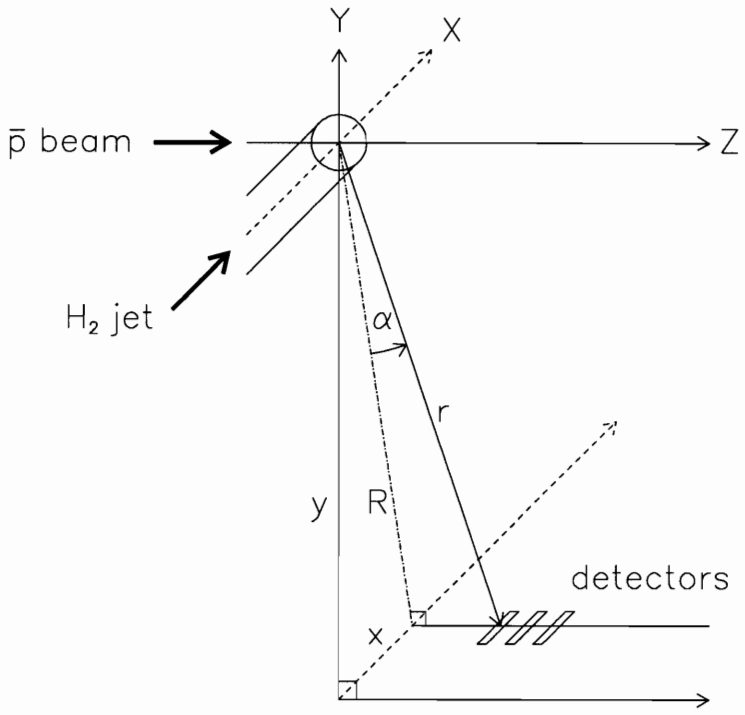

Figure 6.6: Schematic representation of the geometry of the measurements.

$$\Delta\Omega = \frac{A\cos^3\alpha}{R^2} \,. \tag{6.5}$$

Substituting this into Eq. 6.2 leads to

$$\frac{d\sigma(\alpha)}{d\Omega} = \frac{NR^2}{LA\cos^3\alpha} \,. \tag{6.6}$$

In order to use Eq. 6.6 independent of the knowledge of the luminosity, we define a relative cross section by normalizing Eq. 6.6 to the fixed detector ($\alpha_0 = 3.547°$) counts, which are also proportional to the integrated luminosity.

$$\left(\frac{d\sigma(\alpha)}{d\Omega} \Big/ \frac{d\sigma(\alpha_0)}{d\Omega}\right)_{\text{exp}} = \frac{NR^2}{A\cos^3\alpha} \Big/ \frac{N_0 R_0^2}{A_0\cos^3\alpha_0} \,, \tag{6.7}$$

where the 0 subscripts indicate fixed detector quantities. Notice that the above ratio is independent of luminosity and of absolute solid angles of detectors. Only ratios of solid angles subtended by the movable and fixed detectors occur in the expression.

6.5 Determination of the Forward Scattering Parameters

The theoretical expression for $d\sigma/d\Omega$ given in Eq. 2.27 has to be averaged over the finite geometries of the interaction region and the detector, and also over the interaction region density distribution before it can be used to compare with the measured cross sections.

The effect of the finite extensions in the z-direction of both the interaction region and the detector is to average the cross section over a range of recoil angles from $\alpha_{min}(z) = \alpha(z) - \Delta\alpha(z)$ to $\alpha_{max}(z) = \alpha(z) + \Delta\alpha(z)$, where z is the position of the interaction point with respect to the center of the interaction region. This leads to

$$\left\langle \frac{d\sigma(\alpha)}{d\Omega} \right\rangle = \int_{-d}^{d} \frac{dz}{(\alpha_{max}(z) - \alpha_{min}(z))} \int_{\alpha_{min}(z)}^{\alpha_{max}(z)} d\alpha' \frac{d\sigma(\alpha')}{d\Omega} \Big/ \int_{-d}^{d} dz \tag{6.8}$$

where d = 3.35 mm is the radius of the gas jet.

To take account of the interaction region density distribution the integrals over z have to be weighted by the density. Since the cross section of the gas jet is circular in the $y-z$ plane (as shown in Fig. 6.6, z is the beam direction, x is the gas jet direction and y is the vertical), the antiproton beam sees more protons at the center of the jet ($z = 0$) than near the edges ($z \approx \pm d$). Further, because the beam has a Gaussian density distribution, there are more antiprotons at the center of the beam ($y = 0$) than near the edges ($y \approx 2.3\sigma$, where $\sigma = 1.16$ mm is the width of the beam). When these density distributions of the gas jet and the antiproton beam are taken into account, Eq. 6.8 is modified to

$$\left\langle \frac{d\sigma(\alpha)}{d\Omega} \right\rangle = \int_{-d}^{d} \frac{dz}{(\alpha_{max}(z) - \alpha_{min}(z))} \int_{-\sqrt{d^2-z^2}}^{\sqrt{d^2-z^2}} dy \frac{1}{\sigma\sqrt{2\pi}} e^{-y^2/(2\sigma^2)} \times \int_{\alpha_{min}(z)}^{\alpha_{max}(z)} d\alpha' \frac{d\sigma(\alpha')}{d\Omega} \Big/ \int_{-d}^{d} dz \int_{-\sqrt{d^2-z^2}}^{\sqrt{d^2-z^2}} dy \frac{1}{\sigma\sqrt{2\pi}} e^{-y^2/(2\sigma^2)}. \tag{6.9}$$

With these averaged cross sections we construct the ratio

$$\left(\left\langle \frac{d\sigma(\alpha)}{d\Omega} \right\rangle \Big/ \left\langle \frac{d\sigma(\alpha_0)}{d\Omega} \right\rangle \right)_{\text{theory}} \tag{6.10}$$

which can now be compared with the measured experimental ratio of Eq. 6.7.

The measured ratios of Eq. 6.7 are fitted to the theoretical ratios of Eq. 6.10 by a χ^2 minimization procedure using the CERN library code MINUIT, where χ^2 is defined as

$$\chi^2 = \sum \left(\frac{\left(\frac{d\sigma(\alpha)}{d\Omega} \Big/ \frac{d\sigma(\alpha_0)}{d\Omega} \right)_{\text{exp}} - \left(\frac{d\sigma(\alpha)}{d\Omega} \Big/ \frac{d\sigma(\alpha_0)}{d\Omega} \right)_{\text{theory}}}{\Delta \left(\frac{d\sigma(\alpha)}{d\Omega} \Big/ \frac{d\sigma(\alpha_0)}{d\Omega} \right)_{\text{exp}}} \right)^2 \tag{6.11}$$

The fit was done using two different methods. In the first, which we call the "σ_T free" method, σ_T, b and ρ were all allowed to vary to obtain the best fit. In the

Table 6.2: Results for $\bar{p}p$ elastic scattering parameters from the "σ_T free" fit. The parentheses following the momenta in column one identify the charmonium resonance at which the data were taken. The errors in parentheses include the systematic errors indicated in the last row.

p_{lab} (GeV/c)	"σ_T-free" Analysis				σ_T(fit)/
	σ_T (mb)	b (GeV/c)$^{-2}$	ρ	χ^2/df	σ_T(world)
3.702 (η_c)	71.9(9)	12.6(5)	+0.018(15)	0.89	1.020(18)
4.066 (J/ψ)	67.8(15)	12.9(8)	−0.015(24)	0.60	0.988(26)
5.603 ($^1P_1$)	60.9(5)	12.6(3)	−0.047(8)	1.04	0.984(15)
5.724 (χ_2)	59.5(6)	12.7(4)	−0.051(12)	1.13	0.967(16)
5.941 (η_c')	59.1(5)	13.0(3)	−0.063(9)	1.19	0.970(16)
6.234 (ψ')	61.5(12)	11.7(6)	−0.006(20)	0.42	1.022(23)
Systematic errors	±0.24	±0.23	±0.004		

second method, which we call the "σ_T fixed" method, σ_T was fixed according to an external criterion, and only b and ρ were allowed to vary to obtain the best fit to the differential cross sections.

The first method ("σ_T free") of determining the scattering parameters, in which σ_T, b and ρ were all allowed to vary in the fit, has been rarely used in previous experiments, because its success depends on knowing the differential cross sections very precisely either by an independent measurement of luminosity or by absolute Coulomb normalization in the very low momentum transfer region ($|t| \leq 0.001$ (GeV/c)^2). Accurate measurements in this region of $|t|$ are generally difficult to make. However, since our measurements extend to $|t|$ as small as 0.0004 (GeV/c)^2, we have attempted to analyze our data by the "σ_T free" method. The results of this analysis are given in Table 6.2. Our results for the total cross sections (column 2 of Table 6.2) have errors less than 2% and , as indicated in column 5, they differ by less than two standard deviations from the predictions of the fit to the world data described in Appendix

B1. We note, however, that fluctuations in our results for σ_T are accompanied by corresponding fluctuations in the values of b and ρ. This is, of course, the consequence of correlations between the three parameters.

The correlations between the scattering parameters are shown in Fig. 6.7 for a typical case, p = 4.07 GeV/c, and are found to be $C(b,\sigma_T) = -0.557$, $C(b,\rho) = -0.793$, and $C(\rho,\sigma_T) = 0.919$. The largest correlation exists between ρ and σ_T. As a result, a substantial part of the fluctuations in the results for the ρ parameter are induced by the fluctuations in σ_T.

It is desirable to remove the correlation-induced fluctuations in the most sensitive parameters by introducing sensible constraints on one or more of the other parameters. This is usually done by fixing σ_T to values obtained from a fit to the world data for σ_T. Since the world data in our region of interest are extremely fragmentary and have large errors (see Table B1) we have adopted a different procedure. We have fit our results for σ_T in Table 6.2 along with the world data in the limited region $2 \leq p \leq 8$ GeV/c, with the commonly used expression $\sigma_T = A + Bp^n$. The best fit yielded A = 34.48(17) mb, B =89.7(10) mb, and n = -0.702(28). The data and the fit are shown in Fig. 6.8. The values of σ_T obtained with these parameters were then used as the fixed values of σ_T to obtain the best fit to our differential cross section data by varying only b and ρ. The results of this "σ_T-fixed" analysis are presented in Table 6.3. As expected, the large fluctuations in b and ρ values of the "σ_T-free" analysis are no longer present. We consider the "σ_T-fixed" results to be our final results for b and ρ. The results for σ_T in Table 6.2 remain our best independent results for the total cross sections.

The errors given in the first six rows of Tables 6.2 and 6.3 include all statistical and

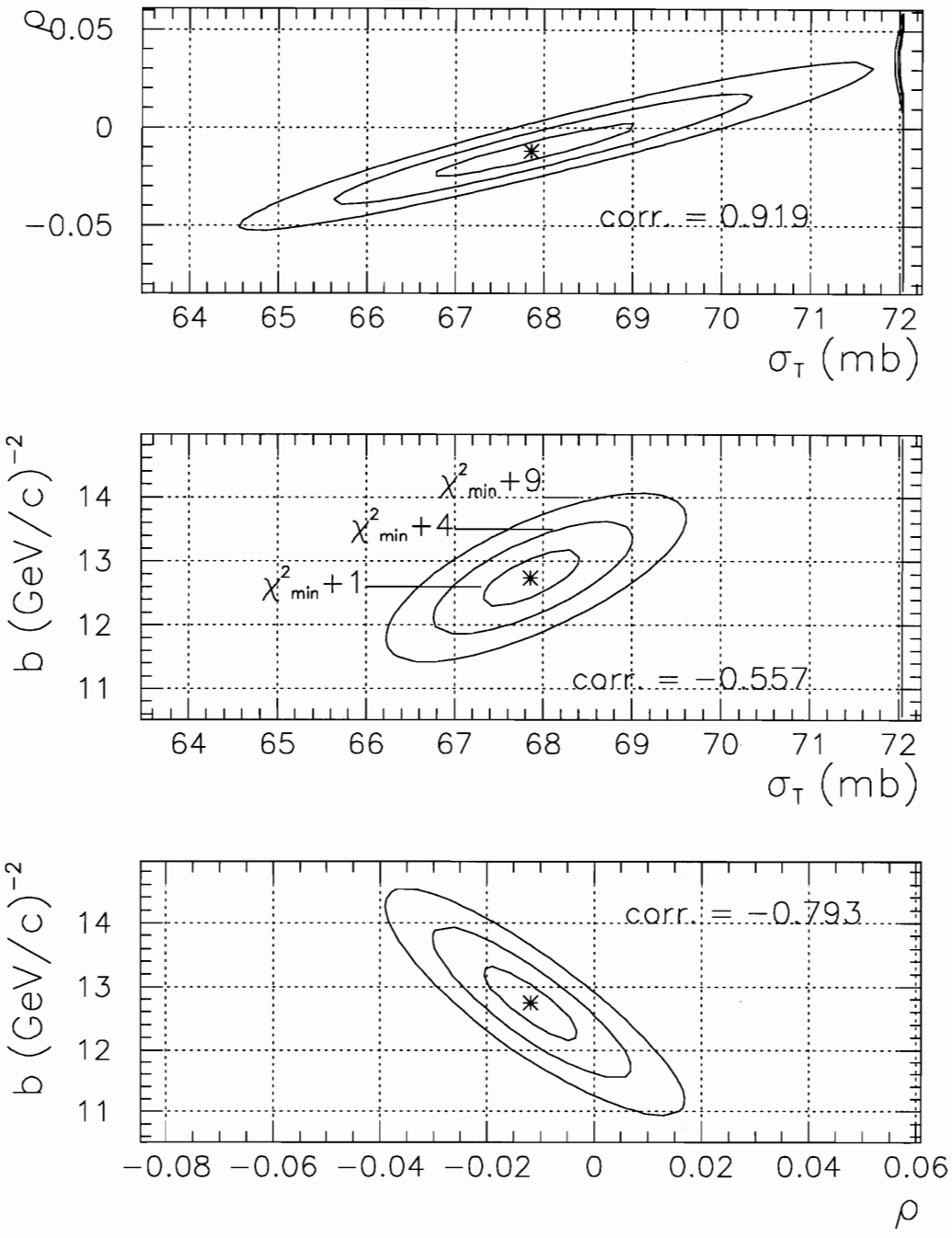

Figure 6.7: Correlations between the three scattering parameters for the data set at $p = 4.07$ GeV/c. The central values of the parameters correspond to those obtained in the fit when all three parameters varied freely (see Table 6.2).

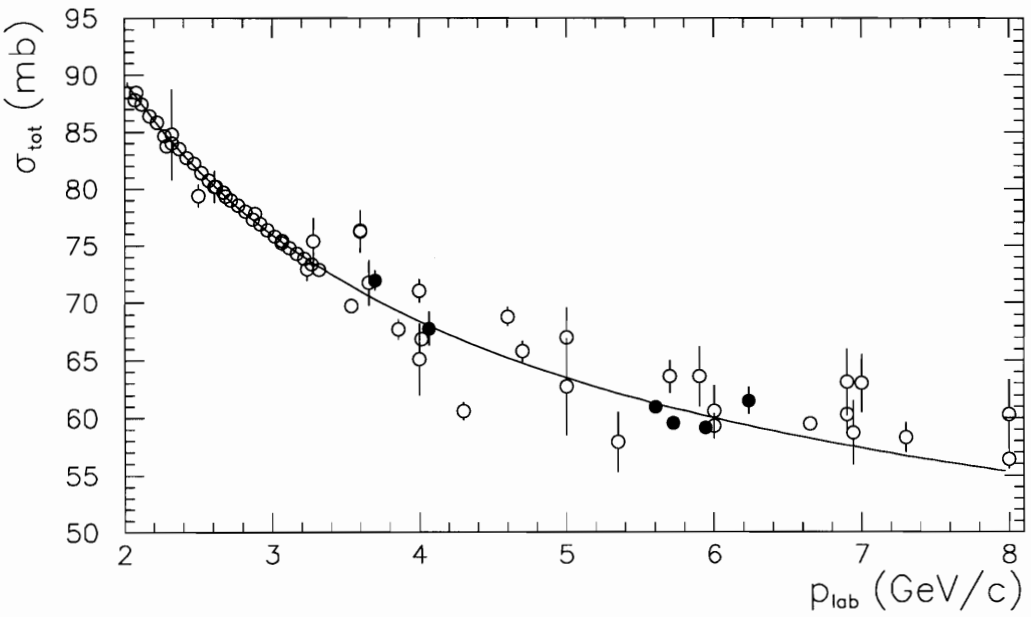

Figure 6.8: World data on $\bar{p}p$ total cross sections in the 2 – 8 Gev/c momentum range. Results of this experiment are shown as filled circles. The curve shows the fit described in the text.

Table 6.3: Results for $\bar{p}p$ elastic scattering parameters from the "σ_T fixed" fit. The parentheses following the momenta in column one identify the charmonium resonance at which the data were taken. The errors in parentheses include the systematic errors indicated in the last row.

		"σ_T-fixed" Analysis		
p_{lab} (GeV/c)	σ_T (mb)	b (GeV/c)$^{-2}$	ρ	χ^2/df
3.702 (η_c)	70.3	12.9(4)	0.006(8)	0.90
4.066 (J/ψ)	68.0	12.8(7)	−0.007(12)	0.60
5.603 ($^1P_1$)	61.3	12.5(3)	−0.030(7)	1.04
5.724 (χ_2)	60.9	12.2(4)	−0.018(8)	1.20
5.941 (η_c')	60.2	12.6(3)	−0.035(8)	1.26
6.234 (ψ')	59.4	12.2(6)	−0.029(10)	0.50
Systematic errors	±0.25	±0.24	±0.0066	

fitting errors and the random uncertainties in the energy calibration and background subtraction procedures. In addition, the systematic errors described below, and listed separately in the last rows of the tables, have been added in quadrature.

The resulting differential cross section data and the best fits to it obtained from the "σ_T fixed" analysis are shown in Fig. 6.9 and are tabulated in Appendix A.

6.6 Systematic Errors

In addition to the random errors discussed above, there are three main sources of systematic error. Their contribution to the uncertainty in the fitted parameters was determined by simulating their variation by ± one standard deviation individually and refitting the data.

The first source of systematic error is the ±0.1% uncertainty in the values of the relative areas of the different detectors which were used to normalize their counts.

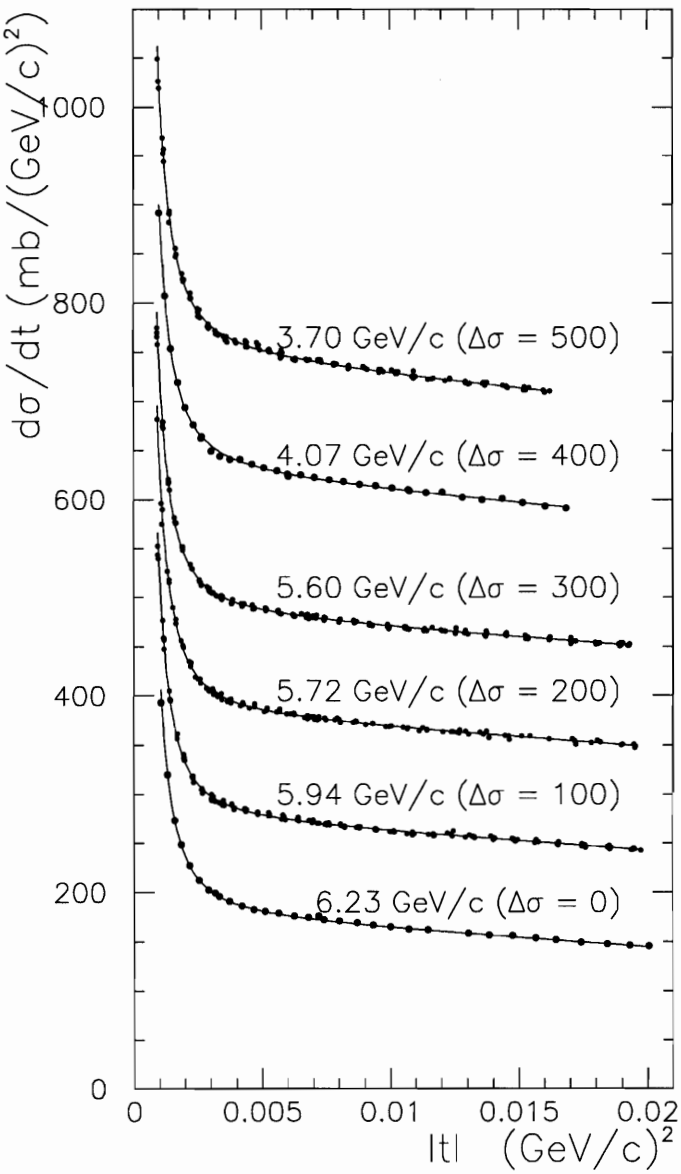

Figure 6.9: The measured differential cross sections (increased as indicated by amounts $\Delta\sigma$ (mb/(GeV/c)^2) for display purposes) for six beam momenta. Only the statistical errors are shown, and in most cases they are smaller than the size of the points. The solid lines represent the fits to the data.

The second source arises from the uncertainty in the determination of t due to the $\pm 0.2\%$ systematic errors in the detector energy calibration (thickness of the absorber on the alpha source, thickness of the detector entrance window and dead layer). The third source of systematic error applies only to the "σ_T-fixed" analysis and is due to the $\approx \pm 0.4\%$ uncertainty in the value of the total cross section as determined by the fit to the data described in Sec. 6.5 and displayed in Fig. 6.8. A summary of the systematic errors due to the sources described above is given in Table 6.4. The final values of b and ρ with overall errors listed in Table 6.3 are displayed in Fig. 6.10. We note that the errors in our ρ parameter values are more than a factor five smaller than those of previous measurements. [57,58]

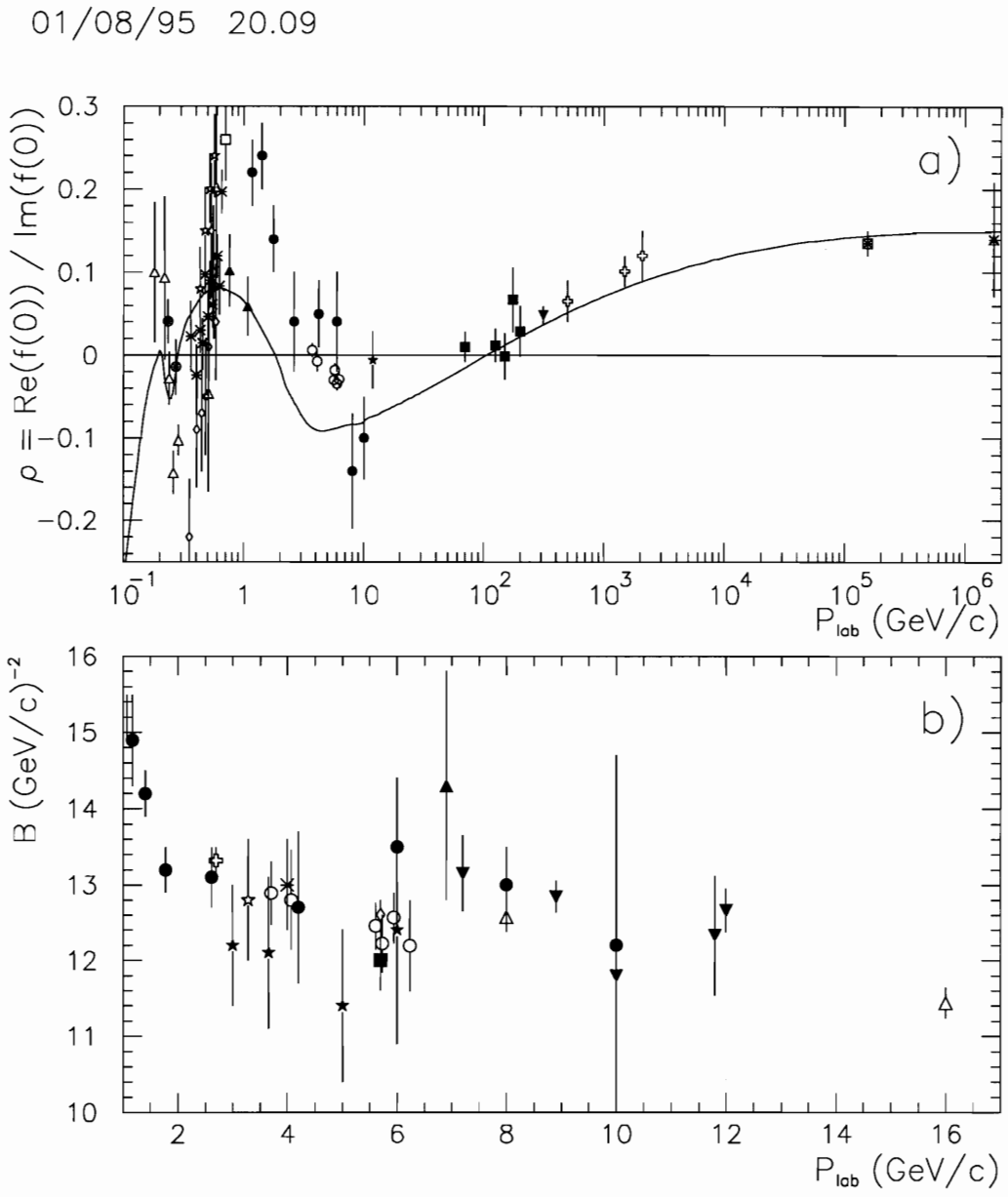

Figure 6.10: Results for the ρ- and b-parameters from the present experiment (open circles) along with the existing world data. The world data and the references to their sources are given in Tables B.5 and B.7. The solid curve in the ρ plot is the dispersion relation prediction due to Kroll and Schweiger [2].

Table 6.4: Systematic errors contribution to σ_T, b and ρ. The errors on σ_T apply only to the "σ_T free" fit.

Source	Uncertainty	Error in:	b $(\mathrm{GeV/c})^{-2}$	ρ	σ_T (mb)
Detector area	$\pm 0.1\%$		± 0.18	± 0.0024	± 0.23
Energy calibration	$\pm 0.2\%$		± 0.14	± 0.0035	± 0.07
Total cross section	$\pm 0.4\%$		± 0.08	± 0.0050	
Total error	"σ_T free"		± 0.23	± 0.0042	± 0.24
	"σ_T fixed"		± 0.24	± 0.0066	

Chapter 7

Discussion of Results

7.1 Results for the ρ Parameter

As mentioned in Chapter 1, several theoretical approaches have been developed to describe forward elastic scattering of hadrons. These have been extensively reviewed by Block and collaborators [6]. All such approaches are based on the fundamental properties of unitarity, analyticity, and crossing symmetry that the scattering amplitude must possess. Two of the more popular of these analyses are those based on dispersion relations and those based on the direct use of analytic amplitudes.

In the dispersion theory analysis, the unitarity, analyticity, and crossing symmetry properties are used not to construct the amplitudes themselves, but to obtain integral dispersion relations which express the real part of an amplitude in terms of integrals over the imaginary parts. The integrals extend from $\sqrt{s} = 0$ to ∞ for the pp amplitude and $\sqrt{s} = 2m_\pi$ to ∞ for the $\bar{p}p$ amplitude. The imaginary parts of the amplitudes are obtained from total cross section data (via the optical theorem) in the physically accessible domain, $\sqrt{s} = 2m \rightarrow \infty$, and in terms of contributions of poles and cuts in the unphysical region, $\sqrt{s} = 2m_\pi \rightarrow 2m$. Since the contributions from the unphysical region are explicitly taken into account, and fits to measured cross sections containing

the effect of important resonances in the physical region are used, dispersion relation analysis can be used in principle to predict ρ all the way down to the physical threshold at $\sqrt{s} = 2m$. In practice, the evaluation of the contributions of poles and cuts in the unphysical region presents a serious challenge.

The analytic amplitude method avoids the problems of resonance and pole contributions by confining its interest in the region $\sqrt{s} \geq 5$ GeV (equivalent $p_{\rm lab} = 12$ GeV/c) where such contributions are known to be negligibly small. It uses the unitarity, analyticity, and crossing symmetry properties of the scattering amplitudes to directly construct such amplitudes. The parameters which enter these amplitudes are obtained by fitting the total cross section and ρ-parameter data for pp and $\bar{p}p$ scattering for $\sqrt{s} \geq 5$ GeV. Once the parameters of the fit have been obtained, the ρ-parameter is analytically determined.

7.1.1 The Analytic Amplitude Analysis of Block et al.

Block et al. [3] write the even and odd analytic amplitudes for pp and $\bar{p}p$ scattering as

$$\frac{4\pi}{p} f_+ = i\left(A + \beta\left[\log\left(\frac{s}{s_0}\right) - i\frac{\pi}{2}\right] + cs^{\mu-1}e^{i\pi(1-\mu)/2}\right) \tag{7.1}$$

$$\frac{4\pi}{p} f_- = -Ds^{\alpha-1}e^{i\pi(1-\alpha)/2} \tag{7.2}$$

for the case where the total cross sections are assumed to rise asymptotically as $\log(s/s_0)$. In terms of these amplitudes, the measurable quantities are

$$\sigma_{\bar{p}p} = \frac{4\pi}{p}\mathrm{Im}(f_+ + f_-)\,, \qquad \sigma_{pp} = \tfrac{4\pi}{p}\mathrm{Im}(f_+ - f_-) \tag{7.3}$$

$$\rho_{\bar{p}p} = \mathrm{Re}(f_+ + f_-)/\mathrm{Im}(f_+ + f_-)\,, \quad \rho_{pp} = \mathrm{Re}(f_+ - f_-)/\mathrm{Im}(f_+ - f_-)\,. \tag{7.4}$$

The parameters A, β, s_0, D, α, c, and μ are determined by fitting both the total cross section and ρ-parameter data for pp and $\bar{p}p$ for energies between 5 and 1800 GeV. The best fit values found by Block et al. are [3]

$$A = -0.6 \pm 1.4 \text{ mb}\,, \quad \beta = 7.7 \pm 0.1 \text{ mb}\,, \quad s_0 = 500 \text{ GeV}^2\,, \quad \mu = 0.83 \pm 0.01 \tag{7.5}$$

$$c = 124 \pm 2 \text{ mb GeV}^{2(1-\alpha)}\,, \quad D = -44.2 \pm 2.1 \text{ mb GeV}^{2(1-\alpha)}\,, \quad \alpha = 0.44 \pm 0.01 \tag{7.6}$$

The total cross section fits from this analysis are shown in Fig. 7.1. Note that these fits depart substantially from the data for $p_{\text{lab}} < 12$ GeV/c ($\sqrt{s} < 5$ GeV), the region which was not included in the fits. The corresponding ρ-parameter predictions are shown in Fig. 7.2. They agree very well with the data in the region of the fit. Although these predictions are not meant to be used for $p_{\text{lab}} < 12$ GeV/c, we note that they are in reasonable agreement with our results in the 3.5 to 6.2 GeV/c region.

7.1.2 The Dispersion Relations Analysis of Kroll and Schweiger

Our measurements of the ρ-parameter are in the range 3.5 to 6.2 GeV/c. As mentioned earlier, this energy region receives substantial contributions from resonances in both the physical and unphysical regions. In this region attempts to fit the data have been made only in terms of dispersion relations. The latest such attempt is due to Kroll and Schweiger.

Kroll and Schweiger write the once-subtracted dispersion relation as [2, 33]

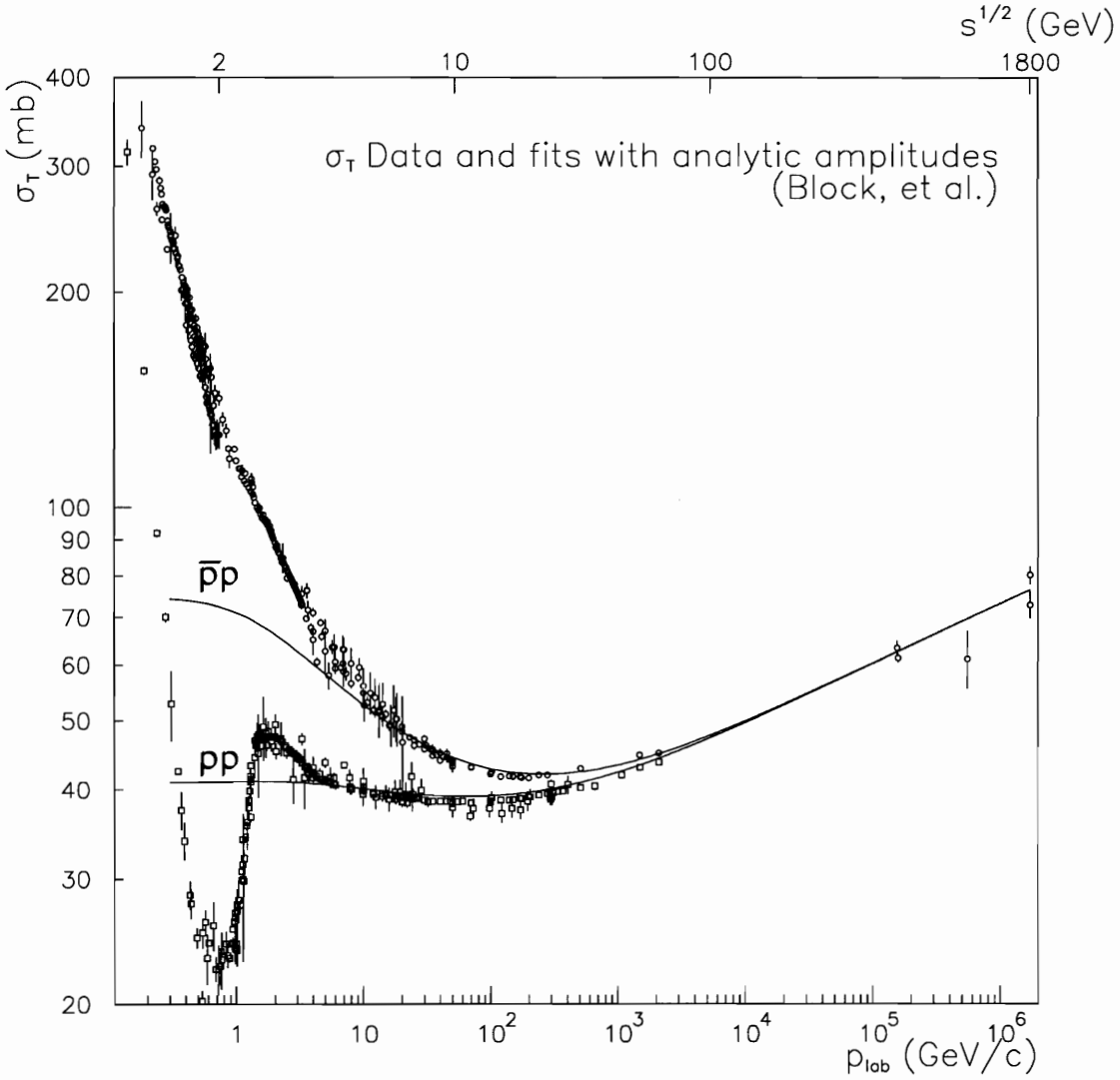

Figure 7.1: Fits to the pp and $\bar{p}p$ total cross sections using the analytic amplitudes of Block et al. [3]. The data and the references to their sources are given in Tables B.1 and B.3.

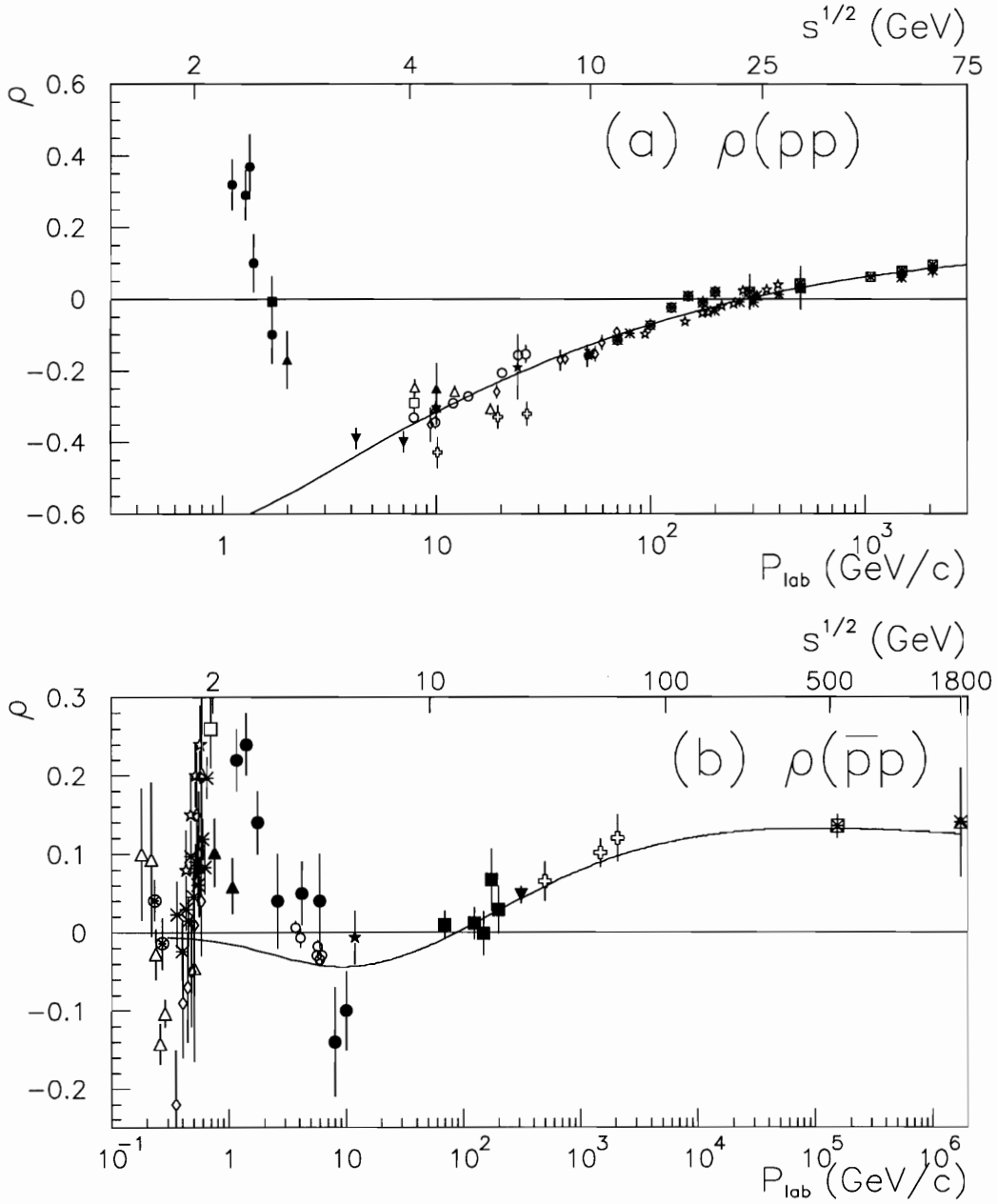

Figure 7.2: Fits to the pp and $\bar{p}p$ ρ-parameter data using the analytic amplitudes of Block et al. [3]. The data and the references to their sources are given in Tables B.6 and B.7.

$$\begin{aligned}
\mathrm{Re}f_{\bar{p}p}(\omega_0) &= \mathrm{Re}f_{pp}(m) - \frac{1}{4m}\frac{g_\pi^2}{4\pi}\frac{\omega_0+m}{\omega_0-\omega_\pi} \\
&+\frac{\omega_0+m}{\pi}\left(\int_m^\infty \frac{\mathrm{Im}f_{\bar{p}p}(\omega)d\omega}{(\omega-\omega_0)(\omega+m)} - \int_m^\infty \frac{\mathrm{Im}f_{pp}(\omega)d\omega}{(\omega+\omega_0)(\omega-m)}\right) \\
&+\frac{\omega_0+m}{\pi}\int_{\omega_{2\pi}}^m \frac{\mathrm{Im}f_{\bar{p}p}(\omega)d\omega}{(\omega-\omega_0)(\omega+m)}\,, \qquad (7.7)
\end{aligned}$$

where ω_0 is the energy of the incident particle in the laboratory frame, $\omega_\pi = m_\pi^2/(2m) - m$ is the position of the pion pole, and $\omega_{2\pi} = 2m_\pi^2/m - m$ is the beginning of the unphysical cut. The subtraction constant $\mathrm{Re}f_{pp}(m)$ is equal to the pp scattering length, -17.1 fm [36]. We note that all but the last term involve quantities which can be experimentally measured, i.e., scattering lengths and imaginary parts of the scattering amplitudes. The last term represents the amplitude in the unphysical region ($\omega < m$) which is inaccessible to direct measurements.

In order to calculate the integrals over the imaginary part of the forward amplitudes, Kroll and Schweiger used parametrizations of the $\bar{p}p$ total cross section data from $T = 10$ MeV up to $\sqrt{s} = 1800$ GeV, and pp data from $T = 10$ MeV up to $\sqrt{s} = 63$ GeV. At energies below those of the lowest energy measurements, they approximated the amplitudes using effective range expansions. At energies above those of the highest energy measurements they used asymptotic expressions constructed so that the difference between the pp and $\bar{p}p$ total cross sections approaches zero at infinite energy.

$$\sigma_{T,pp} = \sigma_0 + \sigma_1\left(\ln\frac{\omega}{\omega_0}\right)^2 \qquad (7.8)$$

$$\sigma_{T,\bar{p}p} = \sigma_{T,pp} + \sigma_2(\omega/\mathrm{GeV})^{\alpha-1}\,, \qquad (7.9)$$

The total cross sections used by Kroll and Schweiger are shown in Fig. 7.3.

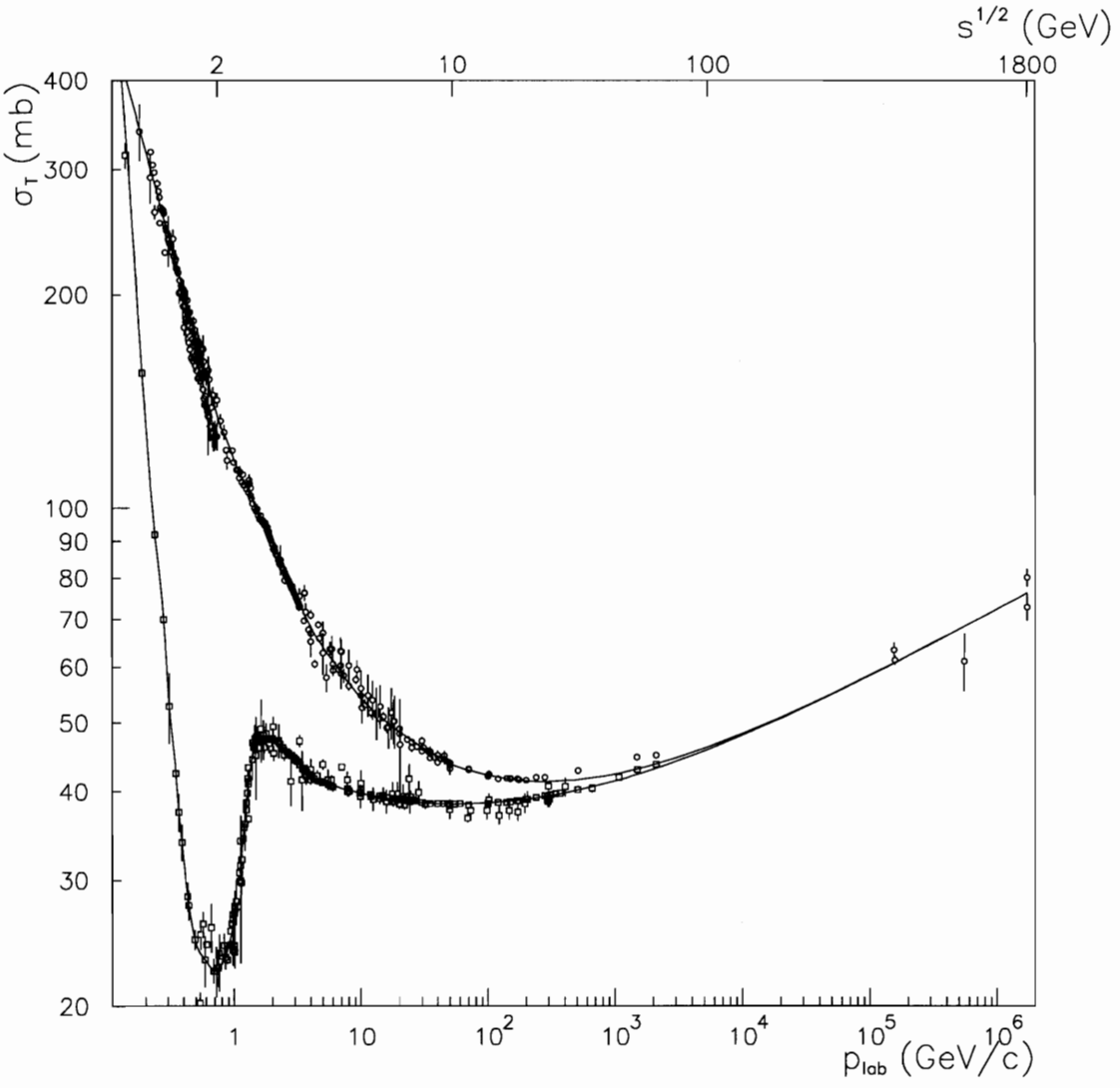

Figure 7.3: Total cross section fits used by Kroll and Schweiger in their dispersion relation analysis.

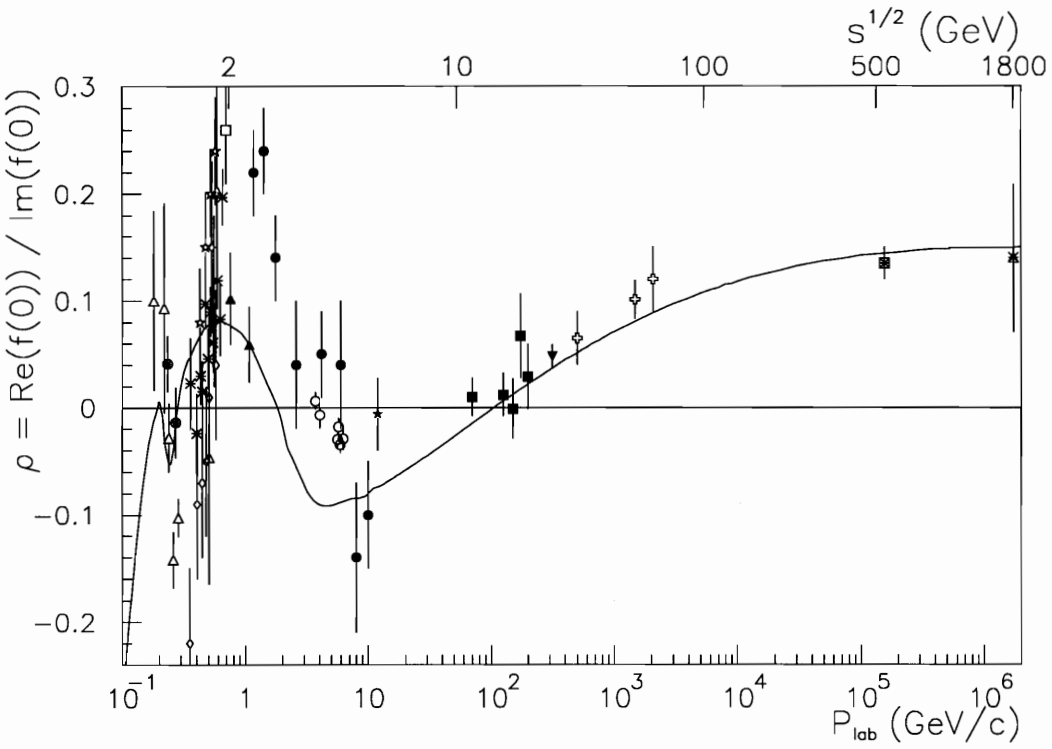

Figure 7.4: The dispersion theory prediction of Kroll and Schweiger [2]. The results of the present experiment are shown as open circles. The data and the references to their sources are given in Table B.7.

In the unphysical region Kroll and Schweiger used the results of an analysis by Grein and Kroll [34] which included the two and three pion continuum contributions as well as pole terms due to the ω and A_1, with masses 782 and 1100 MeV, and coupling constants 8.1 and 7.3, respectively. These were chosen to fit the low energy ρ data from LEAR. Kroll and Schweiger's predictions of the $\bar{p}p$ ρ parameter are shown in Fig. 7.4. The precision results of the present experiment are shown in the figure as open circles. They are in clear disagreement with the dispersion theory prediction.

7.2 Results for the b-Parameter

Unlike the ρ-paramter, there are not many theoretical models for the slope parameter, b. This is because the concept of a constant slope in the small $|t|$ region is largely a phenomenological idea, and the definition of the small $|t|$ region is somewhat arbitrary. In Sec. 2.2, Eq. 2.15, we mentioned that in the approximation in which the particles have Gaussian matter densities, the slope parameter is independent of energy,

$$b = R^2 \ . \tag{7.10}$$

Considering the convolution of two colliding disks, each with rms radius $\sim$ 0.8 fm, $R = 1.13$ fm $= 5.66$ (GeV/c)$^{-1}$, which leads to $b = 16$ (GeV/c)$^{-2}$ [43]. As Illustrated in Fig. 7.5 this is close to the average value of b determined from analyses of the forward scattering data, but it tells us nothing about the energy variation of b, which is clearly visible in the figure.

Block and Cahn [6] have given arguments to show that the energy variation of b should generally follow that of σ_T. They have suggested that the parametrization of b for the even and odd amplitudes should be

$$b^+(s) = C^+ + D^+ \ln s + E^+ \ln^2 s \tag{7.11}$$

$$b^-(s) = C^- + D^- \ln s \ , \tag{7.12}$$

so that,

$$b(s) = b^+(s) \pm \frac{\sigma^-}{\sigma^+} \left(b^-(s) - b^+(s) \right) \ . \tag{7.13}$$

Using these relations, Block and Cahn fitted the experimental data available to them in 1985. Their fit is illustrated in Fig 7.5.

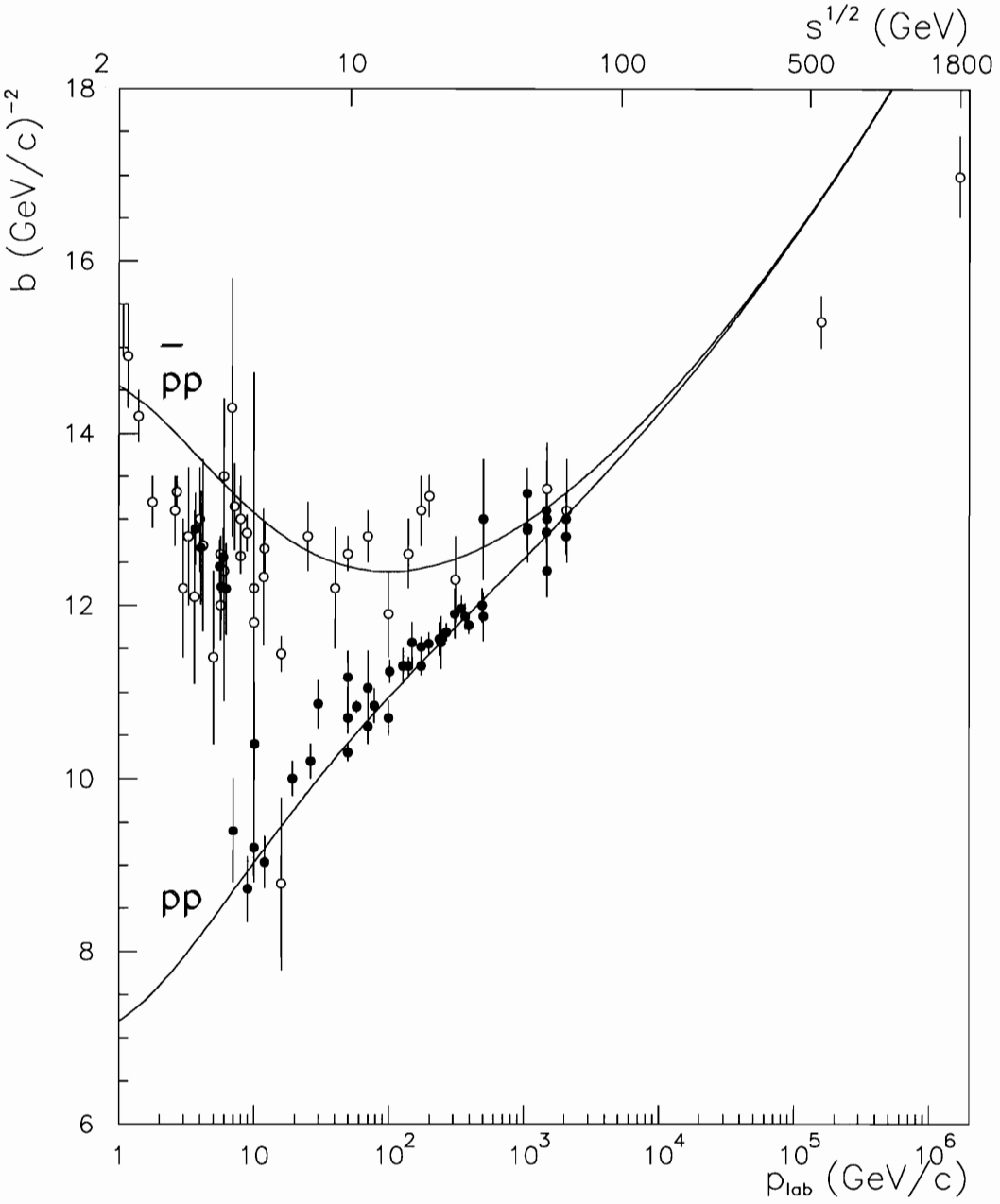

Figure 7.5: World data on the b parameter. The results of the present experiment are shown as the six solid points in the $\bar{p}p$ data set. The curves show the fits of Block et al. [6]. The data and the references to their sources are given in Table B.5.

7.3 Summary and Conclusions

In this dissertation we have presented the results of precision measurements of relative differential cross sections for $\bar{p}p$ elastic scattering at very small momentum transfers for six values of incident antiproton momenta in the range 3.5 to 6.2 GeV/c. The experimental technique used was to measure recoil proton spectra in the vicinity of 90° with excellent signal to background ratio and energy resolution obtained by using solid state detectors. The data were analyzed for the forward scattering parameters b (the nuclear slope parameter) and ρ (the ratio of the real to the imaginary part of the forward scattering amplitude), using values of the total cross sections obtained from a fit to the world data. The resulting values of ρ have errors which are a factor three to four smaller than the errors in previous measurements. Our results for b are in general agreement with earlier published results.

The measured values of ρ have been compared with existing theoretical predictions. It is found that the latest dispersion theory predictions are in serious disagreement with our precision results. Since dispersion theory calculations for the ρ parameter for $p_{lab} \leq 100$ GeV/c receive major contributions from the unphysical region, our data should help constrain the parameters of the unphysical region (poles and cuts) in an important way. Additional data of similar precision in the regions $p_{\rm lab} < 3.5$ GeV/c and $p_{\rm lab}$ from 6.2 to 70 GeV/c would further enhance our knowledge of the physics of the unphysical region. The success of our recoil technique suggests that it can be used to obtain such high precision data in both momentum regions.

Appendix A

Differential Cross Sections from the Present Experiment

The following tables contain the differential cross section results from the present experiment at each of the six incident antiproton momenta which range from 3.702 to 6.234 GeV/c. The errors given in columns 2 and 4 contain the effects due to counting statistics as well as the random errors associated with energy calibration and background subtraction. The systematic errors are described in Sec. 6.6 and are not included in these tables.

The differential cross sections listed are acceptance weighted averages over an interval $\pm\Delta t$ because of the finite geometry of the measurements. The quantity Δt is approximately given by

$$\Delta t \approx \left(4m\sqrt{t/\kappa}\Delta\alpha\right) = 0.02293 \text{ GeV/c } \sqrt{t/\kappa} \tag{A.1}$$

where $\kappa = (E_{beam} + m)/(E_{beam} - m)$ and $\Delta\alpha = 0.00611$. Thus, the averaging interval is

$$\pm\Delta t \approx \pm 0.0005 \text{ (GeV/c)}^2 \text{ at } t = 0.001 \text{ (GeV/c)}^2 \text{ to}$$

$$\pm\Delta t \approx \pm 0.0024 \text{ (GeV/c)}^2 \text{ at } t = 0.020 \text{ (GeV/c)}^2$$

over the range of incident antiproton momenta from 3.7 to 6.2 GeV/c.

Table A.1: Differential cross section results for $p_{\text{lab}} = 3.702$ GeV/c.

$\lvert t\rvert$	$d\sigma/dt$	$\lvert t\rvert$	$d\sigma/dt$
$(\text{GeV/c})^2$	$(\text{mb}/(\text{GeV/c})^2)$	$(\text{GeV/c})^2$	$(\text{mb}/(\text{GeV/c})^2)$
0.000948	536.157 ± 9.45	0.003189	265.889 ± 3.23
0.000970	514.498 ± 8.99	0.003233	262.664 ± 3.23
0.001004	507.356 ± 8.76	0.003309	261.281 ± 3.00
0.001141	457.358 ± 4.38	0.003534	260.129 ± 3.00
0.001169	441.920 ± 4.84	0.003589	256.904 ± 3.00
0.001190	446.298 ± 4.38	0.003632	259.668 ± 3.00
0.001196	434.086 ± 4.84	0.003653	254.139 ± 3.00
0.001384	381.784 ± 3.69	0.003958	256.443 ± 3.00
0.001395	372.798 ± 3.46	0.003994	254.830 ± 2.76
0.001412	383.858 ± 3.69	0.004012	254.369 ± 3.00
0.001420	380.862 ± 3.92	0.004014	253.447 ± 3.00
0.001639	347.453 ± 3.00	0.004379	255.291 ± 3.46
0.001657	339.159 ± 3.23	0.004412	249.531 ± 5.07
0.001661	341.463 ± 3.23	0.004437	254.600 ± 3.23
0.001675	341.002 ± 3.00	0.004448	249.531 ± 2.76
0.001913	321.648 ± 2.76	0.004819	253.908 ± 3.23
0.001922	316.579 ± 2.53	0.004857	250.683 ± 2.76
0.001945	314.275 ± 2.76	0.004882	251.604 ± 2.76
0.001981	315.888 ± 2.76	0.004933	246.535 ± 2.76
0.002219	302.985 ± 2.53	0.005263	245.844 ± 2.07
0.002224	298.377 ± 2.30	0.005311	245.844 ± 3.00
0.002224	296.764 ± 4.15	0.005312	244.231 ± 3.69
0.002229	298.146 ± 2.76	0.005314	247.457 ± 3.00
0.002244	297.455 ± 2.53	0.005362	244.231 ± 2.76
0.002505	287.778 ± 2.30	0.005705	242.618 ± 1.84
0.002520	284.322 ± 2.30	0.005738	238.471 ± 1.84
0.002535	283.631 ± 2.30	0.005747	244.001 ± 1.84
0.002537	279.714 ± 2.07	0.005750	243.540 ± 2.76
0.002544	279.714 ± 3.46	0.005759	245.844 ± 2.76
0.002565	286.396 ± 3.69	0.005768	241.006 ± 1.84
0.002602	278.792 ± 7.14	0.005791	239.623 ± 2.53
0.002892	270.037 ± 3.23	0.005808	243.540 ± 2.76
0.002917	272.341 ± 3.46	0.006231	237.319 ± 1.61
0.002940	270.037 ± 3.23	0.006283	236.858 ± 1.84
0.002943	267.963 ± 3.46	0.006315	238.241 ± 1.84

$p_{\text{lab}} = 3.702$ GeV/c, *continued.*

$\lvert t\rvert$ $(\text{GeV/c})^2$	$d\sigma/dt$ $(\text{mb}/(\text{GeV/c})^2)$	$\lvert t\rvert$ $(\text{GeV/c})^2$	$d\sigma/dt$ $(\text{mb}/(\text{GeV/c})^2)$
0.006333	236.167 ± 1.84	0.010326	224.877 ± 1.38
0.006730	237.319 ± 1.84	0.010860	220.499 ± 2.07
0.006796	236.167 ± 1.84	0.010930	225.799 ± 2.07
0.006869	236.397 ± 1.61	0.010933	218.656 ± 2.07
0.007205	235.706 ± 1.61	0.011007	220.269 ± 2.07
0.007207	236.628 ± 1.84	0.011496	217.504 ± 2.07
0.007307	236.397 ± 1.61	0.011622	217.965 ± 2.07
0.007340	234.093 ± 1.61	0.011699	218.886 ± 2.07
0.007810	232.480 ± 1.61	0.012158	216.582 ± 2.07
0.007838	232.941 ± 1.61	0.012160	216.352 ± 1.84
0.007838	231.098 ± 1.84	0.012335	217.734 ± 2.07
0.007930	232.711 ± 1.61	0.012353	218.886 ± 2.07
0.008386	227.872 ± 1.61	0.012933	215.661 ± 2.07
0.008387	230.407 ± 1.61	0.012953	213.818 ± 1.84
0.008415	231.328 ± 1.61	0.013064	212.896 ± 2.07
0.008420	229.024 ± 1.61	0.013110	213.126 ± 1.84
0.008959	229.946 ± 1.61	0.013617	213.357 ± 1.84
0.009038	228.333 ± 1.61	0.013662	214.509 ± 2.07
0.009066	228.564 ± 1.38	0.013719	211.744 ± 2.07
0.009122	227.181 ± 1.61	0.013783	214.739 ± 2.07
0.009578	224.416 ± 1.38	0.014392	211.513 ± 1.84
0.009596	227.872 ± 2.30	0.014521	210.592 ± 2.07
0.009659	227.181 ± 1.38	0.014548	210.822 ± 1.84
0.009675	226.490 ± 1.38	0.014585	209.209 ± 1.84
0.009744	224.647 ± 1.61	0.015222	207.136 ± 1.84
0.010066	226.720 ± 2.30	0.015240	209.901 ± 1.84
0.010211	224.416 ± 1.61	0.015287	207.136 ± 1.84
0.010228	223.034 ± 1.38	0.015415	209.209 ± 1.84
0.010232	225.338 ± 2.07	0.015969	206.675 ± 1.84
0.010238	223.725 ± 2.07	0.016015	204.601 ± 1.84
0.010249	224.186 ± 1.38	0.016052	205.062 ± 1.84
0.010278	223.264 ± 2.53	0.016236	205.523 ± 1.84

Table A.2: Differential cross section results for $p_{\mathrm{lab}} = 4.066$ GeV/c.

$\lvert t\rvert$	$d\sigma/dt$	$\lvert t\rvert$	$d\sigma/dt$
$(\mathrm{GeV/c})^2$	$(\mathrm{mb}/(\mathrm{GeV/c})^2)$	$(\mathrm{GeV/c})^2$	$(\mathrm{mb}/(\mathrm{GeV/c})^2)$
0.001008	488.032 ± 8.16	0.006524	223.726 ± 1.50
0.001235	404.725 ± 3.65	0.007055	221.364 ± 1.50
0.001467	351.477 ± 3.01	0.007632	218.788 ± 1.50
0.001747	317.124 ± 2.58	0.008204	216.855 ± 1.29
0.002027	292.003 ± 2.58	0.008813	213.849 ± 1.29
0.002352	274.612 ± 2.15	0.009455	212.776 ± 1.29
0.002651	260.441 ± 1.93	0.010106	210.629 ± 1.29
0.002677	262.159 ± 3.44	0.010714	209.340 ± 1.93
0.003043	247.988 ± 4.51	0.010761	207.623 ± 1.29
0.003373	242.620 ± 3.01	0.011416	205.905 ± 1.93
0.003778	239.185 ± 2.58	0.012052	206.979 ± 1.93
0.004178	239.614 ± 2.58	0.012827	201.396 ± 1.72
0.004642	234.461 ± 2.58	0.013584	198.605 ± 1.72
0.005092	230.811 ± 2.58	0.014377	200.323 ± 1.72
0.005600	227.805 ± 2.58	0.015170	195.599 ± 1.72
0.006030	224.370 ± 1.72	0.016047	192.378 ± 1.72
0.006057	222.438 ± 2.58	0.016868	190.446 ± 1.72

Table A.3: Differential cross section results for $p_{\text{lab}} = 5.603$ GeV/c.

$\lvert t\rvert$ $(\text{GeV/c})^2$	$d\sigma/dt$ $(\text{mb}/(\text{GeV/c})^2)$	$\lvert t\rvert$ $(\text{GeV/c})^2$	$d\sigma/dt$ $(\text{mb}/(\text{GeV/c})^2)$
0.000923	463.111 ± 7.70	0.002578	215.480 ± 1.54
0.000929	467.387 ± 8.04	0.002583	216.677 ± 1.71
0.000930	471.833 ± 7.87	0.002602	214.796 ± 1.37
0.000940	464.650 ± 7.70	0.002611	213.941 ± 1.71
0.000961	455.245 ± 8.21	0.002614	214.112 ± 1.37
0.001146	372.644 ± 6.16	0.002640	211.034 ± 1.37
0.001147	377.090 ± 6.33	0.002884	210.008 ± 2.74
0.001147	375.209 ± 5.99	0.002923	207.955 ± 1.54
0.001147	357.594 ± 5.81	0.002938	207.784 ± 1.37
0.001161	377.090 ± 6.33	0.002949	205.732 ± 1.71
0.001167	370.421 ± 6.50	0.002962	205.903 ± 2.22
0.001362	319.287 ± 2.91	0.002962	205.903 ± 1.37
0.001369	318.432 ± 2.57	0.002965	208.126 ± 2.39
0.001375	314.840 ± 3.59	0.002980	204.706 ± 1.37
0.001379	312.275 ± 2.39	0.002984	204.877 ± 1.37
0.001390	315.867 ± 2.57	0.003011	208.298 ± 2.22
0.001411	308.171 ± 3.25	0.003066	203.509 ± 1.37
0.001605	280.124 ± 2.57	0.003091	203.509 ± 1.54
0.001622	275.507 ± 2.05	0.003095	203.680 ± 1.54
0.001637	273.284 ± 2.05	0.003230	200.944 ± 2.22
0.001650	273.797 ± 2.05	0.003239	200.431 ± 2.22
0.001653	274.139 ± 2.05	0.003240	200.260 ± 2.74
0.001661	274.652 ± 2.22	0.003409	198.208 ± 2.22
0.001911	250.025 ± 2.05	0.003412	201.628 ± 2.22
0.001921	247.973 ± 1.88	0.003421	200.773 ± 2.39
0.001927	247.973 ± 2.05	0.003424	199.918 ± 2.22
0.001928	246.776 ± 1.71	0.003443	196.839 ± 2.22
0.001936	250.538 ± 1.88	0.003482	199.576 ± 2.39
0.001939	246.776 ± 1.71	0.003827	192.735 ± 2.05
0.002216	232.411 ± 1.88	0.003830	193.761 ± 2.22
0.002227	232.240 ± 1.88	0.003830	193.077 ± 2.05
0.002230	231.727 ± 1.71	0.003830	195.813 ± 2.05
0.002255	230.017 ± 1.54	0.003856	193.932 ± 2.22
0.002271	228.306 ± 1.54	0.003865	196.668 ± 2.39
0.002297	227.280 ± 1.54	0.004214	192.735 ± 2.22

$p_{\text{lab}} = 5.603$ GeV/c, *continued.*

$\lvert t\rvert$ $(\text{GeV/c})^2$	$d\sigma/dt$ $(\text{mb}/(\text{GeV/c})^2)$	$\lvert t\rvert$ $(\text{GeV/c})^2$	$d\sigma/dt$ $(\text{mb}/(\text{GeV/c})^2)$
0.004227	191.709 ± 2.05	0.006800	181.619 ± 1.88
0.004238	190.170 ± 2.22	0.006805	178.883 ± 1.03
0.004245	191.367 ± 2.05	0.006828	177.686 ± 1.88
0.004264	191.025 ± 2.05	0.006832	179.054 ± 1.88
0.004300	192.735 ± 2.39	0.006955	179.054 ± 1.88
0.004635	191.196 ± 2.22	0.006994	179.567 ± 1.88
0.004664	186.921 ± 2.05	0.006999	178.712 ± 1.88
0.004691	193.248 ± 2.05	0.007066	179.054 ± 1.37
0.004712	187.263 ± 1.88	0.007112	178.199 ± 1.20
0.004716	188.460 ± 1.88	0.007132	180.251 ± 1.54
0.004730	187.776 ± 2.05	0.007375	179.225 ± 1.03
0.005147	188.460 ± 2.05	0.007403	176.489 ± 1.20
0.005164	185.039 ± 1.88	0.007429	176.831 ± 1.03
0.005172	187.776 ± 2.05	0.007432	175.462 ± 1.20
0.005173	186.065 ± 1.88	0.007436	178.370 ± 1.20
0.005187	186.749 ± 2.05	0.007482	177.857 ± 1.37
0.005192	187.605 ± 1.88	0.008017	173.752 ± 1.03
0.005640	185.039 ± 2.05	0.008017	174.607 ± 1.03
0.005658	185.552 ± 2.05	0.008025	174.778 ± 1.03
0.005662	183.329 ± 1.88	0.008032	175.633 ± 1.20
0.005702	186.578 ± 1.88	0.008034	176.318 ± 1.37
0.005728	181.961 ± 1.88	0.008061	176.831 ± 1.20
0.005770	182.474 ± 1.88	0.008590	173.239 ± 1.03
0.006208	180.935 ± 1.88	0.008600	175.633 ± 1.20
0.006217	181.790 ± 1.88	0.008612	173.923 ± 1.20
0.006248	179.738 ± 1.88	0.008622	173.239 ± 1.03
0.006260	181.106 ± 2.05	0.008632	173.581 ± 1.03
0.006266	183.671 ± 1.88	0.008709	174.607 ± 1.37
0.006306	179.567 ± 1.88	0.009196	172.726 ± 1.20
0.006557	181.961 ± 1.54	0.009196	170.503 ± 1.03
0.006734	178.712 ± 1.03	0.009217	171.871 ± 1.03
0.006735	178.370 ± 1.20	0.009275	171.187 ± 1.03
0.006740	181.106 ± 1.88	0.009302	170.161 ± 1.03
0.006762	180.935 ± 1.88	0.009305	171.016 ± 1.03
0.006778	181.619 ± 2.05	0.009903	171.529 ± 1.03

$p_{\text{lab}} = 5.603$ GeV/c, *continued.*

$\lvert t\rvert$ $(\text{GeV/c})^2$	$d\sigma/dt$ $(\text{mb}/(\text{GeV/c})^2)$	$\lvert t\rvert$ $(\text{GeV/c})^2$	$d\sigma/dt$ $(\text{mb}/(\text{GeV/c})^2)$
0.009905	168.451 ± 1.03	0.012141	166.912 ± 1.37
0.009922	169.135 ± 1.20	0.012166	164.688 ± 1.03
0.009926	169.306 ± 1.03	0.012545	162.807 ± 1.54
0.009947	167.425 ± 1.03	0.012565	165.372 ± 1.54
0.009972	168.964 ± 1.03	0.012579	167.938 ± 1.71
0.010550	168.793 ± 1.03	0.012887	162.978 ± 1.37
0.010586	167.767 ± 1.03	0.012927	163.662 ± 1.37
0.010620	168.793 ± 1.20	0.012932	163.833 ± 1.37
0.010635	167.767 ± 0.86	0.012936	164.004 ± 1.37
0.010656	166.912 ± 0.86	0.012953	165.715 ± 1.54
0.010744	166.741 ± 1.03	0.013031	161.781 ± 1.54
0.011325	165.372 ± 1.03	0.013691	161.610 ± 1.37
0.011340	167.425 ± 1.03	0.013724	159.558 ± 1.54
0.011352	167.254 ± 1.03	0.013732	161.781 ± 1.37
0.011390	166.057 ± 0.86	0.013739	160.584 ± 1.37
0.011403	165.715 ± 0.86	0.013744	164.859 ± 1.54
0.011444	165.201 ± 0.86	0.013785	162.465 ± 1.37
0.011655	168.964 ± 1.71	0.014487	160.926 ± 1.54
0.012004	166.570 ± 1.37	0.014502	161.781 ± 1.37
0.012045	165.715 ± 1.37	0.014518	160.242 ± 1.37

$p_{\text{lab}} = 5.603$ GeV/c, *continued.*

$\lvert t\rvert$ $(\text{GeV/c})^2$	$d\sigma/dt$ $(\text{mb}/(\text{GeV/c})^2)$	$\lvert t\rvert$ $(\text{GeV/c})^2$	$d\sigma/dt$ $(\text{mb}/(\text{GeV/c})^2)$
0.014533	163.320 ± 1.37	0.017201	154.769 ± 1.20
0.014547	160.413 ± 1.54	0.017238	154.598 ± 1.20
0.015263	160.755 ± 1.71	0.017990	153.743 ± 1.37
0.015289	157.506 ± 1.54	0.018015	152.033 ± 1.20
0.015350	159.045 ± 2.74	0.018048	152.888 ± 1.37
0.015351	158.703 ± 1.37	0.018078	152.717 ± 1.20
0.015370	158.532 ± 1.37	0.018149	153.230 ± 1.20
0.015373	157.506 ± 1.37	0.018181	153.230 ± 1.20
0.016188	157.848 ± 1.88	0.018905	151.691 ± 1.37
0.016195	155.796 ± 1.88	0.018949	150.152 ± 1.20
0.016209	156.993 ± 1.37	0.018963	153.059 ± 1.37
0.016213	155.796 ± 1.88	0.018991	151.007 ± 1.20
0.016238	158.874 ± 1.37	0.019054	153.059 ± 1.20
0.016239	157.164 ± 1.37	0.019060	151.178 ± 1.20
0.017019	155.283 ± 1.37	0.019244	150.494 ± 1.20
0.017036	152.717 ± 1.37	0.019293	150.836 ± 1.20
0.017041	158.190 ± 1.37	0.019304	152.033 ± 1.37
0.017133	154.941 ± 1.20		

Table A.4: Differential cross section results for $p_{\text{lab}} = 5.724$ GeV/c.

$\lvert t\rvert$ $(\text{GeV/c})^2$	$d\sigma/dt$ $(\text{mb}/(\text{GeV/c})^2)$	$\lvert t\rvert$ $(\text{GeV/c})^2$	$d\sigma/dt$ $(\text{mb}/(\text{GeV/c})^2)$
0.000924	480.083 ± 7.96	0.003805	192.169 ± 2.37
0.001095	395.014 ± 6.78	0.003811	195.728 ± 2.20
0.001127	373.323 ± 6.95	0.004166	189.458 ± 2.20
0.001130	388.744 ± 6.44	0.004271	192.338 ± 2.20
0.001327	325.026 ± 2.88	0.004289	190.474 ± 2.03
0.001387	317.062 ± 2.88	0.004520	186.916 ± 2.20
0.001397	314.520 ± 2.54	0.004725	188.102 ± 2.03
0.001530	288.762 ± 2.54	0.004735	191.322 ± 2.20
0.001650	276.730 ± 2.20	0.005088	183.187 ± 2.03
0.001656	272.663 ± 2.54	0.005189	184.543 ± 2.03
0.001867	255.039 ± 2.03	0.005208	186.746 ± 2.03
0.001928	250.294 ± 1.86	0.005582	182.679 ± 2.03
0.001940	248.430 ± 2.03	0.005690	183.018 ± 1.86
0.002171	234.026 ± 1.69	0.005694	185.560 ± 2.20
0.002238	229.111 ± 1.53	0.005972	180.815 ± 2.03
0.002240	232.840 ± 2.20	0.006132	180.646 ± 2.03
0.002416	218.605 ± 1.69	0.006266	181.662 ± 1.86
0.002518	216.741 ± 1.69	0.006283	180.307 ± 1.86
0.002604	216.741 ± 1.53	0.006661	177.256 ± 1.86
0.002615	212.165 ± 1.36	0.006781	178.951 ± 1.86
0.002861	206.912 ± 1.53	0.006798	175.731 ± 1.86
0.002939	204.370 ± 1.36	0.006927	177.595 ± 1.36
0.002951	205.726 ± 1.53	0.007034	177.595 ± 1.86
0.003081	206.404 ± 2.54	0.007039	177.934 ± 2.03
0.003107	203.862 ± 1.53	0.007059	175.562 ± 1.86
0.003110	202.675 ± 1.69	0.007070	177.256 ± 1.19
0.003122	204.031 ± 3.39	0.007172	175.053 ± 1.36
0.003123	200.811 ± 1.53	0.007225	177.765 ± 1.02
0.003242	200.642 ± 2.37	0.007233	176.070 ± 1.19
0.003269	199.117 ± 3.05	0.007450	176.917 ± 1.02
0.003285	198.100 ± 2.20	0.007512	174.714 ± 1.19
0.003423	201.489 ± 2.20	0.007852	174.714 ± 1.19
0.003453	195.558 ± 2.20	0.007939	176.748 ± 1.36
0.003658	193.525 ± 2.71	0.008015	175.392 ± 1.19
0.003747	195.389 ± 2.37	0.008069	172.173 ± 1.36

$p_{\text{lab}} = 5.724$ GeV/c, *continued.*

$\lvert t\rvert$ $(\text{GeV/c})^2$	$d\sigma/dt$ $(\text{mb}/(\text{GeV/c})^2)$	$\lvert t\rvert$ $(\text{GeV/c})^2$	$d\sigma/dt$ $(\text{mb}/(\text{GeV/c})^2)$
0.008568	172.173 ± 1.02	0.013062	160.480 ± 1.53
0.008666	173.359 ± 1.19	0.013498	162.513 ± 1.36
0.008683	172.850 ± 1.02	0.013646	160.649 ± 1.53
0.009047	169.970 ± 1.02	0.013764	163.869 ± 1.53
0.009313	170.986 ± 1.02	0.013850	157.260 ± 1.53
0.009325	171.156 ± 1.19	0.014477	159.632 ± 1.36
0.009837	168.275 ± 1.02	0.014614	159.124 ± 1.53
0.009963	168.444 ± 1.02	0.014644	155.226 ± 1.36
0.010042	168.783 ± 1.02	0.015121	158.955 ± 1.36
0.010521	167.597 ± 1.02	0.015437	158.785 ± 1.36
0.010666	165.733 ± 0.85	0.016174	156.074 ± 2.03
0.010698	167.089 ± 1.36	0.017079	155.904 ± 1.53
0.011140	164.208 ± 1.02	0.017174	154.210 ± 1.19
0.011284	167.089 ± 1.02	0.017223	150.312 ± 1.53
0.011432	165.394 ± 0.85	0.017825	152.176 ± 1.36
0.011437	164.716 ± 0.85	0.018067	154.549 ± 1.36
0.012070	162.683 ± 1.02	0.018181	152.684 ± 1.36
0.012398	163.361 ± 1.53	0.018981	149.634 ± 1.19
0.012454	163.191 ± 1.36	0.019041	150.481 ± 1.19
0.012630	162.344 ± 1.53	0.019466	150.143 ± 1.36
0.012701	162.005 ± 1.36	0.019515	147.431 ± 1.69
0.012724	165.055 ± 1.53	0.019541	148.787 ± 1.19
0.012953	163.869 ± 1.36		

Table A.5: Differential cross section results for $p_{\text{lab}} = 5.941$ GeV/c.

$\lvert t\rvert$ $(\text{GeV/c})^2$	$d\sigma/dt$ $(\text{mb}/(\text{GeV/c})^2)$	$\lvert t\rvert$ $(\text{GeV/c})^2$	$d\sigma/dt$ $(\text{mb}/(\text{GeV/c})^2)$
0.000943	454.705 ± 7.56	0.003043	196.283 ± 1.32
0.000961	445.170 ± 7.23	0.003043	197.598 ± 1.48
0.000968	441.554 ± 7.23	0.003063	195.954 ± 1.32
0.001128	378.263 ± 6.58	0.003066	199.077 ± 1.48
0.001169	360.674 ± 5.92	0.003106	198.584 ± 2.47
0.001174	359.852 ± 5.92	0.003108	195.625 ± 2.14
0.001176	358.372 ± 5.75	0.003111	195.625 ± 2.14
0.001189	349.331 ± 5.59	0.003165	194.146 ± 2.14
0.001394	306.260 ± 2.63	0.003332	192.830 ± 2.14
0.001413	297.876 ± 2.30	0.003426	191.680 ± 2.14
0.001417	297.219 ± 2.47	0.003480	189.707 ± 2.14
0.001432	296.068 ± 2.30	0.003499	194.803 ± 2.30
0.001446	297.547 ± 2.47	0.003517	191.351 ± 1.97
0.001691	262.203 ± 1.97	0.003529	189.378 ± 1.97
0.001695	257.929 ± 1.97	0.003831	191.680 ± 2.30
0.001695	262.697 ± 2.30	0.003902	187.570 ± 2.14
0.001704	262.532 ± 2.14	0.003914	185.433 ± 2.14
0.001709	262.532 ± 2.14	0.003918	187.241 ± 1.97
0.001958	241.819 ± 2.30	0.003932	187.406 ± 1.97
0.001960	238.038 ± 1.64	0.004309	185.268 ± 2.14
0.001978	239.189 ± 1.81	0.004338	186.419 ± 1.97
0.001980	235.572 ± 2.30	0.004343	184.611 ± 1.97
0.001986	235.736 ± 2.30	0.004373	183.460 ± 1.97
0.002273	219.626 ± 1.48	0.004397	185.433 ± 1.97
0.002313	220.284 ± 1.64	0.004816	182.309 ± 1.97
0.002322	217.653 ± 1.81	0.004821	181.981 ± 1.81
0.002328	217.489 ± 1.64	0.004826	182.309 ± 1.97
0.002351	213.215 ± 1.48	0.004840	182.967 ± 1.97
0.002651	206.146 ± 1.48	0.004849	180.337 ± 1.97
0.002670	207.132 ± 1.48	0.005265	182.145 ± 2.14
0.002676	206.968 ± 1.48	0.005267	179.186 ± 1.81
0.002682	205.324 ± 1.32	0.005289	180.830 ± 1.97
0.002697	202.365 ± 1.32	0.005299	180.337 ± 1.97
0.003026	201.379 ± 2.30	0.005309	179.186 ± 2.14
0.003032	195.296 ± 1.32	0.005773	175.569 ± 1.81

$p_{\text{lab}} = 5.941$ GeV/c, *continued.*

$\lvert t\rvert$ $(\text{GeV/c})^2$	$d\sigma/dt$ $(\text{mb}/(\text{GeV/c})^2)$	$\lvert t\rvert$ $(\text{GeV/c})^2$	$d\sigma/dt$ $(\text{mb}/(\text{GeV/c})^2)$
0.005825	180.008 ± 1.81	0.009408	164.555 ± 0.99
0.005853	176.720 ± 1.97	0.009417	165.870 ± 1.15
0.005861	177.707 ± 1.97	0.009447	164.884 ± 0.99
0.005896	174.747 ± 1.81	0.009454	164.062 ± 1.15
0.006367	175.241 ± 1.81	0.009481	164.391 ± 0.99
0.006384	176.391 ± 1.81	0.009971	162.747 ± 0.99
0.006407	177.213 ± 1.81	0.010069	162.418 ± 1.32
0.006417	174.090 ± 1.81	0.010122	163.076 ± 0.99
0.006436	173.597 ± 1.81	0.010151	163.405 ± 0.99
0.006835	174.419 ± 1.15	0.010162	162.418 ± 1.15
0.006952	172.282 ± 1.81	0.010664	160.445 ± 0.99
0.006952	171.788 ± 1.15	0.010850	159.295 ± 0.99
0.006965	172.446 ± 1.81	0.010853	161.925 ± 0.99
0.006968	172.939 ± 1.81	0.010916	160.610 ± 1.15
0.006975	174.090 ± 1.15	0.010936	160.445 ± 0.99
0.006990	174.747 ± 1.81	0.011492	159.459 ± 0.99
0.006990	173.761 ± 1.32	0.011679	160.610 ± 0.99
0.007000	172.282 ± 1.81	0.011681	159.788 ± 0.99
0.007151	171.131 ± 2.30	0.011688	157.980 ± 0.82
0.007236	171.295 ± 0.99	0.011723	158.637 ± 0.99
0.007468	170.145 ± 1.15	0.012230	161.267 ± 1.48
0.007508	171.295 ± 1.15	0.012370	159.788 ± 1.32
0.007529	169.487 ± 0.99	0.012417	158.144 ± 1.32
0.007599	171.788 ± 1.15	0.012452	163.898 ± 1.48
0.007641	169.651 ± 0.99	0.012925	156.829 ± 1.32
0.008066	170.802 ± 1.32	0.013090	159.459 ± 1.32
0.008073	169.158 ± 1.15	0.013193	157.322 ± 1.32
0.008152	168.501 ± 1.15	0.013209	158.473 ± 1.48
0.008220	167.021 ± 0.99	0.013274	157.651 ± 1.32
0.008222	168.172 ± 0.99	0.013285	156.664 ± 1.32
0.008696	166.857 ± 0.99	0.013911	158.473 ± 1.48
0.008741	167.514 ± 1.15	0.014014	154.692 ± 1.32
0.008801	167.514 ± 0.99	0.014042	156.171 ± 1.48
0.008807	166.528 ± 0.99	0.014049	156.171 ± 1.32
0.008813	167.514 ± 1.15	0.014079	155.514 ± 1.48

$p_{\text{lab}} = 5.941$ GeV/c, *continued.*

$\lvert t\rvert$ $(\text{GeV/c})^2$	$d\sigma/dt$ $(\text{mb}/(\text{GeV/c})^2)$	$\lvert t\rvert$ $(\text{GeV/c})^2$	$d\sigma/dt$ $(\text{mb}/(\text{GeV/c})^2)$
0.014751	155.678 ± 1.32	0.017468	150.089 ± 1.32
0.014807	154.856 ± 1.32	0.017540	148.938 ± 1.48
0.014808	155.021 ± 1.32	0.017577	148.938 ± 1.32
0.014874	152.555 ± 1.32	0.017598	146.965 ± 1.15
0.014957	154.527 ± 1.32	0.018456	147.294 ± 1.15
0.015630	151.404 ± 1.48	0.018475	146.801 ± 1.32
0.015684	154.363 ± 1.32	0.018519	148.774 ± 1.32
0.015705	152.062 ± 1.48	0.018549	144.828 ± 1.15
0.015730	152.719 ± 1.32	0.018583	146.801 ± 1.15
0.015760	152.062 ± 1.48	0.019390	144.006 ± 1.15
0.016489	150.418 ± 1.32	0.019427	144.171 ± 1.15
0.016527	149.267 ± 1.32	0.019444	145.157 ± 1.15
0.016552	152.390 ± 1.48	0.019470	145.815 ± 1.15
0.016554	150.746 ± 1.97	0.019507	144.993 ± 1.15
0.016561	152.226 ± 1.32	0.019750	143.349 ± 1.64
0.017460	148.116 ± 1.15		

Table A.6: Differential cross section results for $p_{\text{lab}} = 6.234$ GeV/c.

$\|t\|$ $(\text{GeV/c})^2$	$d\sigma/dt$ $(\text{mb}/(\text{GeV/c})^2)$	$\|t\|$ $(\text{GeV/c})^2$	$d\sigma/dt$ $(\text{mb}/(\text{GeV/c})^2)$
0.000856	421.396 ± 7.37	0.007195	170.867 ± 1.76
0.001065	382.446 ± 6.25	0.007415	167.501 ± 1.12
0.001332	311.279 ± 2.56	0.008010	166.218 ± 0.96
0.001592	265.917 ± 2.40	0.008712	164.936 ± 0.96
0.001857	242.034 ± 1.76	0.009334	162.051 ± 1.12
0.002182	221.357 ± 1.60	0.010004	160.608 ± 0.96
0.002553	206.451 ± 1.44	0.010724	158.204 ± 0.96
0.002910	197.314 ± 1.44	0.011468	157.563 ± 0.96
0.003171	193.948 ± 1.28	0.013046	154.197 ± 1.28
0.003334	190.422 ± 2.89	0.013838	152.594 ± 1.28
0.003737	186.094 ± 2.40	0.014761	151.792 ± 1.44
0.004224	181.446 ± 2.08	0.015656	149.388 ± 1.60
0.004678	177.599 ± 2.08	0.016449	148.106 ± 1.28
0.005125	175.675 ± 1.76	0.017418	145.702 ± 1.28
0.005657	173.912 ± 1.92	0.018425	143.618 ± 1.28
0.006246	170.867 ± 1.76	0.019320	142.656 ± 1.12
0.006799	169.745 ± 1.76	0.020056	142.015 ± 1.12

Appendix B

World Data for σ_T, b, and ρ

Table B.1: World data for the total cross section for $\bar{p}p$ scattering from Refs. [66, 71], [72]–[108].

p_{lab} (GeV/c)	σ_T (mb)	Ref.	p_{lab} (GeV/c)	σ_T (mb)	Ref.
0.181	339.400 ± 30.60	[66]	0.2948	246.24 ± 1.16	[79]
0.219	292.100 ± 23.60	[66]	0.3046	242.78 ± 2.46	[79]
0.2219	317.71 ± 3.03	[79]	0.3055	239.88 ± 1.35	[79]
0.2296	304.67 ± 1.63	[79]	0.306	238.50 ± 19.10	[82]
0.2370	297.12 ± 3.14	[79]	0.3118	236.03 ± 1.18	[79]
0.239	261.200 ± 5.700	[66]	0.3187	234.65 ± 0.51	[79]
0.2499	286.47 ± 3.11	[79]	0.3194	233.65 ± 0.53	[79]
0.2549	279.66 ± 1.25	[79]	0.3268	229.44 ± 1.16	[79]
0.2588	273.95 ± 1.84	[79]	0.3357	226.90 ± 0.75	[79]
0.261	252.400 ± 2.000	[66]	0.334	239.70 ± 6.80	[76]
0.2656	265.22 ± 2.37	[79]	0.336	226.60 ± 9.60	[82]
0.2717	262.94 ± 1.17	[79]	0.3456	222.89 ± 0.94	[79]
0.2733	263.25 ± 1.09	[79]	0.349	224.50 ± 6.60	[83]
0.2803	262.17 ± 1.48	[79]	0.3547	217.55 ± 0.94	[79]
0.2811	260.39 ± 1.55	[79]	0.360	217.40 ± 4.90	[82]
0.287	229.300 ± 2.00	[66]	0.3648	214.94 ± 0.70	[79]
0.2891	251.64 ± 1.18	[79]	0.372	201.30 ± 6.80	[76]
0.2939	247.94 ± 1.19	[79]	0.3752	209.83 ± 1.24	[79]

Total cross section for $\bar{p}p$ scattering, *continued.*

p_{lab} (GeV/c)	σ_T (mb)	Ref.	p_{lab} (GeV/c)	σ_T (mb)	Ref.
0.381	202.30 ± 3.90	[82]	0.510	156.30 ± 2.70	[96]
0.3851	206.37 ± 0.76	[79]	0.514	171.20 ± 2.10	[82]
0.3942	204.38 ± 0.87	[79]	0.517	166.00 ± 8.00	[84]
0.396	197.80 ± 12.40	[96]	0.522	152.50 ± 2.90	[96]
0.399	192.90 ± 3.30	[82]	0.524	167.60 ± 2.00	[82]
0.403	203.10 ± 6.50	[76]	0.524	172.20 ± 4.70	[76]
0.4039	201.38 ± 1.85	[79]	0.525	169.20 ± 4.10	[83]
0.405	199.70 ± 5.50	[83]	0.533	160.90 ± 2.00	[82]
0.408	179.80 ± 4.50	[96]	0.534	152.60 ± 3.00	[96]
0.4132	196.79 ± 0.87	[79]	0.535	163.00 ± 12.00	[86]
0.416	193.20 ± 3.20	[82]	0.539	159.50 ± 3.80	[76]
0.419	183.10 ± 3.20	[96]	0.542	161.40 ± 1.90	[82]
0.420	185.00 ± 13.00	[86]	0.547	151.10 ± 3.20	[96]
0.429	196.60 ± 6.10	[76]	0.551	156.50 ± 2.40	[82]
0.430	177.20 ± 3.00	[96]	0.553	167.60 ± 3.50	[83]
0.431	188.90 ± 2.90	[82]	0.553	165.00 ± 4.70	[76]
0.441	171.10 ± 3.00	[96]	0.559	153.40 ± 3.20	[96]
0.444	188.00 ± 4.90	[83]	0.567	168.00 ± 4.50	[76]
0.445	184.60 ± 0.29	[82]	0.572	147.00 ± 3.20	[96]
0.452	188.90 ± 4.60	[76]	0.575	167.40 ± 7.80	[75]
0.453	167.40 ± 3.00	[96]	0.577	161.10 ± 3.20	[83]
0.458	183.40 ± 0.27	[82]	0.580	161.10 ± 4.30	[76]
0.463	162.80 ± 3.10	[96]	0.585	142.60 ± 3.20	[96]
0.467	179.50 ± 4.50	[83]	0.592	155.80 ± 4.10	[76]
0.471	177.90 ± 0.26	[82]	0.597	144.00 ± 3.30	[96]
0.472	173.10 ± 4.20	[76]	0.599	154.30 ± 3.00	[83]
0.475	161.40 ± 3.10	[96]	0.604	152.90 ± 4.00	[76]
0.482	183.70 ± 2.60	[82]	0.610	138.80 ± 3.30	[96]
0.487	163.60 ± 2.90	[96]	0.624	136.70 ± 4.00	[96]
0.491	172.00 ± 5.00	[76]	0.627	135.00 ± 16.00	[85]
0.493	178.30 ± 2.50	[82]	0.629	156.30 ± 7.30	[75]
0.498	158.70 ± 2.70	[96]	0.638	134.40 ± 5.30	[96]
0.499	171.10 ± 4.50	[83]	0.639	152.00 ± 7.00	[84]
0.504	174.50 ± 2.20	[82]	0.652	130.30 ± 5.90	[96]
0.508	168.00 ± 4.80	[76]	0.664	138.70 ± 5.70	[96]

Total cross section for $\bar{p}p$ scattering, *continued.*

p_{lab} (GeV/c)	σ_T (mb)	Ref.	p_{lab} (GeV/c)	σ_T (mb)	Ref.
0.679	127.50 ± 5.60	[96]	1.650	97.05 ± 0.06	[72]
0.681	144.30 ± 3.70	[75]	1.683	96.17 ± 0.39	[75]
0.694	126.10 ± 5.70	[96]	1.700	96.46 ± 0.06	[72]
0.708	126.80 ± 6.00	[96]	1.750	95.61 ± 0.06	[72]
0.723	126.40 ± 4.60	[96]	1.770	95.32 ± 0.07	[94]
0.733	142.10 ± 3.30	[75]	1.800	94.48 ± 0.06	[72]
0.737	126.20 ± 5.40	[96]	1.830	94.14 ± 0.07	[94]
0.785	132.70 ± 3.00	[75]	1.850	93.71 ± 0.06	[72]
0.837	128.00 ± 2.90	[75]	1.875	93.05 ± 0.06	[72]
0.867	120.70 ± 1.30	[75]	1.880	92.75 ± 0.07	[94]
0.888	116.80 ± 3.30	[75]	1.900	92.52 ± 0.06	[72]
0.972	120.50 ± 0.90	[75]	1.925	92.07 ± 0.06	[72]
1.000	117.42 ± 0.21	[72]	1.950	91.38 ± 0.06	[72]
1.050	114.59 ± 0.17	[72]	1.950	90.33 ± 0.07	[94]
1.074	113.30 ± 0.90	[75]	2.000	90.23 ± 0.04	[72]
1.100	111.64 ± 0.16	[72]	2.050	88.84 ± 0.05	[72]
1.110	112.60 ± 2.00	[95]	2.082	88.48 ± 0.20	[75]
1.150	110.11 ± 0.12	[72]	2.095	88.46 ± 0.06	[72]
1.178	111.60 ± 0.60	[75]	2.150	87.39 ± 0.06	[72]
1.200	108.96 ± 0.11	[72]	2.200	86.81 ± 0.06	[72]
1.250	107.75 ± 0.10	[72]	2.250	85.62 ± 0.06	[72]
1.300	106.47 ± 0.10	[72]	2.285	83.76 ± 0.43	[75]
1.310	109.60 ± 2.00	[95]	2.300	85.00 ± 0.05	[72]
1.330	108.40 ± 3.00	[95]	2.320	84.80 ± 4.00	[74]
1.345	105.50 ± 0.10	[72]	2.350	84.45 ± 0.05	[72]
1.350	106.70 ± 2.00	[95]	2.400	83.66 ± 0.06	[72]
1.380	103.30 ± 0.40	[75]	2.450	83.16 ± 0.06	[72]
1.400	102.78 ± 0.09	[72]	2.500	82.32 ± 0.04	[72]
1.450	101.12 ± 0.08	[72]	2.550	81.64 ± 0.05	[72]
1.490	100.26 ± 0.06	[72]	2.600	81.12 ± 0.05	[72]
1.520	99.70 ± 1.50	[95]	2.650	80.61 ± 0.05	[72]
1.550	98.82 ± 0.06	[72]	2.686	79.33 ± 0.25	[75]
1.600	97.81 ± 0.06	[72]	2.70	79.90 ± 0.05	[72]
1.630	97.57 ± 0.07	[94]			

Total cross section for $\bar{p}p$ scattering, *continued.*

p_{lab} (GeV/c)	σ_T (mb)	Ref.	p_{lab} (GeV/c)	σ_T (mb)	Ref.
2.750	79.47 ± 0.05	[72]	5.900	63.60 ± 2.60	[103]
2.800	78.91 ± 0.05	[72]	**5.941**	**59.1 ± 0.5**	
2.850	78.21 ± 0.05	[72]	6.000	59.30 ± 1.10	[102]
2.886	77.82 ± 0.28	[75]	6.000	60.60 ± 2.20	[105]
2.900	77.79 ± 0.05	[72]	**6.234**	**61.5 ± 1.2**	
2.950	77.23 ± 0.05	[72]	6.650	59.50 ± 0.50	[104]
3.000	76.68 ± 0.05	[72]	6.900	60.30 ± 1.50	[103]
3.050	76.29 ± 0.05	[72]	6.90	63.10 ± 2.90	[100]
3.068	75.24 ± 0.70	[75]	6.94	58.70 ± 2.80	[92]
3.100	75.66 ± 0.05	[72]	7.00	63.00 ± 2.50	[105]
3.150	75.16 ± 0.05	[72]	7.30	58.30 ± 1.30	[97]
3.200	74.66 ± 0.05	[72]	8.00	56.40 ± 0.80	[102]
3.240	72.90 ± 1.00	[75]	8.00	60.30 ± 3.00	[103]
3.250	74.20 ± 0.05	[72]	9.10	57.51 ± 0.73	[93]
3.280	75.40 ± 2.00	[91]	9.30	59.50 ± 1.80	[103]
3.300	73.67 ± 0.05	[72]	10.00	54.70 ± 0.60	[89]
3.540	69.70 ± 0.50	[75]	10.00	56.00 ± 3.30	[103]
3.600	76.30 ± 1.80	[90]	10.20	52.60 ± 2.70	[105]
3.600	76.20 ± 1.80	[88]	10.70	53.00 ± 1.00	[105]
3.660	71.70 ± 2.00	[91]	11.30	54.70 ± 3.70	[103]
3.702	**71.9 ± 0.9**		12.00	51.70 ± 0.80	[93]
3.860	67.70 ± 0.90	[75]	12.30	53.90 ± 3.40	[103]
4.000	65.10 ± 3.10	[103]	13.30	51.70 ± 4.40	[103]
4.000	71.00 ± 1.00	[87]	13.30	51.40 ± 0.50	[89]
4.015	66.84 ± 0.32	[75]	14.00	50.70 ± 0.90	[93]
4.066	**67.8 ± 1.5**		14.20	52.70 ± 3.70	[103]
4.300	60.60 ± 0.80	[75]	15.00	51.00 ± 0.70	[89]
4.600	68.80 ± 0.80	[90]	16.00	49.20 ± 0.80	[93]
4.700	65.80 ± 0.90	[75]	16.40	49.30 ± 3.30	[103]
5.000	62.70 ± 4.20	[103]	17.40	51.70 ± 4.30	[103]
5.000	67.00 ± 2.50	[105]	18.00	50.30 ± 3.60	[93]
5.350	57.90 ± 2.60	[75]	18.30	50.30 ± 4.30	[103]
5.603	**60.9 ± 0.5**		20.00	48.20 ± 0.40	[89]
5.700	63.60 ± 1.40	[99]	20.00	49.00 ± 1.10	[73]
5.724	**59.5 ± 0.6**		20.30	46.60 ± 7.40	[103]

Total cross section for $\bar{p}p$ scattering, *continued.*

p_{lab} (GeV/c)	σ_T (mb)	Ref.	p_{lab} (GeV/c)	σ_T (mb)	Ref.
23.00	47.40 ± 0.30	[104]	50.000	43.86 ± 0.22	[101]
25.00	47.00 ± 0.30	[89]	70.000	43.05 ± 0.06	[106]
25.00	46.10 ± 0.60	[73]	70.000	43.00 ± 0.22	[101]
27.50	46.30 ± 0.30	[104]	100.000	42.12 ± 0.08	[106]
30.00	45.60 ± 0.30	[89]	100.000	42.04 ± 0.09	[80]
30.00	47.10 ± 0.60	[73]	100.000	42.04 ± 0.21	[101]
31.00	46.10 ± 0.30	[104]	101.50	42.33 ± 0.14	[77]
33.50	45.60 ± 0.30	[104]	120.00	41.70 ± 0.15	[106]
35.000	44.60 ± 0.30	[104]	140.00	41.80 ± 0.21	[101]
35.000	45.30 ± 0.40	[89]	150.00	41.79 ± 0.17	[106]
35.000	45.50 ± 0.70	[73]	150.00	41.72 ± 0.18	[80]
35.000	45.46 ± 0.10	[106]	170.00	41.69 ± 0.15	[106]
37.500	44.70 ± 0.30	[104]	175.00	41.60 ± 0.21	[101]
40.000	45.00 ± 0.40	[89]	200.00	41.51 ± 0.15	[107]
40.000	45.00 ± 0.70	[73]	240.00	41.90 ± 0.20	[107]
40.000	44.00 ± 0.30	[104]	280.00	41.91 ± 0.21	[107]
42.500	44.50 ± 0.30	[104]	511.17	42.80 ± 0.35	[108]
45.000	44.40 ± 0.70	[89]	1484.67	44.70 ± 0.45	[108]
45.000	44.90 ± 0.70	[73]	2114.10	45.00 ± 0.40	[108]
47.500	44.10 ± 0.30	[104]	155391.09	63.30 ± 1.50	[78]
50.000	43.10 ± 0.80	[89]	554000.00	61.10 ± 5.70	[98]
50.000	43.60 ± 0.80	[73]	1726577.00	80.03 ± 2.24	[81]
50.000	43.93 ± 0.10	[106]	1726577.00	72.8 ± 3.1	[71]
50.000	43.86 ± 0.11	[80]			

The above data for $\sigma_T(\bar{p}p)$ have been fitted by various authors with different functions. The most common functional form is that used by the Review of Particle Properties [17]

$$\sigma_T(p) = A + Bp^n + Cln^2(p) + Dln(p)\,, \tag{B.1}$$

with the last two terms included to take account of the slow rise of σ_T at $p \geq$ 100 GeV/c. We find that the data below 50 GeV/c can be best fitted by neglecting these two terms altogether. We have fitted the data in three different energy regions, 2-50 GeV/c, 2-25 GeV/c, and 2-12 GeV/c in the following manner.

All existing data were used with their stated errors, which in most cases are only statistical. It was found that the 1970 data of Abrams et al [72] for p = 1.0-3.3 GeV/c present a special problem. In the range 2.2-3.3 GeV/c the quoted statistical errors for these data are extremely small, $\sim 0.06\%$, and it is stated that "...no great effort was made to obtain an absolute cross-section uncertainty to better than about $\pm 1\%$." Since the statistical errors of Ref. [72] are 15-50 times smaller than the errors for the data from all other sources, if only these errors are used, the data of Ref. [72] completely determine the fit in our region of interest, given the functional form. We have therefore arbitrarily raised the errors on the data of Ref. [72] by a factor four, i.e. to 0.25%. Further, to account for the present value of the density of liquid hydrogen, we have reduced their cross sections by 1.13%. With these changes we obtain the best fit results listed in Table B.2.

Table B.2: Fitted parameters in the parametrization of Eq. B.1 and fitted values of the total cross section. Results are given for three different ranges of data included in the fit.

Fit Range	Fitted Parameters				Fitted σ_T (mb)	
(GeV/c)	A	B	n	χ^2/df	3.5 GeV/c	6.2 GeV/c
$2-50$	40.18(11)	85.96(33)	$-0.797(6)$	2.64	71.85(47)	60.26(42)
$2-25$	40.66(34)	85.96(35)	$-0.810(10)$	2.97	71.82(91)	60.27(86)
$2-12$	41.40(97)	85.69(51)	$-0.826(23)$	3.61	71.85(2.51)	60.39(239)

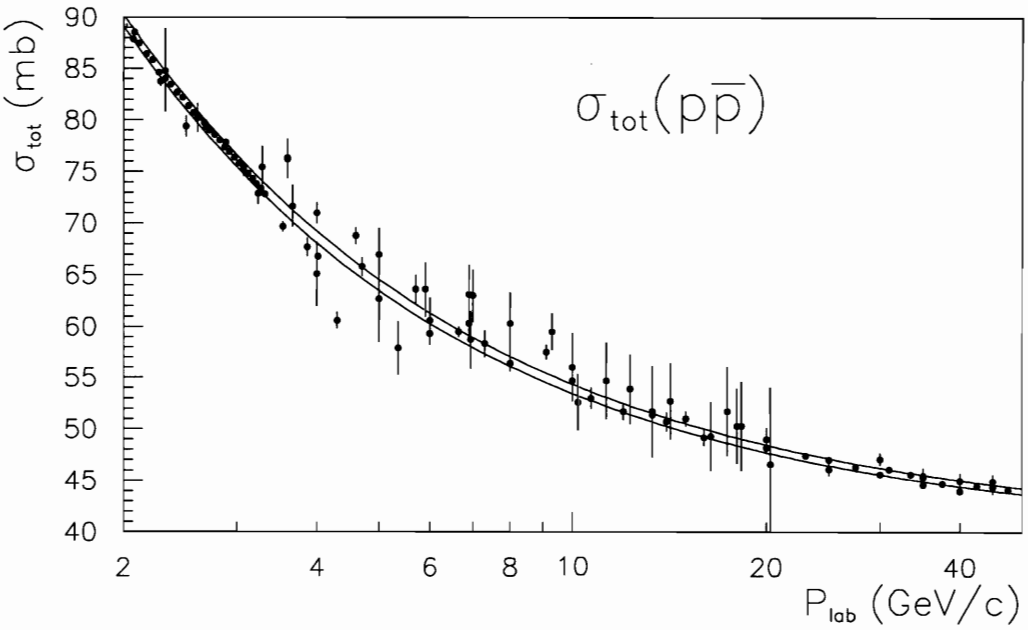

Figure B.1: World data on $\bar{p}p$ total cross sections in the $2 - 50$ GeV/c momentum range (see Table B.1). The curves are the $\pm 2\sigma$ bounds for the fit described in the text.

Total cross section for pp scattering, *continued.*

p_{lab} (GeV/c)	σ_T (mb)	Ref.	p_{lab} (GeV/c)	σ_T (mb)	Ref.
1.289	43.23 ± 0.11	[122]	2.027	49.40 ± 1.60	[124]
1.290	41.00 ± 2.00	[143]	2.050	45.30 ± 1.12	[140]
1.291	36.60 ± 0.50	[128]	2.079	47.22 ± 0.04	[122]
1.294	41.40 ± 0.60	[147]	2.212	46.99 ± 0.05	[122]
1.391	44.40 ± 2.80	[124]	2.240	47.20 ± 2.60	[124]
1.400	46.90 ± 1.00	[139]	2.280	46.67 ± 0.04	[122]
1.408	46.49 ± 0.05	[122]	2.419	46.13 ± 0.04	[122]
1.420	46.20 ± 0.50	[140]	2.450	45.83 ± 0.04	[122]
1.460	47.50 ± 2.20	[139]	2.470	45.10 ± 0.83	[140]
1.463	47.00 ± 2.00	[148]	2.592	45.53 ± 0.04	[122]
1.475	45.00 ± 6.00	[144]	2.680	45.33 ± 0.04	[122]
1.499	47.80 ± 1.60	[124]	2.704	45.17 ± 0.04	[122]
1.522	47.60 ± 1.60	[124]	2.784	41.40 ± 3.20	[124]
1.592	46.10 ± 0.50	[138]	2.819	45.01 ± 0.04	[122]
1.600	47.50 ± 1.02	[140]	2.857	44.93 ± 0.04	[122]
1.607	47.48 ± 0.06	[122]	2.958	44.65 ± 0.04	[122]
1.628	49.00 ± 5.00	[130]	2.970	44.50 ± 0.46	[140]
1.660	47.55 ± 0.06	[122]	2.994	44.47 ± 0.04	[122]
1.696	48.00 ± 2.00	[148]	3.000	44.32 ± 0.06	[145]
1.696	47.40 ± 3.00	[136]	3.054	44.40 ± 0.04	[122]
1.730	46.20 ± 0.82	[140]	3.110	44.19 ± 0.04	[122]
1.780	47.49 ± 0.05	[122]	3.131	44.16 ± 0.04	[122]
1.781	48.30 ± 1.60	[124]	3.142	44.11 ± 0.04	[122]
1.858	47.46 ± 0.04	[122]	3.270	47.10 ± 0.90	[127]
1.890	46.80 ± 1.51	[140]	3.277	43.61 ± 0.04	[122]
1.940	47.36 ± 0.05	[122]	3.303	43.67 ± 0.04	[122]
1.952	47.41 ± 0.04	[122]	3.412	41.60 ± 4.00	[124]
2.005	47.50 ± 1.60	[124]	3.444	43.14 ± 0.04	[122]

Table B.3: World data for the total cross section for pp scattering from Refs. [54]–[56], [101]–[108], [109]–[149].

p_{lab} (GeV/c)	σ_T (mb)	Ref.	p_{lab} (GeV/c)	σ_T (mb)	Ref.
0.140	314.00 ± 13.00	[115]	0.937	25.50 ± 0.23	[146]
0.190	155.00 ± 2.00	[115]	0.963	26.15 ± 0.23	[146]
0.240	92.00 ± 1.00	[115]	0.966	24.00 ± 1.00	[141]
0.280	70.00 ± 1.00	[115]	0.968	26.50 ± 1.40	[124]
0.310	52.80 ± 6.00	[115]	0.968	26.90 ± 0.70	[128]
0.350	42.50 ± 0.40	[115]	0.970	24.00 ± 1.00	[128]
0.370	37.40 ± 2.30	[115]	0.971	26.90 ± 0.70	[128]
0.390	33.90 ± 2.00	[115]	0.981	23.90 ± 1.10	[142]
0.430	28.50 ± 1.30	[115]	0.995	24.30 ± 1.30	[142]
0.440	27.70 ± 1.30	[115]	1.005	23.80 ± 1.20	[149]
0.490	24.80 ± 0.80	[115]	1.009	27.60 ± 0.23	[146]
0.539	20.20 ± 0.70	[142]	1.010	27.00 ± 2.00	[148]
0.540	25.20 ± 1.20	[115]	1.037	28.00 ± 2.00	[143]
0.570	26.10 ± 1.00	[115]	1.075	27.60 ± 0.40	[128]
0.590	23.20 ± 1.90	[115]	1.090	29.90 ± 0.40	[128]
0.607	24.40 ± 0.24	[146]	1.093	30.75 ± 0.26	[146]
0.658	25.80 ± 2.00	[123]	1.108	31.45 ± 0.27	[146]
0.690	22.40 ± 0.90	[115]	1.111	34.03 ± 0.17	[122]
0.720	22.40 ± 1.80	[115]	1.127	30.00 ± 7.00	[130]
0.750	22.60 ± 1.30	[115]	1.136	29.80 ± 1.30	[124]
0.757	23.70 ± 0.21	[146]	1.142	32.10 ± 0.50	[128]
0.763	23.10 ± 2.10	[142]	1.162	34.30 ± 0.33	[146]
0.830	24.30 ± 1.00	[115]	1.194	35.60 ± 0.50	[128]
0.831	24.30 ± 1.00	[123]	1.207	36.00 ± 3.00	[148]
0.850	23.40 ± 0.90	[115]	1.238	37.70 ± 1.40	[124]
0.872	24.30 ± 0.22	[146]	1.244	38.60 ± 0.50	[128]
0.880	23.20 ± 0.30	[115]	1.269	39.80 ± 0.60	[128]
0.930	24.40 ± 0.40	[115]	1.282	41.80 ± 1.10	[134]

Total cross section for pp scattering, *continued.*

p_{lab} (GeV/c)	σ_T (mb)	Ref.	p_{lab} (GeV/c)	σ_T (mb)	Ref.
3.546	42.98 ± 0.04	[122]	9.90	39.40 ± 1.50	[113]
3.580	43.20 ± 0.43	[140]	10.00	39.90 ± 0.60	[102]
3.670	42.10 ± 1.20	[135]	10.00	41.10 ± 1.70	[110]
3.731	42.68 ± 0.04	[122]	10.00	40.20 ± 0.30	[118]
3.908	42.32 ± 0.04	[122]	11.90	39.62 ± 0.12	[56]
4.000	41.60 ± 0.62	[140]	12.00	39.40 ± 0.60	[102]
4.000	43.00 ± 1.50	[125]	12.00	39.60 ± 0.10	[119]
4.037	42.14 ± 0.04	[122]	12.40	39.00 ± 1.50	[113]
4.265	41.76 ± 0.04	[122]	14.00	39.10 ± 0.60	[102]
4.510	42.10 ± 0.70	[127]	14.01	39.42 ± 0.12	[56]
4.552	41.46 ± 0.04	[122]	15.00	39.50 ± 1.00	[103]
4.783	41.38 ± 0.04	[122]	15.00	39.29 ± 0.12	[104]
4.966	41.17 ± 0.04	[122]	15.80	38.70 ± 1.50	[113]
5.000	43.70 ± 0.70	[105]	16.00	38.70 ± 0.60	[102]
5.221	41.17 ± 0.03	[122]	16.03	39.23 ± 0.12	[56]
5.500	41.60 ± 1.40	[109]	17.70	39.70 ± 1.50	[113]
5.526	40.88 ± 0.04	[122]	17.91	39.18 ± 0.12	[56]
5.824	40.85 ± 0.04	[122]	18.00	38.70 ± 0.60	[102]
5.830	41.60 ± 0.60	[127]	19.33	38.90 ± 0.30	[54]
6.000	40.60 ± 0.60	[102]	19.40	39.70 ± 1.50	[113]
7.000	43.30 ± 0.40	[105]	20.00	38.40 ± 0.60	[102]
7.750	41.60 ± 1.10	[127]	20.00	39.06 ± 0.12	[104]
7.820	40.34 ± 0.12	[56]	20.22	39.05 ± 0.12	[56]
7.835	40.08 ± 0.05	[122]	20.46	39.09 ± 0.12	[56]
7.850	40.00 ± 0.60	[55]	21.40	39.40 ± 1.50	[113]
8.000	40.00 ± 0.60	[102]	22.00	38.30 ± 0.60	[102]
8.100	40.10 ± 0.20	[133]	22.00	38.88 ± 0.12	[56]
9.800	39.84 ± 0.12	[56]	23.00	39.39 ± 0.42	[106]

Total cross section for pp scattering, *continued.*

p_{lab} (GeV/c)	σ_T (mb)	Ref.	p_{lab} (GeV/c)	σ_T (mb)	Ref.
24.000	38.90 ± 0.10	[119]	120.00	38.58 ± 0.04	[106]
24.200	38.70 ± 1.50	[113]	122.00	37.00 ± 1.10	[117]
24.500	39.30 ± 0.80	[120]	140.00	38.57 ± 0.19	[101]
25.000	38.80 ± 0.12	[104]	147.00	37.60 ± 1.10	[117]
26.000	38.90 ± 0.12	[56]	150.00	38.69 ± 0.04	[106]
26.420	38.80 ± 0.30	[54]	170.00	38.83 ± 0.04	[106]
28.400	39.90 ± 1.50	[113]	172.00	37.40 ± 1.10	[117]
30.000	38.59 ± 0.12	[104]	175.00	38.76 ± 0.19	[101]
32.000	38.40 ± 0.60	[137]	196.00	38.50 ± 1.20	[117]
35.000	38.49 ± 0.12	[104]	200.00	38.98 ± 0.04	[107]
35.000	38.46 ± 0.05	[106]	205.00	39.00 ± 1.00	[116]
40.000	38.50 ± 0.12	[104]	240.00	39.24 ± 0.04	[107]
45.000	38.45 ± 0.12	[104]	280.00	39.42 ± 0.04	[107]
48.000	38.50 ± 0.10	[117]	293.35	38.89 ± 0.21	[111]
50.000	38.46 ± 0.12	[104]	293.35	39.10 ± 0.30	[114]
50.000	37.74 ± 1.18	[112]	293.35	39.40 ± 0.30	[131]
50.000	38.20 ± 0.05	[106]	295.86	38.70 ± 0.70	[129]
50.000	38.14 ± 0.19	[101]	300.00	40.68 ± 0.55	[132]
55.000	38.43 ± 0.12	[104]	303.00	39.00 ± 1.00	[126]
60.000	38.44 ± 0.12	[104]	310.00	39.59 ± 0.06	[107]
69.000	36.68 ± 0.53	[112]	340.00	39.69 ± 0.07	[107]
70.000	38.28 ± 0.04	[106]	370.00	39.77 ± 0.06	[107]
70.000	38.24 ± 0.19	[101]	405.00	40.60 ± 1.20	[121]
73.000	37.60 ± 1.10	[117]	511.17	40.22 ± 0.22	[108]
98.000	37.60 ± 1.10	[117]	659.33	40.40 ± 0.50	[114]
100.000	38.46 ± 0.04	[106]	1073.37	41.90 ± 0.30	[114]
100.000	38.39 ± 0.19	[101]	1495.95	43.00 ± 0.27	[108]
102.000	38.90 ± 0.80	[121]	2114.10	43.71 ± 0.29	[108]
102.00	38.90 ± 0.80	[121]			

Table B.4: Nuclear slope parameter b for pp elastic scattering from Refs. [159]–[162], [54, 46, 101, 114, 61, 62, 58].

p_{lab} (GeV/c)	b (GeV/c)$^{-2}$	Ref.	p_{lab} (GeV/c)	b (GeV/c)$^{-2}$	Ref.
7.0	9.4 ± 0.6	[58]	175.0	11.52 ± 0.11	[46]
9.0	8.72 ± 0.38	[46]	199.0	11.56 ± 0.12	[46]
10.0	9.2 ± 0.4	[58]	239.0	11.61 ± 0.19	[46]
10.11	10.4 ± 0.4	[54]	245.0	11.57 ± 0.3	[162]
12.0	9.03 ± 0.3	[46]	270.0	11.69 ± 0.1	[46]
19.33	10.0 ± 0.2	[54]	312.0	11.90 ± 0.28	[46]
26.42	10.2 ± 0.2	[54]	348.0	11.96 ± 0.15	[46]
30.0	10.86 ± 0.28	[160]	371.0	11.87 ± 0.15	[46]
50.0	10.3 ± 0.1	[101]	396.0	11.77 ± 0.1	[46]
50.0	10.7 ± 0.18	[46]	494.0	12.0 ± 0.2	[161]
50.0	11.17 ± 0.3	[160]	504.9	11.87 ± 0.28	[162]
58.0	10.83 ± 0.07	[46]	505.2	13.0 ± 0.7	[159]
70.0	10.6 ± 0.2	[101]	1072.0	12.87 ± 0.2	[162]
70.0	11.05 ± 0.43	[160]	1073.0	13.3 ± 0.3	[114]
78.0	10.84 ± 0.2	[46]	1081.0	12.9 ± 0.4	[159]
100.0	10.7 ± 0.2	[101]	1485.0	12.85 ± 0.12	[61]
102.0	11.24 ± 0.13	[46]	1485.0	13.1 ± 0.2	[114]
128.0	11.3 ± 0.2	[46]	1495.0	12.4 ± 0.3	[159]
140.0	11.3 ± 0.1	[101]	1502.0	13.0 ± 0.3	[159]
150.0	11.57 ± 0.23	[46]	2081.0	13.0 ± 0.3	[62]
175.0	11.3 ± 0.1	[101]	2081.0	12.8 ± 0.2	[114]

Table B.5: Nuclear slope parameter b for $\bar{p}p$ elastic scattering from Refs. [57]–[62], [65]–[71], [98]–[100], [150]–[158].

p_{lab} (GeV/c)	b (GeV/c)$^{-2}$	Ref.	p_{lab} (GeV/c)	b (GeV/c)$^{-2}$	Ref.
0.233	71.50 ± 4.50	[65]	0.353	33.50 ± 1.20	[68]
0.272	47.70 ± 2.70	[65]	0.406	28.80 ± 1.20	[68]
0.590	22.80 ± 0.94	[66]	0.446	26.80 ± 1.20	[68]
0.505	26.40 ± 1.14	[66]	0.479	23.80 ± 1.20	[68]
0.287	32.30 ± 1.70	[66]	0.508	25.20 ± 1.10	[68]
0.261	39.20 ± 2.00	[66]	0.533	23.30 ± 1.10	[68]
0.239	52.40 ± 3.80	[66]	0.556	21.00 ± 1.10	[68]
0.219	61.20 ± 16.50	[66]	0.578	22.20 ± 1.10	[68]
0.181	83.70 ± 24.00	[66]	0.550	20.90 ± 2.10	[69]
0.359	56.78 ± 5.50	[67]	0.700	15.00 ± 1.80	[158]
0.402	36.57 ± 1.70	[67]	0.757	18.00 ± 0.50	[69]
0.431	29.90 ± 1.30	[67]	1.077	15.20 ± 0.30	[69]
0.449	30.36 ± 1.20	[67]	1.170	14.90 ± 0.60	[57]
0.475	27.41 ± 1.10	[67]	1.410	14.20 ± 0.30	[57]
0.499	24.33 ± 0.90	[67]	1.780	13.20 ± 0.30	[57]
0.523	24.23 ± 0.80	[67]	2.610	13.10 ± 0.40	[57]
0.546	23.61 ± 0.80	[67]	2.700	13.32 ± 0.18	[154]
0.597	21.83 ± 0.80	[67]	3.000	12.20 ± 0.80	[150]
0.625	21.57 ± 0.80	[67]	3.280	12.80 ± 0.80	[155]
0.652	23.36 ± 0.90	[67]			

Nuclear slope parameter b for $\bar{p}p$ elastic scattering, *continued.*
The entries in bold type refer to results from the present experient.

p_{lab} (GeV/c)	b (GeV/c)$^{-2}$	Ref.	p_{lab} (GeV/c)	b (GeV/c)$^{-2}$	Ref.
3.650	12.10 ± 1.00	[150]	10.000	11.80 ± 2.90	[156]
3.702	**12.9 ± 0.4**		11.800	12.33 ± 0.79	[157]
4.000	13.00 ± 0.60	[155]	12.000	12.66 ± 0.29	[156]
4.066	**12.8 ± 0.7**		15.900	8.78 ± 1.00	[157]
4.200	12.70 ± 1.00	[57]	16.000	11.44 ± 0.20	[152]
5.603	**12.5 ± 0.3**		25.200	12.80 ± 0.40	[151]
5.700	12.60 ± 0.20	[153]	40.100	12.20 ± 0.70	[151]
5.700	12.00 ± 0.40	[99]	50.000	12.60 ± 0.20	[101]
5.724	**12.2 ± 0.4**		70.000	12.80 ± 0.30	[101]
5.941	**12.6 ± 0.3**		100.000	11.90 ± 0.50	[101]
6.000	12.40 ± 1.50	[150]	140.000	12.60 ± 0.40	[101]
6.000	13.50 ± 0.90	[58]	175.000	13.10 ± 0.40	[101]
6.234	**12.2 ± 0.6**		200.000	13.27 ± 0.24	[59]
6.900	14.30 ± 1.50	[100]	314.000	12.30 ± 0.50	[60]
7.200	13.15 ± 0.50	[156]	2100.00	13.10 ± 0.60	[61]
8.000	13.00 ± 0.50	[58]	1500.00	13.36 ± 0.53	[62]
8.000	12.57 ± 0.20	[152]	156000.00	15.50 ± 0.10	[70]
8.900	12.84 ± 0.21	[156]	554000.000	16.20 ± 0.50	[98]
10.000	12.20 ± 0.10	[58]	1700000.000	16.99 ± 0.47	[71]

Table B.6: World data for the ρ-parameter for pp elastic scattering from Refs. [44]–[62].

p_{lab} (GeV/c)	ρ_{pp}	Ref.	p_{lab} (GeV/c)	ρ_{pp}	Ref.
1.110	0.320 ± 0.070	[53]	55.330	−.154± 0.022	[47]
1.280	0.290 ± 0.070	[53]	59.430	−.122± 0.020	[47]
1.340	0.370 ± 0.090	[53]	69.830	−.092± 0.011	[47]
1.400	0.100 ± 0.080	[53]	70.000	−.115± 0.015	[59]
1.700	−.100± 0.080	[53]	80.000	−.096± 0.010	[50]
1.700	−.007± 0.070	[48]	94.500	−.098± 0.012	[46]
2.000	−.170± 0.080	[51]	100.000	−.074± 0.018	[59]
4.200	−.390± 0.030	[58]	125.000	−.024± 0.014	[59]
7.000	−.400± 0.030	[58]	145.000	−.064± 0.010	[46]
7.810	−.331± 0.014	[56]	150.000	0.008 ± 0.012	[59]
7.850	−.290± 0.030	[55]	174.600	−.039± 0.012	[46]
7.920	−.247± 0.023	[49]	175.000	−.011± 0.019	[59]
9.390	−.351± 0.048	[47]	185.400	−.038± 0.014	[46]
9.860	−.345± 0.018	[56]	199.000	−.034± 0.009	[50]
9.940	−.302± 0.018	[49]	200.000	0.019 ± 0.016	[59]
10.000	−.310± 0.040	[58]	215.500	−.020± 0.012	[46]
10.000	−.250± 0.070	[51]	244.100	−.013± 0.010	[46]
10.110	−.430± 0.043	[54]	261.000	−.009± 0.009	[50]
11.940	−.290± 0.013	[56]	269.200	0.022 ± 0.015	[46]
12.140	−.258± 0.016	[49]	290.000	0.020 ± 0.050	[44]
14.030	−.272± 0.013	[56]	303.000	−.011± 0.008	[50]
17.820	−.307± 0.016	[49]	314.000	0.009 ± 0.010	[60]
19.070	−.258± 0.020	[47]	348.700	0.025 ± 0.015	[46]
19.330	−.330± 0.033	[54]	393.000	0.039 ± 0.012	[46]
20.240	−.205± 0.013	[56]	398.000	0.012 ± 0.009	[50]
24.000	−.190± 0.090	[52]	498.000	0.042 ± 0.011	[45]
24.120	−.157± 0.018	[56]	500.000	0.030 ± 0.060	[44]
26.120	−.154± 0.025	[56]	501.000	0.029 ± 0.010	[61]
26.420	−.320± 0.033	[54]	1064.000	0.062 ± 0.011	[45]
38.030	−.171± 0.029	[47]	1485.000	0.060 ± 0.006	[62]
40.030	−.168± 0.015	[47]	1490.000	0.078 ± 0.010	[45]
50.630	−.159± 0.030	[47]	2074.000	0.095 ± 0.011	[45]
51.500	−.157± 0.012	[46]	2081.000	0.080 ± 0.020	[61]
52.000	−.153± 0.012	[50]			

Table B.7: World data for the ρ-parameter for $\bar{p}p$ elastic scattering from Refs. [56]–[61], [63]–[71]. The entries in bold type refer to results from the present experiment.

p_{lab} (GeV/c)	$\rho_{\bar{p}p}$	Ref.	p_{lab} (GeV/c)	$\rho_{\bar{p}p}$	Ref.
0.181	0.100 ± 0.084	[66]	0.625	0.083 ± 0.034	[67]
0.219	0.093 ± 0.098	[66]	0.652	0.197 ± 0.026	[67]
0.233	0.041 ± 0.026	[65]	0.687	0.390 ± 0.060	[63]
0.239	−.028± 0.032	[66]	0.700	0.260 ± 0.050	[64]
0.261	−.142± 0.026	[66]	0.757	0.102 ± 0.043	[69]
0.272	−.014± 0.033	[65]	1.077	0.059 ± 0.035	[69]
0.287	−.103± 0.018	[66]	1.174	0.220 ± 0.040	[57]
0.354	−.220± 0.070	[68]	1.412	0.240 ± 0.040	[57]
0.359	0.023 ± 0.042	[67]	1.776	0.140 ± 0.040	[57]
0.402	−.024± 0.037	[67]	2.607	0.040 ± 0.060	[57]
0.406	−.090± 0.070	[68]	**3.702**	**0.006 ± 0.008**	
0.430	0.080 ± 0.050	[63]	**4.066**	**−0.007 ± 0.012**	
0.431	0.030 ± 0.027	[67]	4.200	0.050 ± 0.040	[58]
0.446	−.070± 0.070	[68]	**5.603**	**−0.030 ± 0.007**	
0.449	0.015 ± 0.029	[67]	**5.724**	**−0.018 ± 0.008**	
0.475	0.097 ± 0.023	[67]	**5.941**	**−0.035 ± 0.008**	
0.475	0.150 ± 0.050	[63]	6.000	0.040 ± 0.060	[58]
0.479	−.050± 0.070	[68]	**6.234**	**−0.029 ± 0.010**	
0.499	0.046 ± 0.028	[67]	8.000	−.140± 0.070	[58]
0.505	−.046± 0.119	[66]	10.000	−.100± 0.050	[58]
0.508	0.010 ± 0.080	[68]	11.900	−.006± 0.034	[56]
0.522	0.200 ± 0.040	[63]	70.000	0.010 ± 0.018	[59]
0.523	0.090 ± 0.023	[67]	125.000	0.012 ± 0.020	[59]
0.534	0.150 ± 0.080	[68]	150.000	−.001± 0.028	[59]
0.546	0.061 ± 0.027	[67]	175.000	0.067 ± 0.039	[59]
0.550	0.084 ± 0.051	[69]	200.000	0.029 ± 0.030	[59]
0.557	0.100 ± 0.080	[68]	314.000	0.048 ± 0.011	[60]
0.572	0.240 ± 0.050	[63]	501.000	0.065 ± 0.025	[61]
0.578	0.040 ± 0.070	[68]	1485.000	0.101 ± 0.018	[61]
0.590	0.203 ± 0.110	[66]	2081.000	0.120 ± 0.030	[61]
0.597	0.119 ± 0.026	[67]	156000.000	0.135 ± 0.015	[70]
0.624	0.450 ± 0.050	[63]	1730000.000	0.140 ± 0.069	[71]

Bibliography

[1] P. Soding, *Phys. Lett.* **8**, 285 (1964).

[2] P. Kroll and W. Schweiger, *Nucl. Phys.* **A503** 865 (1989).

[3] M. M. Block et al., *NUHEP Report* **389** Northwestern University (1994), to be published in *Proc. XXIV Int. Symp. on Multiparticle Dynamics*, edited by A. Giovannini et al. (World Scientific, Singapore).

[4] M. L. Goldberger, Y. Nambu and R. Oehme, *Ann. Phys.* **2** 226 (1957).

[5] C. Bourrely and J. Fischer, *Nucl. Phys.* **B61** 513 (1973).

[6] M. M. Block and R. N. Cahn, *Rev. Mod. Phys.* **57** 563 (1985).

[7] Y. K. Akimov et al., *Sov. Phys. JETP* **21** 507 (1965).

[8] A. C. Melissinos and S. L. Olsen, *Phys. Rpts.* **17** 77 (1975).

[9] P.N. Kirk et al., *Phys. Rev.* **D8**, 63 (1973).

[10] Russ et al., *Phys. Rev.* **D15** 3139 (1977).

[11] R. Cahn, *Z. Phys.* **C15** 253 (1982). Note that the Coulomb phase $\alpha\phi$ in Cahn's article is written here as δ.

[12] Design Report Tevatron 1 Project, Fermi National Accelerator Laboratory, Batavia, IL (1984).

[13] B. F. Bayanov et al., *Nucl. Instrum. Methods* **190** 9 (1981).

[14] John Marriner, Fermilab-Conf-93/308, 1993.

[15] Michael Church, private communication 1994.

[16] T. A. Armstrong et al., *Phys. Rev.* **D47** 772 (1993).

[17] Particle Data Group, *Phys. Rev.* **D50** 1173 (1994).

[18] T. Bagwell et al., Fermilab Technical Memo 1254 (1984).

[19] C. Baglin et al., *Nucl. Phys.* **B286** 592 (1987), see Appendix B; also M. Macri in *Proceedings of the CERN Accelerator School, 1989 at Geneva, Switzerland* edited by P. Bryant and S. Newman (1983) CERN 84-15 p. 469.

[20] C. Biino et al., *Nucl. Instrum. Methods* **A317** 135 (1992).

[21] L. Bartoszek et al., *Nucl. Instrum. Methods* **A301** 47 (1991).

[22] C. Biino et al., *Nucl. Instrum. Methods* **A271** 417 (1988); *IEEE Trans. Nucl. Sci.* **36** 98 (1989).

[23] R. Calabrese et al., *Nucl. Instrum. Methods* **A277** 116 (1989).

[24] G. Barisone et al., *Report No. Genova INFN/AE-89* (1989).

[25] S. Trokenheim et al., *Nucl. Instrum. Methods* **A355** 308 (1995).

[26] Intertechnique, Instrumentation Nucleaire Enertec, 1, Chemin de la Roseraie, 67383 Lingolsheim, Cedex, France.

[27] BEI Electronics, Inc., 819 Reddick Ave., Santa Barbara, CA 93103.

[28] MDC Vacuum Products Corporation, 23842 Cabot Boulevard, Hayward, CA 94545-1651, USA.

[29] C.F.G. Delaney and E.C. Finch, *Radiation Detectors: Physical Principles and Applications* (Clarendon Press, Oxford, 1992).

[30] Oak Ridge Technical Enterprises Corporation, P.O. Box C, Oak Ridge, TN, USA.

[31] Tennelec Inc., 601 Oak Ridge Turnpike, P.O. Box 2560, Oak Ridge, TN 37831-2560, USA.

[32] Nuclear Data Inc., Instrumentation Division, Golf and Meachem Roads, Schaumburg, IL 60196, USA.

[33] W. Grein and P. Kroll, *Nucl. Phys.* **B137** 173 (1978).

[34] W. Grein and P. Kroll, *Nucl. Phys.* **A338** 332 (1980).

[35] M. L. Goldberger et al., *Phys. Rev.* **120** 2250 (1960).

[36] O. Dumbrajs et al., *Nucl. Phys.* **B216** 277 (1983).

[37] R. A. Arndt et al., *Phys. Rev.* **C50** 2731 (1994).

[38] T. A. Rijken et al., *Nucl. Phys.* **A508** 173c (1990).

[39] R. Timmermans et al., THEF-NYM-93-02 (1994), *submitted to Phys. Rev. C.*

[40] V. G. J. Stoks et al., *Phys. Rev.* **C49** 2950 (1994).

[41] C. A. Baker et al., *Nucl. Phys.* **A483** 631 (1988).

[42] G. Hohler et al., *Nucl. Phys.* **B114** 505 (1976).

[43] Martin L. Perl, *High Energy Hadron Physics*, (John Wiley and Sons, New York, 1974).

[44] U. Amaldi et al., *Phys. Lett.* **B43** 231 (1973).

[45] U. Amaldi et al., *Phys. Lett.* **B66** 390 (1977).

[46] V. Bartenev et al., *Phys. Rev. Lett.* **31** 1088 (1973).

[47] G. G. Beznogikh et al., Phys. Lett. **B39** 411 (1972).

[48] J. D. Dowel et al., *Phys. Lett.* **12** 252 (1964).

[49] K. J. Foley et al., *Phys. Rev. Lett.* **14** 74 (1965).

[50] D. Gross et al., *Phys. Rev. Lett.* **41** 217 (1978).

[51] L. F. Kirillova et al., *Phys. Lett.* **13** 93 (1964).

[52] E. Lohrman et al., *Phys. Lett.* **13** 78 (1964).

[53] A. A. Vorobyov et al., *Phys. Lett.* **B41** 639 (1972).

[54] G. Bellettini et al., *Phys. Lett.* **14** 164 (1965).

[55] A. E. Taylor et al., *Phys. Lett.* **14** 54 (1965).

[56] K. J. Foley et al., *Phys. Rev. Lett.* **19** 857 (1967).

[57] P. Jenni et al., *Nucl. Phys.* **B94** 1 (1975).

[58] P. Jenni et al., *Nucl. Phys.* **B129** 232 (1977).

[59] L. A. Fajardo et al., *Phys. Rev.* **D24** 46 (1981).

[60] R. E. Breedon et al., *Phys. Lett.* **B216** 459 (1989).

[61] N. Amos et al., *Phys. Lett.* **B128** 343 (1983).

[62] N. Amos et al., *Phys. Lett.* **B120** 460 (1983).

[63] H. Iwasaki et al., *Phys. Lett.* **B103** 247 (1981).

[64] H. Kaseno et al., *Phys Lett* **B68** 487 (1977) (errata).

[65] L. Linssen et al., *Nucl. Phys.* **A469** 726 (1987).

[66] W. Bruckner et al., *Phys. Lett.* **B158** 180 (1985).

[67] V. Ashford et al., *Phys. Rev. Lett.* **54** 518 (1985).

[68] M. Cresti et al., *Phys. Lett.* **B132** 209 (1983).

[69] P. Schiavon et al., *Nucl. Phys.* **A505** 595 (1989).

[70] C. Augier et al., *Phys. Lett.* **B316** 448 (1993).

[71] N. A. Amos et al., *Phys. Rev. Lett.* **68** 2433 (1992).

[72] R. J. Abrams et al., *Phys. Rev.* **D1** 1917 (1970).

[73] J. V. Allaby et al., *Phys. Lett.* **B30** 500 (1969).

[74] W. W. M. Allison et al., *Nucl. Phys.* **B56** 1 (1973).

[75] U. Amaldi et al., *Nuovo Cimento* **34** 825 (1964).

[76] U. Amaldi et al., *Nuovo Cimento* **A46** 171 (1966).

[77] S. F. Biagi et al., *Nucl. Phys.* B186 1 (1981).

[78] M. Bozzo et al., *Phys. Lett.* **B147** 392 (1984).

[79] D. V. Bugg et al., *Phys. Lett.* **B194** 563 (1987).

[80] A. S. Carroll et al., *Phys. Rev. Lett.* **33** 928 (1974).

[81] F. Abe et al., *Phys. Rev.* **D50** 5550 (1994).

[82] V. Chaloupka et al., *Phys. Lett.* **B61** 487 (1976).

[83] B. Conforto et al., *Nuovo Cimento* **A54** 441 (1968).

[84] C. A. Coombes et al., *Phys. Rev.* **112** 1303 (1958).

[85] B. Cork et al., *Phys. Rev.* **107** 248 (1957).

[86] B. Cork et al., *Nuovo Cimento* **25** 497 (1962).

[87] O. Czyzewski et al., *Phys. Lett.* **15** 188 (1965).

[88] H. C. Dehne et al., *Phys. Rev.* **B136** 843 (1964).

[89] S. P. Denisov et al., Nucl. Phys. **B65** 1 (1973).

[90] B. Escoubes et al., *Phys. Lett.* **5** 132 (1963).

[91] T. Ferbel et al., *Phys. Rev.* **B137** 1250 (1965).

[92] T. Ferbel et al., *Phys. Rev.* **173** 1307 (1968).

[93] P. S. Gregory et al., *Nucl. Phys.* **B119** 60 (1977).

[94] R. W. Green et al., *Phys. Rev.* **D9** 90 (1974).

[95] G. R. Kalbfleisch et al., *Nucl. Phys.* **B30** 466 (1971).

[96] T. Kamae et al., *Phys. Rev. Lett.* **44** 1439 (1980).

[97] G. D. Patel et al., *Z. Phys.* **C12** 189 (1982).

[98] N. A. Amos et al., *Nuovo Cimento* **A106** 123 (1993).

[99] K. Bockmann et al., *Nuovo Cimento* **A42** 954 (1966).

[100] T. Kitagaki et al., *Phys. Rev. Lett.* **21** 175 (1968).

[101] D. S. Ayres et al., *Phys. Rev.* **D15** 3105 (1977).

[102] W. Galbraith et al., *Phys. Rev.* **B138** 913 (1965).

[103] S. J. Lindenbaum et al.,*Phys. Rev. Lett.* **7** 185 (1961).

[104] S. P. Denisov et al., *Phys. Lett.* **B34** 167 (1971); *Phys. Lett.* **B36** 528 (1971); *Phys. Lett.* **B36** 415 (1971).

[105] G. von Dardel et al., *Phys. Rev. Lett.* **5** 333 (1960).

[106] A. S. Carroll et al., *Phys. Lett.* **B61** 303 (1976).

[107] A. S. Carroll et al., *Phys. Lett.* **B80** 423 (1979).

[108] G. Carboni et al., Nucl. Phys. **B254** 697 (1985).

[109] G. Alexander et al., *Phys. Rev.* **154** 1284 (1967).

[110] S. P. Almeida et al., *Phys. Rev.* **174** 1638 (1968).

[111] U. Amaldi et al., *Nucl. Phys.* **B166** 301 (1980).

[112] V. V. Ammosov et al., *Phys. Lett.* **B42** 519 (1972).

[113] A. Ashmore et al., *Phys. Rev. Lett.* **5** 576 (1960).

[114] L. Baksay et al., *Nucl. Phys.* **B141** 1 (1978).

[115] Barashenkov et al., *Fortschr. Phys.* **9** 549 (1961).

[116] S. Barish et al., *Phys. Rev.* **D9** 2689 (1974).

[117] V. Bartenev et al., *Phys. Rev. Lett* **29** 1755 (1972).

[118] G. Bellettini et al., *Phys. Lett.* **19** 705 (1966).

[119] V. Blobel et al., *Nucl. Phys.* **B69** 454 (1974).

[120] P. Breitenlohner et al., *Phys. Lett.* **7** 73 (1963).

[121] C. Bromberg et al., *Phys. Rev. Lett.* **31** 1563 (1973).

[122] D. V. Bugg et al., *Phys. Rev.* **146** 980 (1966).

[123] H. G. de Carvalho et al., Phys. Rev. **96** 398 (1954).

[124] F. Chen et al., *Phys. Rev.* **103** 211 (1956).

[125] S. Coletti et al., *Nuovo Cimento* **A49** 479 (1967).

[126] F. T. Dao et al., *Phys. Rev. Lett.* **29** 1627 (1972).

[127] A. N. Diddens et al., *Phys. Rev. Lett.* **9** 32 (1962).

[128] V. P. Dzhelepov et al., *Sov. Phys. Dokl.* **104** 380 (1955).

[129] K. Eggert et al., *Nucl. Phys.* **B98** 93 (1975).

[130] T. Elioff et al., *Phys. Rev. Lett.* **3** 285 (1959).

[131] D. Favart et al., *Phys. Rev. Lett.* **47** 1191 (1981).

[132] A. Firestone et al., *Phys. Rev.* **D10** 2080 (1974).

[133] J. Ginestet et al., *Nucl. Phys.* **B13** 283 (1969).

[134] V. M. Guzhavin et al., *Sov. Phys. JETP* **19** 847 (1964).

[135] E. L. Hart et al., *Phys. Rev.* **126** 747 (1962).

[136] G. J. Igo et al., *Nucl. Phys.* **B3** 181 (1967).

[137] M. A. Jabiol et al., *Nucl. Phys.* **B127** 365 (1977).

[138] M. E. Law et al., *Nucl. Phys.* **9** 600 (1959).

[139] M. J. Longo et al., *Phys. Rev. Lett.* **3** 568 (1959).

[140] M. J. Longo et al., *Phys. Rev.* **125** 701 (1962).

[141] J. Marshall et al., *Phys. Rev.* **91** 767 (1953).

[142] Marshall et al., *Phys. Rev.* **103** 222 (1956).

[143] M. G. Mescerjakov et al., *Nuovo Cimento Supl.* **3** 119 (1956).

[144] T. W. Morris et al., *Phys. Rev.* **103** 1472 (1956).

[145] K. F. Riley et al., *Phys. Rev.* **D1** 2481 (1970).

[146] P. Schwaller et al., *Phys. Lett.* **B35** 243 (1971).

[147] V. M. Sidorov et al., *Sov. Phys. JETP* **4** 22 (1957).

[148] L. W. Smith et al., *Phys. Rev.* **97** 1186 (1955).

[149] R. B. Sutton et al., *Phys. Rev.* **97** 783 (1955).

[150] I. Ambats et al., *Phys. Rev.* **D9** 1179 (1974).

[151] Y. M. Antipov et al., *Nucl. Phys.* **B57** 333 (1973).

[152] D. Birnbaum et al., *Phys. Rev. Lett.* **23** 663 (1969).

[153] H. Braun et al. *Nucl. Phys.* **B95** 481 (1975).

[154] V. Domingo et al., *Phys. Lett.* **B24** 642 (1967).

[155] T. Ferbel et al., *Phys. Rev.* **138** 1528 (1965).

[156] K. J. Foley et al., *Phys. Rev. Lett.* **11** 503 (1963).

[157] K. J. Foley et al., *Phys. Rev. Lett.* **15** 45 (1965).

[158] H. Kaseno et al., *Phys. Lett.* **B61** 203 (1976).

[159] U. Amaldi et al., *Phys. Lett.* **B36** 504 (1971).

[160] K. Chernev et al., *Phys. Lett.* **B36** 266 (1971).

[161] M. Holder et al., *Phys. Lett.* **B36** 400 (1971).

[162] G. Barbiellini et al., *Phys. Lett.* **B39** 663 (1972).